A THERMODYNAMIC MODELLING APPROACH TO PREDICT THE OUTCOME OF CARBONACEOUS FLUID METASOMATISM ON EARTH AND MARS

Michele Rinaldi

A Thesis Submitted for the Degree of PhD
at the
University of St Andrews

2023

A THERMODYNAMIC MODELLING APPROACH TO PREDICT THE OUTCOME OF CARBONACEOUS FLUID METASOMATISM ON EARTH AND MARS

Michele Rinaldi

University of
St Andrews

This thesis is submitted in partial fulfilment for the degree of

Doctor of Philosophy (PhD)

at the University of St Andrews

April 2023

ABSTRACT

The carbon flux between the atmosphere and the geosphere is linked by a broad range of geodynamic and magmatic processes which govern the deep carbon cycles on all telluric planets, asteroids, and moons. On Earth, carbon is introduced into the mantle by subduction. On Mars, deep carbon is mobilised by magmatism and mantle convection, with delamination the only likely mechanism to recycle crustal carbon. The mobilisation and transportation of phases across P-T-X gradients result in the destabilisation of carbon-bearing and hydrated minerals leading to the formation of melts and fluids. Both act as mass-transfer agents, mobilising and transferring carbon. The interaction of fluids and magmas with surrounding rocks results in metasomatism. The role of carbon-rich fluids in the formation of metasomatic minerals and methane reservoirs on Earth and Mars has been studied via thermodynamic modelling. Here I present the results of predictive simulations to express the evolution of metasomatic systems at different P-T-fO_2 conditions.

This study finds that the traditional distinction of diamonds through paragenetic groups cannot be used as a genetic classification because fluid-rock metasomatism can produce the compositional range of garnet and clinopyroxene found as inclusions in diamonds. The amount of carbon in the system – and its speciation – controls the geochemistry of metasomatic silicates, highlighting how carbon is even more influential than previously thought. Furthermore, fluid metasomatism can convert depleted mantle rocks into fertile websterites without championing a mechanism involving partial melting. Fluids have all the rock-forming elements to precipitate anhydrous silicates, and the presence or absence of hydrated minerals is no reliable evidence to distinguish melt and fluid metasomatism. Finally, the reduced conditions of Mars favour the formation of methane, which can be stored in geological reservoirs and then transported to the surface, sustaining the CH_4-based greenhouse required for liquid water on the surface of Early Mars.

AIM OF THIS WORK

The initial plan for this PhD was to study the likelihood of a magmatic origin for methane on Early Mars through experiments supplemented by thermodynamic modelling. However, because of restrictions on working conditions as a consequence of the COVID-19 pandemic, the required training for the essential laboratory work at St Andrews (experimental petrology, Raman spectroscopy, electron probe microanalysis, gas sourced isotope mass spectrometry) and the Carnegie Institution of Washington (experimental petrology, Raman spectroscopy, electron probe microanalysis) could not be guaranteed with any certainty owing to the unprecedented nature of the COVID-19 pandemic. Therefore, a new plan was devised to examine the origin of methanogenesis on Early Mars. The approach was re-focused on adopting a theoretical approach using the extended Deep Earth Water (DEW) model thermodynamic software.

Proper use of every thermodynamic software requires an established procedure to reproduce natural data in a computational process. My initial training with the DEW model exposed several important lines of enquiry which would strengthen the use of the DEW model when applying it to Mars. Moreover, the relative dearth of data Mars concerning the geochemistry and petrology of the Martian interior led to the decision to refine the model using the relatively large dataset of diamond inclusion geochemistry and mineralogy because diamond-formation is fundamentally the result of carbon-rich metasomatism, albeit on Earth.

This new approach proved to be fruitful in the fact that I have accurately reproduced natural data and answered the following questions:

- Can fluid-rock interaction reproduce the range of garnet and clinopyroxene compositions found as diamond inclusions? If so, are these inclusions compositions (traditionally used for the diamond classification) genetically related phases as opposed to distinct mantle provinces?

- Does the carbon content of metasomatic fluids directly influence the composition of metasomatic silicate minerals? If so, what's its impact on the geochemistry of mantle diamond inclusions?
- What is the result of fluid metasomatism? In particular, are hydrous minerals a reliable signature for fluid-rock interaction?
- What is the likelihood of a magmatic origin for methane on Early Mars, and could such a process sustain a CH_4-based greenhouse on Early Mars?

This work resulted in a series of manuscripts presented here as Data Chapters:

- Chapter 3 is the manuscript submitted to *Geochimica et Cosmochimica Acta* about the origin of diamond inclusions, and it is currently in the second round of review. This is the direct evolution of Mikhail et al. (2021) (*Geochemical Perspective Letters*), in which I am the second author.
- Chapter 4 is a draft of a forthcoming paper about the metasomatic origin of pyroxenites.
- Chapter 5 is the manuscript submitted to *Nature Geoscience* about methanogenesis on Early Mars, and it is currently in revision.

Each Data Chapter can be read as a stand-alone study, and the overarching essential background information is presented in Chapter 1: Introduction and Chapter 2: Method. Chapter 6: Conclusions and Further work summarises the significant results and describes new ideas for my future career

Research Data

Research data underpinning this thesis are available at https://doi.org/10.17630/72f28ceb-4290-4de1-8778-56ed6a2e837c.

Candidate's declaration

I, Michele Rinaldi, do hereby certify that this thesis, submitted for the degree of PhD, which is approximately 24,000 words in length, has been written by me, and that it is the record of work carried out by me, or principally by myself in collaboration with others as acknowledged, and that it has not been submitted in any previous application for any degree. I confirm that any appendices included in my thesis contain only material permitted by the 'Assessment of Postgraduate Research Students' policy.

I was admitted as a research student at the University of St Andrews in September 2019.

I received funding from an organisation or institution and have acknowledged the funder(s) in the full text of my thesis.

Date 21/08/2023 Signature of candidate

Supervisor's declaration

I hereby certify that the candidate has fulfilled the conditions of the Resolution and Regulations appropriate for the degree of PhD in the University of St Andrews and that the candidate is qualified to submit this thesis in application for that degree. I confirm that any appendices included in the thesis contain only material permitted by the 'Assessment of Postgraduate Research Students' policy.

Date 21/08/2023 Signature of supervisor

Permission for publication

In submitting this thesis to the University of St Andrews we understand that we are giving permission for it to be made available for use in accordance with the regulations of the University Library for the time being in force, subject to any copyright vested in the work not being affected thereby. We also understand, unless exempt by an award of an embargo as requested below, that the title and the abstract will be published, and that a copy of the work may be made and supplied to any bona fide library or research worker, that this thesis will be electronically accessible for personal or research use and that the library has the right to migrate this thesis into new electronic forms as required to ensure continued access to the thesis.

I, Michele Rinaldi, have obtained, or am in the process of obtaining, third-party copyright permissions that are required or have requested the appropriate embargo below.

The following is an agreed request by candidate and supervisor regarding the publication of this thesis:

Printed copy

No embargo on print copy.

Electronic copy

Embargo on all of electronic copy for a period of 1 year on the following ground(s):

- Publication would preclude future publication

Supporting statement for electronic embargo request

The data in this thesis are under consideration for being published in scientific journals.

Title and Abstract

- I agree to the title and abstract being published.

Date 21/08/2023 Signature of candidate

Date 21/08/2023 Signature of supervisor

Underpinning Research Data or Digital Outputs

Candidate's declaration

I, Michele Rinaldi, understand that by declaring that I have original research data or digital outputs, I should make every effort in meeting the University's and research funders' requirements on the deposit and sharing of research data or research digital outputs.

Date 21/08/2023 Signature of candidate

Permission for publication of underpinning research data or digital outputs

We understand that for any original research data or digital outputs which are deposited, we are giving permission for them to be made available for use in accordance with the requirements of the University and research funders, for the time being in force.

We also understand that the title and the description will be published, and that the underpinning research data or digital outputs will be electronically accessible for use in accordance with the license specified at the point of deposit, unless exempt by award of an embargo as requested below.

The following is an agreed request by candidate and supervisor regarding the publication of underpinning research data or digital outputs:

Embargo on all of electronic files for a period of 1 year on the following ground(s):

- Publication would preclude future publication

Supporting statement for embargo request

The data in this thesis are under consideration for being published in scientific journals.

Date 21/08/2023 Signature of candidate

Date 21/08/2023 Signature of supervisor

DISCLAIMER

The studies in this thesis are the result of collaborative work. Therefore, here I detail the contributions of other co-authors to the data presented in the following chapters.

Chapter 3

Sami Mikhail (University of St Andrews, UK) provided the idea for the study and insights about diamond inclusions formation. Dimitri A. Sverjensky (Johns Hopkins University, USA*)* provided the model of the eclogitic fluid based on Kessel et al. (2015), and insights and technical support about the Deep Earth Water model. Joanna Kalita (University of St Andrews, UK) provided help with running thermodynamic models.

Chapter 4

Sami Mikhail (University of St Andrews, UK) provided help in the definition of the metasomatic environments considered. Dimitri A. Sverjensky (Johns Hopkins University, USA*)* provided technical support for the Deep Earth Water model.

Chapter 5

Sami Mikhail (University of St Andrews, UK) provided the idea for the study and insights about the thermal profile of Early Mars. Dimitri A. Sverjensky (Johns Hopkins University, USA*)* provided insights about the metastability of methane and technical support for the Deep Earth Water model.

Chapter 6

Simone Tumiati (University of Milan, Italy) and Luca Toffolo (University of Milan, Italy) provided help in devising the experimental setup for corroborating thermodynamic models.

ACKNOWLEDGEMENTS

There are many people I am grateful to for helping me produce this thesis. I want to start with my supervisor, Dr Sami Mikhail, the best supervisor I could have ever asked for. He supported me in all my choices and provided invaluable help during my PhD on personal and scientific matters. Despite my strong tendency to fall into rabbit holes (and being a giant nerd), he kept me on track every time without freaking out (I still don't know how he managed to do it). Without any doubt, I am the researcher I am now, thanks to him.

I am grateful to Prof Dimitri Sverjensky, who taught me everything he knows about the Deep Earth Water model and endured my rookie questions even after 3.5 years of pure modelling. My entire PhD was only possible with your supervision and patience. If my love for thermodynamic modelling was great, now it is even more.

I want to thank the research group (Dr Filippo Formoso, Dr Toby Boocock, and Dr Eleanor Mare) for helping me become more confident, providing great comments and support, and having a great time during the meetings, social events, and conferences. Despite working on different topics, you always had interesting questions and suggestions, which made my work better (and my life easier).

Prof Stefano Poli, who always looked after me even after the end of my Master's degree. I am at this point in my career because of you. Thanks for sharing your passion for petrology, modelling and experiments with me all these years.

To Simone Tumiati, Luca Toffolo, and Andrea Risplendente, who welcomed me back to the University of Milan in the last months of my PhD. The experimental work was only possible with you.

A giant thank you goes to Peize Li, my girlfriend, one of the best people I have ever met. Besides being a great drinking and party mate, your kindness made my life (and my character) so much better. The last year would not have been the same without you.

To Fiona Fotherby, my best friend in St Andrews, with whom I shared many good memories and so much food and drinks. She was always at hand when I needed anything and always provided great suggestions.

To all my colleague/friends in St Andrews who made the experience abroad much better than I thought it could be. I will miss the Friday beers and hanging out with you, but I am sure we will meet again somewhere sooner or later. In particular, the first people I met in St Andrews, Wilmer Koster and Hanna Ewen, for all the good nights we spent together.

A huge thank you goes to my best friends: Nicole Pezzotta and Roberta Invernizzi. With you, I made better choices all these years. Despite the years abroad, you were always with me.

To my former band, Insubria, who still considers me part of the group after all these years. One day I will play again with you, even if my lack of rhythm worsens (and it wasn't good since the beginning, let's be honest). And to all my Italian friends, who welcomed me back whenever I came home.

I am grateful to Richard White and Andrew Thomson for the excellent viva and review they provided.

Infine, a Mamma e Papà, che in tutti questi anni mi hanno sempre supportato e approvato le mie scelte di vita. Spero di rendervi fieri ad ogni mio passo nella carriera che mi sono scelto e, soprattutto, come persona.

FUNDING

This work was supported by the UK space agency Aurora grant (ST/T001763/1).

TABLE OF CONTENTS

CHAPTER 1

AN INTRODUCTION TO THE DEEP CARBON CYCLE AND AQUEOUS GEOCHEMICAL MODELLING

1.1 THE DEEP CARBON CYCLE

Carbon is a unique and irreplaceable element in our dynamic and evolving planet. The atmosphere's carbon content is critical to maintaining a habitable climate on Earth, and the carbon geochemistry of the oceans is vital for essential biogeochemical cycles supporting the food chain at every level. As we are experiencing for ourselves, altering the delicate equilibrium of the carbon cycle has drastic consequences on life and the environment. Our planet provides a complex mechanism to sustain such balance over geological eras (**Fig. 1.1**). About 1.85 billion gigatons of carbon are thought to be on Earth (Lee et al., 2019), and more than 90% reside inside the mantle and the core (Suarez et al., 2019). Volcanic CO_2 emissions control carbon fluxes between the mantle and the exosphere (Hoffman et al., 1998; Kerrick and Connolly, 2001; Storey et al., 2007) on a short to long geological scale (Hayes and Waldbauer, 2006; Huybers and Langmuir, 2009). The efficiency of such degassing is connected to both the depth and the extension of magmatic chambers beneath the volcanic zones. Deep magmas are carbon-richer than shallow ones, providing an extensive reservoir for long-term volatile emissions (Dasgupta et al., 2006; Dasgupta and Hirschmann, 2010). On the other hand, returning carbon to the deep Earth is crucial. Preventing its accumulation in the atmosphere avoids the consequent “carbon catastrophes”, which may have led to mass extinctions in the past (Suarez et al., 2019) or a runaway greenhouse effect (i.e., Venus). In billions of years, subduction can transport the entire carbon budget of the surface into the mantle and the core

(Sleep and Zahnle, 2001; Dasgupta and Hirschmann, 2010), bringing downward carbonate-rich sediments and altered oceanic crust (Arzilli et al., 2023).

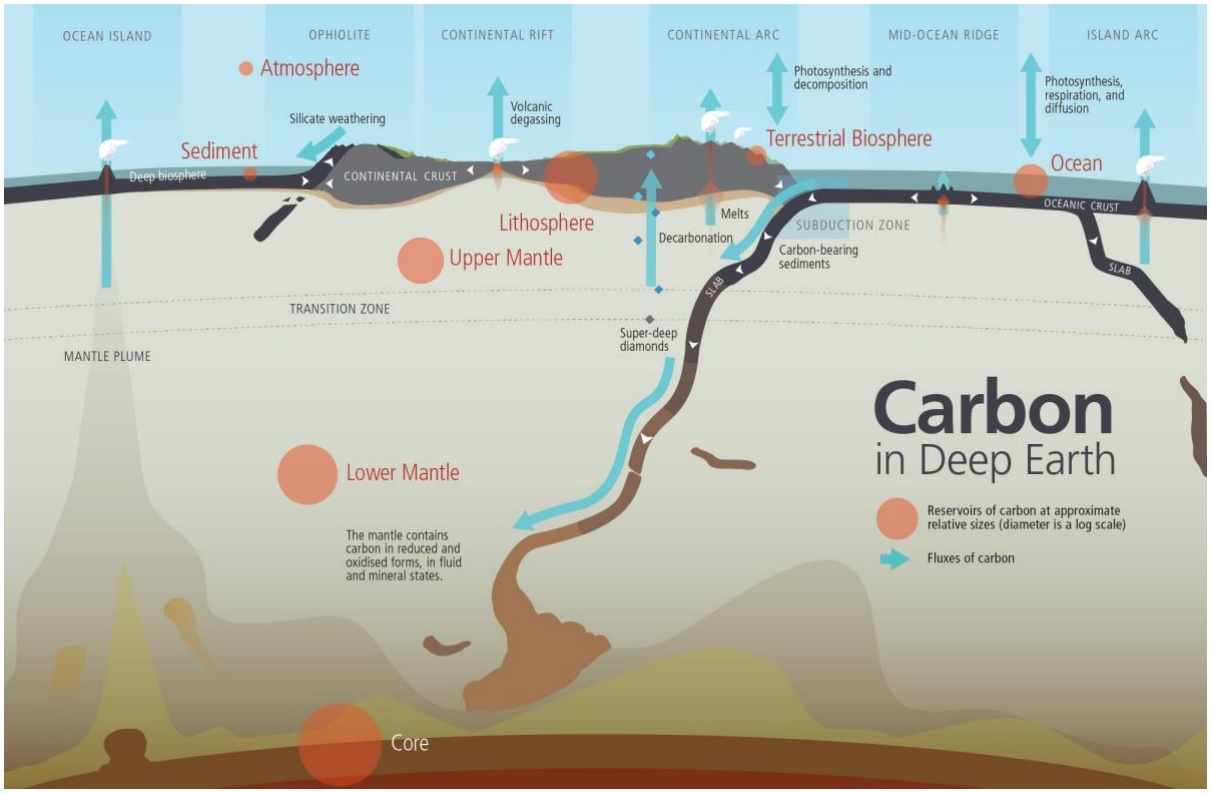

Figure 1.1 - Cartoon illustrating the deep carbon cycle and carbon reservoir in the Earth's interior. Figure from Deep Carbon Observatory (2019).

The degree of partial melting is determined by the geophysical asset of the subduction, defined by the pressure–temperature path of the slab, subduction angle, bulk composition of both oceanic crust and sediments, presence of water, and active magmatism. If the temperature at the top of the slab is high enough, carbon can be released in the mantle wedge due to partial melting (Poli, 2015) or decarbonisation (Molina and Poli, 2000; Gorman et al., 2006). Alternatively, cooler subduction allows carbon to remain stable in the residual crust, surviving shallow dehydration and hydrous melting processes, for being further transported in the deep mantle into refractory minerals (calcite, diamond, and graphite) (Connolly, 2005; Poli et al.,

2009; Thomson et al., 2016) and, potentially, reaching the core (Dasgupta and Hirschmann, 2010).

Once carbon has re-entered the Earth's mantle, the petrological characteristics of the environment control its fate. Carbon is stored in accessory minerals (Luth, 1999) and therefore has no direct influence over the physical properties of mantle lithologies. Oxygen fugacity, temperature, and pressure are critical parameters for redox-sensitive elements such as carbon (Tumiati and Malaspina, 2019). Carbon partially remains in graphite and diamond at reduced conditions, and further degassing is less efficient (Holloway, 1998). At oxidised conditions, carbon is in carbonates and can be easily extracted by partial melting (Dasgupta et al., 2006). The extremely low solubility of carbon in silicates (Keppler, 2003; Shcheka et al., 2006; Panero and Kabbes, 2008) implies that most of the carbon is stored in non-silicate phases. The stable crystalline phase at shallow (< 150 km) oxidised conditions is carbonate, with a progressive enrichment in magnesium as the depth increases (Dasgupta et al., 2006; Thomsen and Schmidt, 2008; Litasov and Ohtani, 2009). At depths > 150 km, the saturation of Fe-Ni-C alloys occurs (Rohrbach et al., 2007; Frost, 2008), and diamond, Fe-carbide and Fe-Ni metal are the most likely hosts for carbon (Frost and McCammon, 2008; Walter et al., 2008; Lord et al., 2009). Nevertheless, the thermodynamic stability in the lower mantle of carbonates cannot be ruled out, as magnesite and aragonite are known to be stable under such conditions (Santos et al., 2019). Finally, carbon is responsible for lowering the melting point of mantle lithologies, contributing to the ongoing mantle differentiation (Dasgupta et al., 2006, 2009) and catalysing the formation of oceanic lithosphere (Dasgupta et al., 2007). The melting of carbon-rich lithologies results in carbonatitic or carbonated silicate melts (Foley et al., 2009) and the subsequent release of water in a broad range of fluids (Sverjensky et al., 2014b; Mysen, 2022). Fluid's ability to mobilities geochemical components through mineral dissolution and

precipitation is the core of the deep carbon cycle, triggering a broad range of magmatic and metasomatic processes in both mantle and crust.

1.2 MANTLE METASOMATISM

Mantle metasomatism refers to general metamorphic processes where melts and fluids interact with the surroundings and alter the geochemical and petrological characteristics of the host rocks. Because of the chemical disequilibrium established, minerals which compose the rocks are dissolved and replaced by new minerals which directly reflect the composition of the liquid or fluid phase. During metasomatism, the rock remains in a solid state.

Two main types of metasomatism are prevalent: [1] diffusional metasomatism and [2] infiltration metasomatism. The first is related to the diffusion of a solute through a stagnant solution, and the driving force is the chemical potential gradient between the solution and the rock. The second takes place through the transfer of material in solution infiltrating the host rocks, and it is forced by pressure and concentration gradients (Zharikovf et al., 2006). Metasomatic events can be classified into three categories: [1] modal metasomatism (adding non-primary minerals), [2] cryptic metasomatism (changes in the mineral composition and trace elements, without introducing new minerals), and [3] stealth metasomatism (addition of secondary minerals which are indistinguishable from the primary minerals) (Gréau et al., 2011; O'Reilly and Griffin, 2013).

Both melts and fluids are responsible for metasomatic processes. If melts ultimately crystallise, fluids are only sampled as inclusions, and their behaviour is more enigmatic (Weiss et al., 2022). The passage of fluids is indeed recorded as a hidden variation in the geochemistry of solid phases but is often masked by the original geochemical signatures of the primary rock. Nevertheless, recent studies provide new insight into fluid-rock metasomatism, as fluids are

capable of precipitating silicate minerals as well as melts (Sverjensky et al., 2014b; Mikhail et al., 2021). The distinction between fluids and melts disappears at great depths and in supercritical regimes (Kessel et al., 2005a, b). Metasomatism is responsible for the modification and destruction of [1] the oceanic mantle (Weiss et al., 2016; Keller et al., 2017) and [2] the sub-continental lithospheric mantle (Tumiati et al., 2017; Tiraboschi et al., 2018), [3] the evolution of magmatic environments (Ammannati et al., 2016; Weiss et al., 2016), [4] re-fertilization of the depleted mantle (Laukert et al., 2014; Borghini et al., 2016), and [5] the formation of carbon-rich mineral such as diamond (Stachel and Harris, 2008; Sverjensky and Huang, 2015). The ratio between metasomatic rocks and primary rocks is unknown, but it is thought that very few primary rocks are left after billions of years of metasomatic events (O'Reilly and Griffin, 2013).

1.3 FLUIDS IN THE EARTH'S INTERIOR

The Cambridge dictionary defines a fluid as "a substance that flows and is not solid". Using this definition, silicate, carbonatite melts, and aqueous liquids are all described as fluids. In mantle petrology, the term is ubiquitous with a substance that is either liquid or supercritical in a state with a significantly hydrated geochemical composition (i.e., aqueous solutions). Fluids are involved in virtually all geological processes, from the surface to the lower mantle. The impact of fluids as mass transport agents inside Earth directly relates to pressure, temperature, redox conditions, and system bulk composition. Different geological environments have, therefore, a distinct influence on fluid formation and can suppress or promote the fluid-rock metasomatic interaction. Fluids can be generated during subduction (**Fig. 1.2**), where water-rich sediments and hydrothermal altered oceanic crust are brought down into the mantle (Evans and Tomkins, 2020). During the metamorphism, the fluids component is released and

incorporated into hydrous, carbonate and silicate minerals, and sometimes into F- and Cl-phases. Then, as the metamorphic grade increases, fluids are gradually released into the mantle wedge or even transported into the lower mantle (Ohtani, 2020). Once released, fluids can [1] trigger partial melting and being incorporated into magmatic liquids (Ulmer, 2001), [2] take part in metasomatic processes in the mantle wedge (Manning and Frezzotti, 2020), [3] migrate away from the subduction (Morishige and van Keken, 2018), or crystallise diamond. However, the origin(s) and nature of deep fluids are poorly constrained.

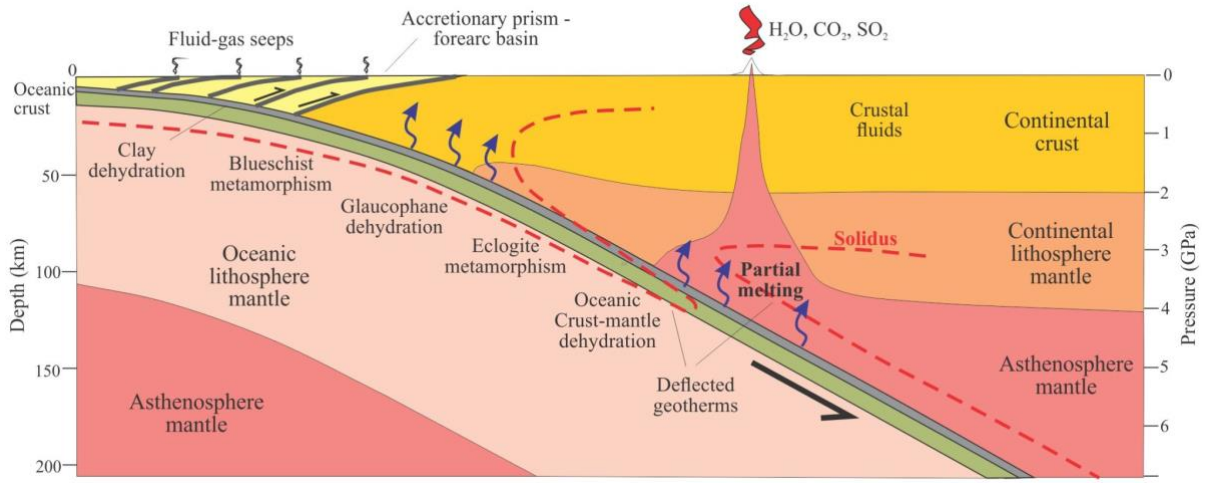

Figure 1.2 - Geodynamic evolution of a subduction zone. Fluids are released into the continental crust at shallow depths (< 50 km). At higher depths (> 50 km), fluids are released into the mantle wedge instead. The geochemistry of these fluids varies with pressure and temperature and is related to the dehydration of water- and carbon-rich minerals. Figure from Geological Digressions.

Fluids are a mix of neutral oxidised and reduced species and aqueous ions. Decades of experimental studies of mineral solubilities (Manning, 1994; Newton and Manning, 2010; Hunt et al., 2011), rock solubilities (Kessel et al., 2005a, b; Tsay et al., 2017; Elazar et al., 2019), and aqueous speciation at high pressures and temperatures (Mysen et al., 2013; Facq et al.,

2014; Schmidt and Manning, 2017) have established that fluids can contain up to >50 wt.% of rock-forming elements (Si, Fe, Mg, Ca, etc.). The solubility of an element in the fluid depends on the element of interest, the environmental conditions (pressure, temperature, and oxygen fugacity), the composition of the fluid, and the mineralogy of the source rock (Hunt and Manning, 2012; Scheuermann et al., 2018). Based on their composition, fluids vary from silicic (high SiO_2 content) to saline (high halogen content) and to carbonatitic (high divalent ions content) (Tomlinson et al., 2006; Shirey et al., 2013).

Redox conditions control fluid speciation, especially when redox-sensitive elements are involved. The two main fO_2-dependent carbon species are CO_2 and CH_4 (Taylor and Green, 1986; Zhang and Duan, 2009), alongside sulfur and nitrogen species in specific circumstances (Busigny et al., 2011). Water is predominant (Jambon, 1994), and CO_2 is the second-most abundant component (Tiraboschi et al., 2022). Carbon availability is traditionally linked to carbonate minerals (Manning, 2013) but can also be found in small concentrations inside solid solutions such as apatite and scapolite (Harlov, 2015). The CO_2/H_2O normally ratio increases with the depth of fluid release as carbonates are more stable at higher pressures and temperatures than OH-bearing minerals (Poli and Schmidt, 2003). Variations in the CO_2/H_2O ratio deeply influence the solubility of elements, the migration of the fluid and the bulk composition of partial melts in the metasomatised mantle wedge (Manning, 2004; Manning and Frezzotti, 2020). Chlorides and sulfides can also be important fluids components, and they are mostly related to oceanic water and sediments (Kawamoto et al., 2014; Morrissey and Tomkins, 2020).

The physical and chemical structure of a fluid is a function of its composition as well as the type and proportion of oxide solutes. Under most conditions, H_2O is the predominant component and controls the fluid structure and behaviour (Jambon, 1994). Other elements, such as F, Cl, and S, are relevant in the C-O-H-N-S system, but their influence depends on

pressure, temperature, and redox conditions (Bouhifd et al., 2006; Grove et al., 2012). Nevertheless, theoretical and experimental work predicts the existence of carbon-rich fluids, where water is a minor component (Zhang and Duan, 2009; Tiraboschi et al., 2022). Under the conditions of Earth's interior, individual H_2O molecules are linked together by hydrogen bonding (Sahle et al., 2013). As these bounds are weaker than silicate chains, fluids have lower density and viscosity than silicate melts. These characteristics improve the extent and efficiency of fluid migration. When favourable geophysical conditions, fluids can travel large distances along grain boundaries (Watson and Lupulescu, 1993) or fractures (White et al., 2019) without causing partial melting. Such behaviour is likely for fluids with low solubility in magmas and a limited influence over the solidus temperature of rocks (Mysen, 2022).

Fluids are a dynamic system that quickly re-equilibrate with the surrounding (Sverjensky et al., 2014a, b; Mikhail et al., 2021). This implies the formation of metasomatic minerals, and the fluid-rock interaction can profoundly change the petrological characteristic of the environment. Natural samples with fluid inclusions are rare, but sometimes fluids can be trapped inside accessory minerals such as diamonds or other xenocrysts (Frezzotti et al., 2011; Weiss et al., 2022), providing invaluable samples. The number of samples decreases with the depth, as only a few geological processes, such as kimberlites, can transport deep rocks and bring them to the surface quickly enough to avoid the loss of fluid inclusion-bearing minerals. On the other hand, experiments involving fluid-rock interaction are hard to develop, as H-bearing species tend to diffuse into the capsule under high pressure and temperature conditions (Kadik et al., 2013). Experimentally constraining relevant parameters such as oxygen fugacity and pH is only sometimes feasible or accurate, often losing a fundamental aspect for comprehending fluid-rock interaction. At the current state of the art, aqueous geochemical modelling is one of the most dynamic and controlled approaches to studying metasomatic processes, where the software easily controls environmental parameters.

1.4 AQUEOUS GEOCHEMICAL MODELLING OF METASOMATIC INTERACTIONS

Geochemical modelling of water-rock interaction has long been possible under crustal conditions. The fundamental theory of aqueous geochemistry was developed by Helgeson in the 1960s (Helgeson, 1964, 1969) and culminated in a four-series of papers in the next twenty years (Helgeson and Kirkham, 1974a, b, 1976; Helgeson et al., 1981). This pioneering work provided the Helgeson-Kirkham-Flowers (HFK) equations of state for aqueous species. Based on this foundation, subsequent works have refined such equations of state (Tanger and Helgeson, 1988; Shock and Helgeson, 1988, 1990; Shock et al., 1989, 1997) . The significant achievement of the revised HFK equations was the predictive estimation schemes for the equation of state parameters of aqueous species. The calculation of the standard partial molal properties at 25 °C and 1.0 bar for a broad range of aqueous species was incorporated in the code SUPCRT92 (Johnson et al., 1992) and allowed the geochemical calculation of fluid-rock interaction up to 0.5 GPa (**Fig. 1.3a**), which has been extensively used in geoscience and geotechnical applications.

The lack of knowledge of the dielectric constant of pure water at higher pressure defined the 0.5 GPa limit (**Fig. 1.3a**). The dielectric constant of water appears in the Born equation for solvation. It is a critical component in modelling the standard partial molal properties and the non-standard contributions of aqueous species at high pressure and temperature (Helgeson et al., 1981). The recent characterisation of the dielectric constant of water through a semi-empirical equation for polar solvents (Franck et al., 1990) and *ab-initio* molecular dynamics (Pan et al., 2013) led to the development of the Deep Earth Water (DEW) model (Sverjensky et al., 2014a; Huang and Sverjensky, 2019) and increased the pressure upper limit where aqueous modelling is applicable (**Fig. 1.3b**).

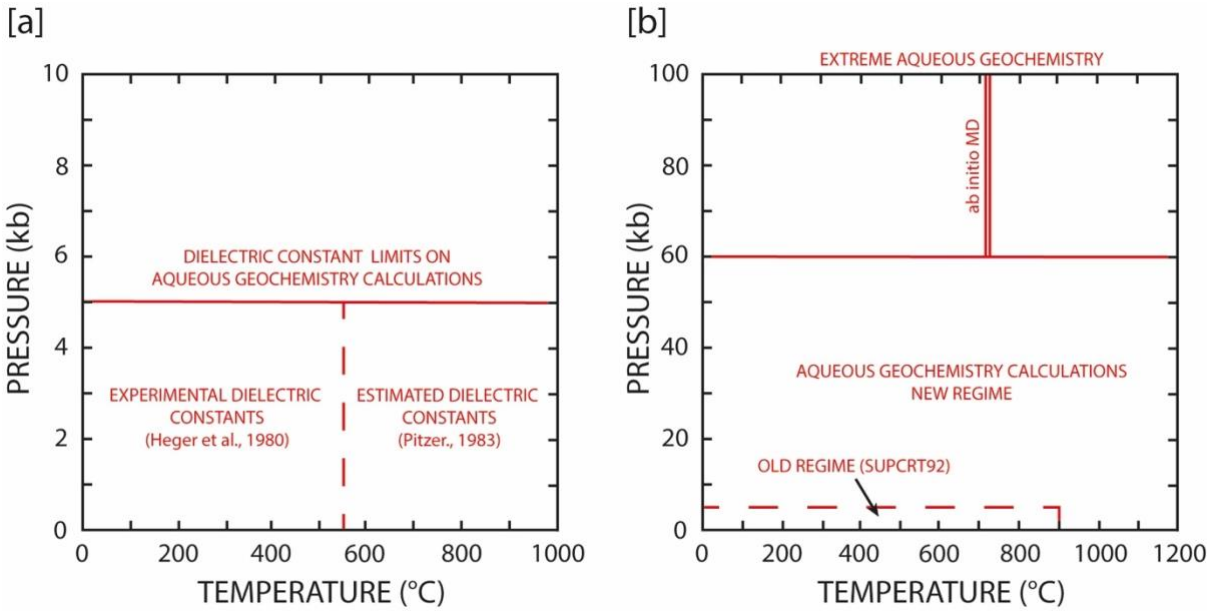

Figure 1.3 - Limits of the quantitative geochemical modelling: a) range of the dielectric constant in SUPCRT92 (Heger et al., 1980; Pizter, 1983; Johnson et al., 1992) and b) range of the dielectric constant in the DEW model (Pan et al., 2013; Sverjensky et al., 2014). Figure reproduced from Sverjensky (2019).

The DEW model is calibrated through experimental data of ion speciation at high pressures (Facq et al., 2014, 2016), solubility speciation of neutral species (Newton and Manning, 2002; Tropper and Manning, 2007; Mysen, 2010), experimental solubilities of synthetic rocks in the Na_2O-K_2O-MgO-CaO-Al_2O_3-SiO_2-FeO-H_2O-CO_2-H_2 system(Dvir et al., 2011; Kessel et al., 2015), and previous C-O-H fluid models (Duan and Zhang, 2006). After the recent incorporation of preliminary models for C-rich aqueous species (Huang and Sverjensky, 2019), the solubility and mass transfer codes are no longer restricted to water-rich fluids. As a result, a predictive model of C-rich metasomatism is also possible (Huang and Sverjensky, 2020; Mikhail et al., 2021). The DEW model allows the prediction of the equilibrium constants for hydrolysis reactions, aqueous complexing reactions, and other reactions involving hydration and organic species. These predicted equilibrium constants from the DEW model are

incorporated in the database of aqueous speciation and solubility code EQ3 and in the irreversible mass transfer code EQ6 (Wolery, 1992), modified for upper mantle conditions. Therefore, the geochemical modelling of aqueous speciation, solubilities, and chemical mass transfer is now feasible up to 6.0 GPa and 1200 °C (**Fig. 1.3b**).

CHAPTER 2

THERMODYNAMIC MODELLING OF METASOMATIC SYSTEMS

2.1 THE DEEP EARTH WATER MODEL

The Deep Earth Water model (DEW) is a thermodynamic software which allows the theoretical geochemical calculation of fluid-rock interaction using the Helgeson – Kirkham – Flowers (HKF) equations of state (Helgeson and Kirkham, 1974a, b, 1976; Helgeson et al., 1981; Shock and Helgeson, 1988; Shock et al., 1997; Sverjensky et al., 1997) up to 6 GPa and 1200°C. The equilibrium constants for aqueous complexes are calculated through the DEW model, and the ones for minerals are obtained by fitting Berman's equations (Berman, 1988) to experimental data. The equilibrium constants for solid and dissolved components are incorporated in the aqueous speciation, solubility, and chemical mass transfer codes EQ3 and EQ6 (Wolery, 1983, 1984, 1992).

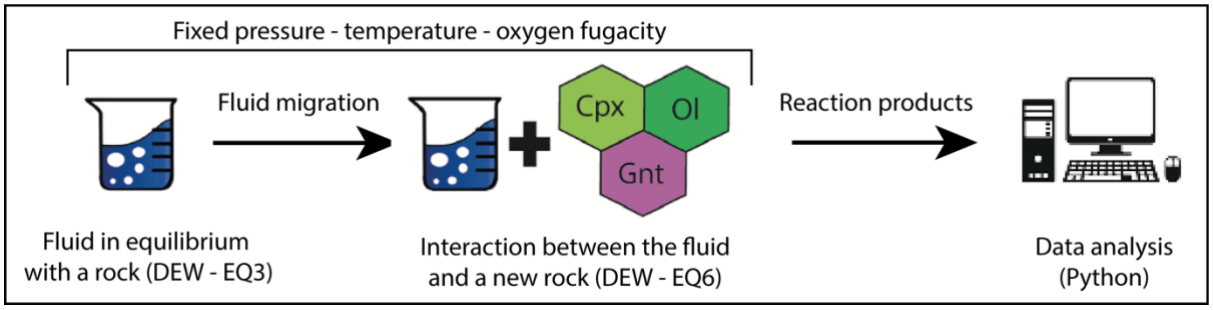

Figure 2.1 - Schematic modelling approach used in this work. The aqueous speciation and solubility code EQ3 and the mass transfer code EQ6 are the core of the modelling part. The results are then analysed through *ad-hoc* Python scripts.

In the first step, the composition and speciation of the fluid in equilibrium with the initial lithology are calculated with the aqueous speciation and solubility code EQ3. Then, the fluid

interacts with a different rock under isobaric and isothermal conditions in a closed system. Because the fluid-rock system is not in equilibrium, a chemical gradient drives irreversible mass transfer reactions, which are calculated using the mass transfer code EQ6 calibrated for upper mantle conditions (Sverjensky, 2019; Huang and Sverjensky, 2019) (**Fig. 2.1** and **Fig. 2.2**). The model is built to simulate the evolution of a single batch of fluid interacting with a host rock where the fluid directly controls the dissolution of the host rock and the precipitation of metasomatic minerals. Therefore, a step-by-step metasomatic interaction is modelled: the fluid progressively dissolves the reactant rock, and the fluid geochemistry changes accordingly, triggering the formation of metasomatic minerals. Each unit of the reaction progress (ξ) corresponds to the destruction of 1.0 mole of each of the reactant minerals per 1.0 Kg of H_2O in the initial fluid. The process continues until the reactant rock is equilibrated with the fluid or the changes in the fluid geochemistry are no longer relevant. For each step, the modelling results in the fluid speciation of aqueous anions, metal complexes, and neutral species, alongside the mineralogy and geochemistry of metasomatic minerals. The user does not force the formation of any phase in the system, and the software alone identifies the most stable aqueous and solid phases among the ones in the database (**Table A.1 – A.4**). Therefore, the metasomatic products are the most stable mineral assemblage in equilibrium with the fluid geochemistry of each step. As the process continues and a progressively higher amount of the reactant rock is destroyed, the fluid reciprocates the dissolution reactions modifying the fluid composition and the geochemistry of the metasomatic minerals precipitated. The variations of aqueous and solid phases among the steps define the system's evolution.

Each model outputs thousands of data in .txt files, and a manual analysis would have been time expensive. To work around this problem, *ad-hoc* Python scripts have been built to extract and plot these data.

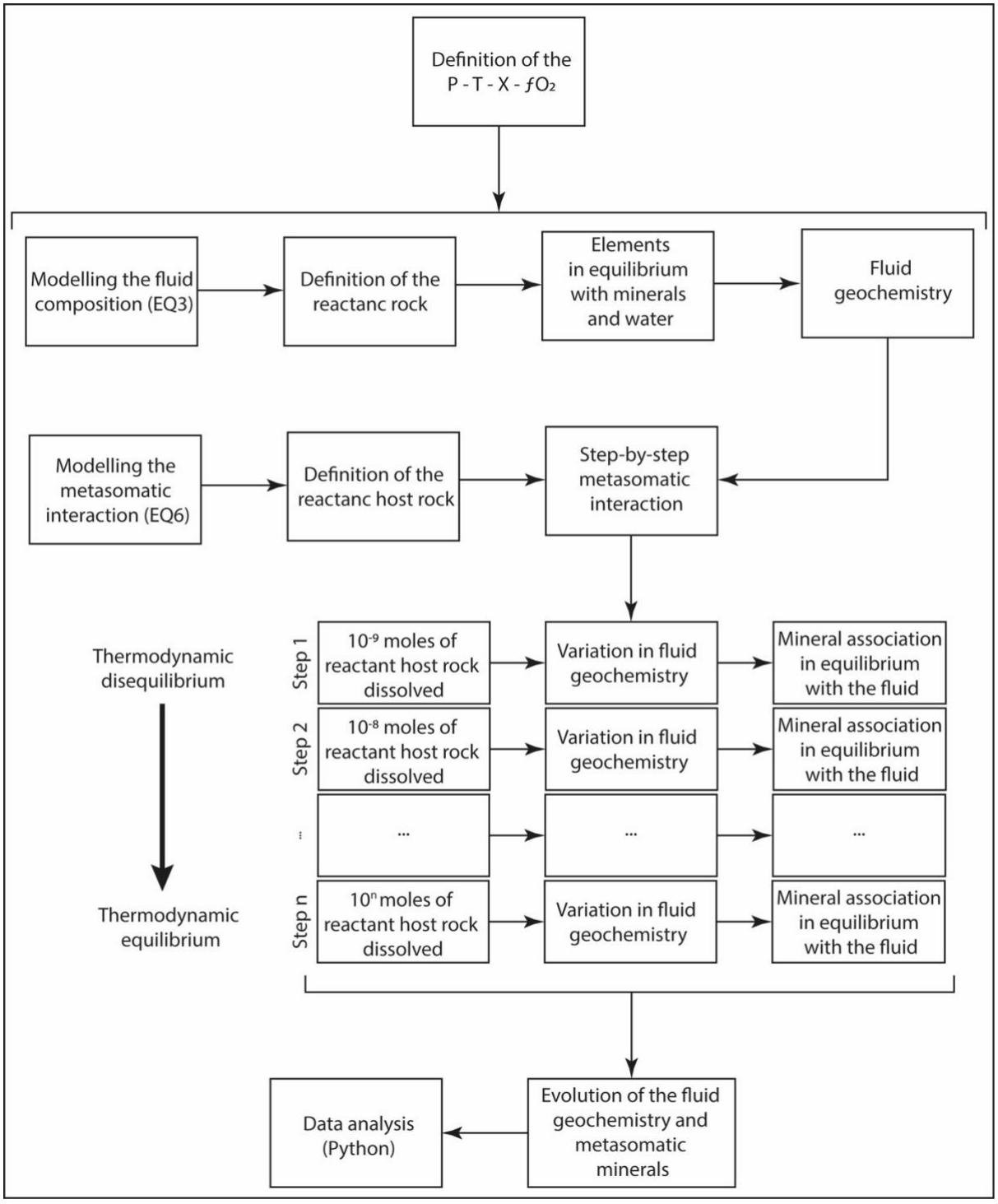

Figure 2.2 - Flowchart of the modelling approach and procedure used in this work. Firstly, the fluid is set in equilibrium with an initial rock (in EQ3). Then the fluid is 'placed' into another lithology where it is out of equilibrium and reacts (in EQ6). The reaction products are analysed with *ad-hoc* python scripts.

2.2 THEORY

The following paragraphs provide a description of how the Deep Earth Water model (DEW) works. The DEW works with the basic principle of thermodynamic modelling as any other software, but the mathematical and chemical approach to reaching the thermodynamic equilibrium differs from other common modelling software tools, such as PerpleX (Connolly, 2005) and Factsage (Bale et al., 2016). The complexity of the theoretical approach to thermodynamic modelling is far beyond the aim of this thesis, and a detailed analysis of the theory behind DEW can be found in Miron et al. (2019) and Sverjensky (2019).

2.2.1 The thermodynamic equilibrium

Software such as Perplex and Factsage use the Gibbs free energy minimisation (GEM) approach to predict phase equilibria as a function of P-T-X, where the $\Sigma\Delta G^0_{r\,P,T}$ for each phase in the system is minimised. The central assumption of GEM software is that the lower the energy of the system, the more stable the system is. Therefore, their databases are built with all the required thermodynamic parameters for an *ex-novo* calculation of $\Delta G^0_{r\,P,T}$ for each phase in every run. Phases are thus defined by thermodynamic parameters only, and no relationships between one phase and another are considered. The DEW model deviates from this approach considering every phase as intrinsically connected to a specific reaction, such as in the following example:

$$Eq.1 : Forsterite + 2\ H^+ \rightarrow\ Mg^{2+} + 0.5\ H_4SiO_4(aq)$$

Eq.1 shows the dissolution reaction which defines the relationship between a mineral (forsterite) and the fluid components (H^+, Mg^{2+}, and H_4SiO_4). The same concept is applied to all other phases. For aqueous species, the reaction represents the stability of a chemical species

in the fluid. Thermodynamics allows the calculation of the Gibbs Free energy for a reaction, shown in Eq.2:

$$Eq.2: \ \Delta G_{r\,P,T} = \ \Delta G^{0}_{r\,P,T} + 2.303RTlogQ$$

Where $\Delta G^{0}_{r\,P,T}$ is the apparent Gibbs free energy at a specific temperature (T) as a function of the Standard Gibbs Free energy ($\Delta G^{0}{}_{P,T}$), the gas constant (R = 8.314 J K^{-1} mol^{-1}), the thermodynamic activity quotient (Q), and 2.303 is a conversion factor from natural log to $\log_{10}$. Alike to other thermodynamic software, the DEW calculates thermodynamic equilibrium. This means that every single reaction, such as Eq.1, is treated as happening at equilibrium conditions, which implies $\Delta G^{0}{}_{P,T} = 0$. In this specific case, Eq.2 can be re-written as:

$$Eq.3: \ 0 = \ \Delta G^{0}_{r\,P,T} + 2.303RTlogK$$

and

$$Eq.4: K = \ \Pi_i (a_i)^{\nu_i}$$

Where K is the thermodynamic equilibrium constant, which defines a fixed activity ratio for the species in the reaction at given pressure and temperature. It should be noted that the ratio is fixed, but the value of each chemical activity (a_i) involved varies. When K > 1, there are more products than reactants; when K < 1, there are more reactants than products. Practically, this means that the product of the back reaction balances the product of the forward reaction, and there is no net change with time. The equilibrium constant K is sensitive to pressure and

temperature, and the system equilibrium varies as a function of the environmental conditions (pressure, temperature, fO_2, pH and bulk composition).

The DEW model database, therefore, contains the logK values for reactions which define each phase at fixed pressures and temperatures, and no thermodynamic parameters are present. The chemical activity is directly connected to the mole fraction of the related phase in the system, as the following equation, shown in Eq.5:

$$Eq.5 : a_{phase} = X_{phase} \cdot \lambda_{phase}$$

Where X is the mole fraction and λ is the rational activity coefficient. The definition of λ varies in function of the physical and chemical state of a phase (solid, gas, solvents, and aqueous solution), and an ideal behaviour (λ = 1) can be considered at ambient pressure and temperature with minimal errors. No ideal behaviour can be assumed for geological applications where temperature and pressures are far from the ambient conditions, and complex theoretical approaches must be considered to obtain a valid rational activity coefficient.

Much has been written about the relationship between activity coefficient and molal fraction (Zhang and Duan, 2009; Anderson, 2017), and no unique solution has been found that covers the range of geological P-T-X conditions. However, the critical point of thermodynamic modelling is considering a chemical-mathematical approach which best suits some simplifying assumptions required to compensate for the lack of experimental data. To date, the only framework built to be as general and predictive as possible is Helgeson et al., 1981, as other treatments have too many adjustable parameters (i.e., thermodynamic parameters required to describe the behaviour of an aqueous specie) to properly function in a predictive mode from a practical standpoint.

2.2.2 Evaluation of equilibrium constant over a wide range of pressure and temperatures

The evaluation of the equilibrium constant is a key feature in computing aqueous speciation, solubility, and mass transfer models. Traditionally, in aqueous geochemistry, the computer code SUPCRT92 has been used to calculate the K value of dissociation reactions, but it is limited to 1000 °C and 0.5 GPa. Instead, the DEW can calculate the equilibrium constants up to 1200 °C and 6.0 GPa, as the dielectric constant of water has been extended by Sverjensky et al. (2014a) up to these pressure-temperature conditions. The influence of the dielectric constant of water is briefly discussed later in this chapter. From Eq.3, the equilibrium constant can be defined as:

$$Eq.6: logK = \frac{\Delta G^0_{r\ P,T}}{-2.303RT}$$

The definition of $\Delta G^0_{r\ P,T}$ at high temperature and pressure is required for the calculation of logK. To do this, we need the standard Gibbs free energy for each phase involved in a reaction, shown in Eq.7:

$$Eq.7: \Delta G^0_{r\ P,T} = \Sigma_j\ v_j\ \Delta G^0_{f\ j\ P,T}$$

where:

$$Eq.8: \Delta G^0_{r\ P,T} = \Delta G^0_{f,j\ Pr,Tr} + (\Delta G^0_{j\ P,T} - \Delta G^0_{j\ Pr,Tr})$$

The first right-hand term in Eq.8 refers to the true standard Gibbs free energy of formation of j^{th} at reference conditions, while the second term is the variation of the Gibbs free energy of the j^{th} with temperature and pressure. In both equations, ν_j represents the stoichiometric reaction coefficient of the j^{th} species in the reaction. If the first term is available in the literature for many minerals and aqueous species, the lack of experimental data for high pressure and temperature conditions requires theoretical compensation.

If we define:

$$Eq.9: \; G_{j\,P,T}^{0} - \; G_{j\,Pr,Tr}^{0} = \; - S_{j\,Pr,Tr}^{0}(T - T_r) + \; \int_{Tr}^{T} C_{j\,Pr}^{0} dT - T \; \int_{Tr}^{T} C_{j\,Pr}^{0} dlnt + \; \int_{Pr}^{P} V_{j\,T}^{0} dP$$

It is evident that the partial molal entropy at the reference temperature and pressure ($S_{j\,Pr,Tr}^{0}$), the temperature dependence of the isobaric standard partial molal heat capacity ($C_{j\,Pr}^{0}$), and the pressure dependence of the standard partial molal volume ($V_{j\,T}^{0}$) are required to properly calculate the logK values of a reaction. Alongside, the partial molal enthalpy ($H_{j\,Pr,Tr}^{0}$) is required for the calculation of the true standard Gibbs free energy.

a) Mineral free energies at high pressures and temperatures: Berman Equations

The thermoelastic properties of minerals are calculated through the approach proposed by Berman (1988), with a modification for Na- and K- bearing minerals (Sverjensky et al., 1991). The following equations are used:

$$Eq.10: C = K_1 + K_2 T^{-0.5} + \; K_3 T^{-2} + \; K_4 T^{-3}$$

$$Eq.11: \frac{V^{P,T}}{V^{Pr,Tr}} = 1 + \; v_1(P - \; P_r) + \; v_2 + \; (P - P_r)^2 + \; v_3(T - T_r) + \; v_4(T - T_r)^2$$

Where K_1, K_2, K_3, K_4, v_1, v_2, v_3 and v_4 are empirical parameters fit to experimental data. The partial molal entropy ($S^0_{j\,Pr,Tr}$,) and partial molal enthalpy ($H^0_{j\,Pr,Tr}$) are available for several minerals in the literature.

b) Aqueous species free energies at high pressures and temperatures: Helgeson – Kirkham – Flowers (HFK) equations of state

The critical point of the modelling of an aqueous system is the choice of the best equation(s) of state for aqueous species at the conditions of the investigation. Many different approaches have been proposed and discussed in the literature (Anderson, 2017; Miron et al., 2019). No equation best suits every pressure-temperature condition, especially at extreme conditions such as close to the supercritical point of water. The DEW model is based on the Helgeson – Kirkham – Flowers (HKF) approach (Helgeson and Kirkham, 1974a, b, 1976; Helgeson et al., 1981), which forms the base for all the subsequent revisions and extensions (Shock and Helgeson, 1988; Shock et al., 1997; Sverjensky et al., 1997). To improve the readability of this thesis chapter, here I present only simplified HFK equations of state, listed as Eq.12-15:

$$Eq.12: \; H_j^0 = H_j^R + f_{Hi}\,(a_1, \dots, a_4, c_1, c_2, \omega)$$

$$Eq.13: \; G_j^0 = G_j^R - S_j^R(T - T^R) + f_{Gi}\,(a_1, \dots, a_4, c_1, c_2, \omega)$$

$$Eq.14: \; S_j^0 = S_j^R + f_{Si}\,(a_1, \dots, a_4, c_1, c_2, \omega)$$

$$Eq.15: \; C_j^0 = C_j^R + f_{Ci}\,(a_1, \dots, a_4, c_1, c_2, \omega)$$

Where the parameters between brackets are the integration constants for the volume (a), heat capacity (c) and temperature and pressure properties of water (ω). The R apex stands for the standard state properties in water. As the parameter ω is involved in the HKF method, a valid characterisation of water is needed to have solid thermodynamic modelling of aqueous geochemistry. The dielectric constant of water has been calibrated up to 6 GPa and 1200 °C (Sverjensky et al., 2014a). The primary use of Eq. 12-15 is to allow calculation and prediction of the standard partial molal free energies of each aqueous species, from simple and monoatomic ions to neutral species, complexes, and organic compounds. The integrated free energies are less sensitive to uncertainty than the derivate properties, as the HKF approach was built on the need for estimation algorithms in the perspective of the lack of thermoelastic properties for most of the aqueous species at high pressure and temperatures. Ideally, these equations would be fitted to experimental data over a broad range of conditions. Sadly, the current scientific literature does not provide experimental data at "geological" pressures and temperatures. The built-in algorithm has therefore proved to be an unmatched strength of the HKF approach. However, a very common situation is that no experimental volumes, compressibilities and heat capacities are available at 25 °C and 1.0 bar. This is most common for aqueous metal complexes, both inorganic and organic. To compensate for this lack of empirical data, an estimation algorithm has been implemented in the DEW model (Shock et al., 1997; Sverjensky et al., 1997). Consequently, a predictive scheme is now available for estimating the thermodynamic properties of poorly characterised aqueous species.

2.2.3 The modelling approach

Once the chemical and thermoelastic parameters for each phase in the system have been defined, the thermodynamic modelling of an aqueous system is possible. The DEW model does

not work with the Gibbs free energy minimisation (GEM); instead, a mathematical system is considered, where all the reactions involving aqueous species are considered simultaneously:

$$\begin{cases} Eq.16: logK_j = \dfrac{\Delta G^0_{r,j}{}_{P,T}}{-2.303RT} \\ Eq.17: m_{k,\ fluid} = \Sigma m_{k,j} \\ Eq.18: q_{k,\ fluid} = \Sigma q_{k,j} \end{cases}$$

Eq.16 is Eq.6 applied for all the aqueous species in the fluid. Eq.17 and Eq.18 are, respectively, mass and charge balance between the fluid and the aqueous species. Solving this system will result in a unique solution (the number of equations is equal to the number of variables) for the activity and concentration of each aqueous phase and, therefore, the composition and speciation of the fluid. Finally, the fluid's saturation state concerning the minerals can be calculated by applying Eq.2 for each possible mineral dissolution reaction. Because the fluid changes composition at each step of the metasomatic reaction (where each unit of the reaction progress (ξ) corresponds to 1.0 moles of the reactant rock being destroyed), this mathematical system is solved for each step with a new set of results. Therefore, it is possible to simulate the fluid-rock interaction as the magnitude of the metasomatic interaction progressively increases and evaluate the influence of the host rock over the fluid, and *vice-versa*.

2.3 PROCEDURE DEVELOPMENT

2.3.1 Procedure

Over the last thirty years, thermodynamic modelling has been proven to be a powerful tool and provided otherwise inestimable results of geological processes from domains inaccessible to sampling or experiment. However, modelling without empirical checks might generate

inaccurate data due to the intrinsic limitation of the database, as only a small fraction of the natural minerals and aqueous species are represented. Despite the theoretical character of thermodynamic modelling, natural samples still play a fundamental role in the modelling process, both for calibrating the procedure (i.e., testing the input parameters) and for corroborating the results. Generally speaking, natural samples provide better constraints than experiments, as they represent a complex chemical system that can hardly be reproduced in the lab. Still, complex and dynamic geological events sometimes cannot be modelled adequately within the current state of the art. Therefore, experiments are always required for model calibration as they provide accurate and precise results about a simpler chemical-mineralogical system with reduced and controlled variables. The procedure used in this work is described below. A schematic flowchart of the procedure is shown in **Fig. 2.2** and a step-by-step example is described in Appendix A.

Step 1: Definition of the environmental parameters

This step identifies the pressure, temperature, oxygen fugacity, and chemical system that best describe the system under study. Here, extensive bibliographic research must be conducted to define suitable environmental conditions for the target geological system. If the average P – T – fO_2 conditions can be easily obtained from previous studies and only need to be compared to the calibration range of the software (**Fig. 1.3**), the choice of the bulk composition is a critical point. In fact, the availability of thermodynamic and thermoelastic data of solid and aqueous phases in the database limits the elements that can be modelled. A simplistic bulk composition would not be sufficient to model a reliable natural system. At the same time, an excessive number of elements may result in the inability of the software to adequately describe the system's behaviour due to the lack of solid and aqueous phases bearing specific elements. A clear example of this concept is Cr, which has been proven relevant in diamond inclusion

formation (Aulbach et al., 2002). The DEW database used in this work does not allow the modelling of the Cr behaviour as no minerals or aqueous species are available for this element. Therefore, adding Cr to the system would result in its permanence in the fluid as Cr^{2+} or Cr^{3+}, altering the charge balance without contributing to any chemical evolution and only destabilising the system.

In this work, we used the K–Na–Ca–Mg–Fe–Al–Si–Cl–C–O system (K and Cl are not considered when eclogitic fluids are involved), reflecting the major element composition of Terrestrial (Pearson et al., 2014; Sverjensky and Huang, 2015; Gonzaga et al., 2010; Farré- de-Pablo et al., 2020; Liu et al., 2022; Lu et al., 2022) and Martian (Gleason et al., 1997; Treiman, 2005; Beck et al., 2006; Howarth et al., 2014; Udry et al., 2017) rocks. The database adequately represents each element in both solid and aqueous species. For Chapters 3 and 4, models have been run at 5 GPa, 1000 °C, and logfO_2 = ΔFMQ -2 to -4, overlapping the average P-T-X-fO_2 conditions for lithospheric diamond inclusion formation (Stachel and Harris, 2008; Stachel and Luth, 2015). For Chapter 5, the P-T-X-fO_2 conditions used (P = 0.5 GPa, T = 300-800 °C, logfO_2 = ΔFMQ 0 to -3) are relevant to the depth where the crust-mantle boundary is considered to be located (~40 km) (Righter et al., 2008; Knapmeyer-Endrun et al., 2021).

Step 2: Fluid modelling

The aqueous speciation and solubility code EQ3 (Woolery, 1983, 1984, 1992) has been used to model the aqueous phase. Pressure and temperature are constants, and oxygen fugacity is initially set as fixed. Still, the software can slightly modify it to meet the charge and mass balance requirements (see Paragraph 2.2.3). Then, modifications of the logK of a specific reaction (for example, Eq. 1) are made to match recent experimental data and improve the model's calibration when available. These modifications are equivalent to changing the logK

value in the database, but they are quicker to make and often related to a specific P-T-X system unsuitable for all applications.

	Eclogitic	**Peridotitic**	**Carbonatitic**
Variable	**Set with**	**Set with**	**Set with**
K	-	Phlogopite	Fixed
Na	Fixed	Fixed	Fixed
Ca	Diopside (0.350)	Grossular (0.100)	Calcite (0.500)
Mg	Pyrope (0.352)	Forsterite (0.920)	Magnesite (0.450)
Fe	Almandine (0.323)	Fayalite (0.080)	Fayalite (0.080)
Al	Grossular (0.326)	Pyrope (0.800)	Grossular (0.300)
Si	Coesite	Clinoenstatite (0.955)	Forsterite (0.920)
Cl	-	Fixed	Fixed
C	Fixed/Diamond	Fixed/Diamond	Diamond
pH	Jadeite (0.539)	Jadeite (0.015)	Fixed
$f\mathbf{O_2}$	Fixed	Fixed	Fixed

Table 2.1 - Composition of mineral assemblages and model parameters for eclogitic, peridotitic and carbonatitic fluids for Chapters 3 and 4. Note that the compositions of the fluids are not shown here, as different amounts of carbon have been considered. The geochemistry of the fluids is reported in Table 3.1 and B.3 instead.

Finally, each element considered in the chemical system needs to be set in equilibrium with a mineral endmember or treated as a fixed term to calculate its concentration in the fluid,

following the mathematical approach described in Paragraph 2.2.3. Therefore, the mineralogical association chosen defines the chemical composition of the aqueous phase, leading to the model of different fluids.

For Chapters 3 and 4, the initial fluid compositions we used are designed to mirror endmember compositions of fluid inclusions from diamonds described in the literature (i.e., silicic, peridotitic and carbonatitic; Weiss et al., 2009, 2022), which are equilibrated with a specific mantle rock (e.g., mineral assemblage; **Table 2.1**). The silicic fluid is based on an experimental calibration of aqueous fluid in equilibrium with a mafic eclogite (Kessel et al., 2015), documented in (Huang and Sverjensky, 2020). For the peridotitic and carbonatitic fluids, we chose the peridotite and carbonated dunite used to model the fluid endmembers to form Panda diamonds (Huang and Sverjensky, 2020), with garnet instead of spinel to match the higher temperature and pressure. We assumed an ideal site- mixing of garnet (pyrope, grossular and almandine) and dolomite (calcite, magnesite, and siderite) endmembers and a non-ideal site-mixing of clinopyroxene endmembers (diopside, clinoenstatite, hedenbergite, and jadeite). The clinopyroxene solid solutions were calibrated using natural samples of diamond inclusions as described previously (Huang and Sverjensky, 2020; Mikhail et al., 2021).

For Chapter 5, the fluid is an unknown variable, as no compositions are available in the literature. Mars is a telluric planet, and there is no doubt that there was (and is) magmatism. Likely, the Martian interior is not different from the Terrestrial one (Lenardic et al., 2004; Lapen et al., 2017). The Martian interior is not anhydrous, evidenced by the presence of hydrated magmatic minerals in Martian basalts (e.g., apatite and amphibole) (McCubbin et al., 2016). Besides, solid macro-molecular carbon (MMC) and gaseous organic carbon components have been found in Martian basalts (Blamey et al., 2015) in the co-association with high-temperature magmatic minerals (Steele et al., 2012). Therefore, the choice of using a peridotite (Howarth et al., 2014) as lithology to calibrate the fluid phase is coherent with the current

knowledge of the interior of Mars. The composition of the mineral assemblage and model parameters used for modelling are shown in **Table 2.2**.

mol/Kg	Equilibrium with	300 ºC	400 ºC	500 ºC	600 ºC	700 ºC	800 ºC
Na	Fixed	0.50	0.50	0.50	0.50	0.50	0.50
K	Fixed	0.50	0.50	0.50	0.50	0.50	0.50
Ca	Diopside (0.26)	$0.22x10^{-5}$	0.85×10^{-5}	0.22×10^{-4}	0.59×10^{-4}	0.15×10^{-4}	$0.30x\ 10^{-3}$
Mg	Forsterite (0.65)	0.17	0.28	0.32	0.30	0.25	0.19
Fe	Fayalite (0.35)	$0.34x10^{-4}$	$0.18x10^{-3}$	$0.38x10^{-3}$	$0.37x10^{-3}$	$0.41x10^{-3}$	$0.47x10^{-3}$
Si	Enstatite (0.41)	0.06	0.01	0.16	0.24	0.28	0.30
Al	Spinel	0.14	0.15	0.21	0.26	0.27	0.26
C	Fixed	0.50	0.50	0.50	0.50	0.50	0.50
Cl	Fixed	0.50	0.50	0.50	0.50	0.50	0.50
pH	Charge balance	8.08	7.58	7.38	7.30	7.27	7.32
fO_2		-35.45	-28.72	-23.81	-20.07	-17.13	-14.75
ΔFMQ		0	0	0	0	0	0

Table 2.2 - Chemical composition (molality concentration [moles/kg H_2O]) for selected peridotitic fluids at 0.5 GPa, between 300 and 800 ºC, and logfO_2 = 0 ΔFMQ for Chapter 5.

Step 3: Definition of the reactant host-rock

Host-rock is intended as the lithology that interacts with the fluid during the modelled metasomatic process. The mineralogical and geochemical compositions of the host rocks are from natural samples which best suit the previously selected environmental parameter in Step 1. This approach is needed to avoid considering a metasomatic process involving

disequilibrium mineral assemblages, leading to studying a different geological system than the one required by this study.

Rock	Mineral composition (% in volume)
Lherzolite	51% ol ($Fo_{0.933}Fa_{0.067}$), 18% opx ($En_{0.938}Fe_{0.062}$), 26% cpx ($Di_{0.294}Hdn_{0.088}Ja_{0.015}En_{0.603}$), 5% grt ($Py_{0.733}Gr_{0.137}Alm_{0.130}$)
Harzburgite	71% ol ($Fo_{0.933}$ $Fa_{0.067}$), 24% opx ($En_{0.938}Fe_{0.062}$), 5% grt ($Py_{0.733}Gr_{0.137}Alm_{0.130}$)
Dunite	83% ol ($Fo_{0.933}$ $Fa_{0.067}$), 5% opx ($En_{0.938}Fe_{0.062}$), 7% cpx ($Di_{0.294}Hdn_{0.088}Ja_{0.015}En_{0.603}$), 5% grt ($Py_{0.733}Gr_{0.137}Alm_{0.130}$)
Eclogite type 1	41% cpx ($Di_{0.200}Hdn_{0.100}Ja_{0.700}En_{0.000}$), 26% grt ($Py_{0.600}Gr_{0.100}Alm_{0.300}$), 33% coe
Eclogite type 2	19% cpx ($Di_{0.200}Hdn_{0.100}Ja_{0.700}En_{0.000}$), 39% grt ($Py_{0.333}Gr_{0.334}Alm_{0.333}$), 42% coe
Eclogite type 3	25% cpx ($Di_{0.200}Hdn_{0.100}Ja_{0.700}En_{0.000}$), 75% grt ($Py_{0.200}Gr_{0.600}Alm_{0.200}$)
Websterite	5% ol ($Fo_{0.920}$ $Fa_{0.080}$), 40% opx ($En_{0.750}Fe_{0.250}$), 50% cpx ($Di_{0.560}Hdn_{0.020}Ja_{0.020}En_{0.400}$), 5% grt ($Py_{0.500}Gr_{0.250}Alm_{0.250}$)
Orthopyroxenite	3% ol ($Fo_{0.890}$ $Fa_{0.110}$), 92% opx ($En_{0.900}Fe_{0.100}$), 5% grt ($Py_{0.700}Gr_{0.100}Alm_{0.200}$)
Clinopyroxenite	5% ol ($Fo_{0.930}$ $Fa_{0.070}$), 90% cpx ($Di_{0.700}Hdn_{0.025}Ja_{0.250}En_{0.025}$), 5% grt ($Py_{0.250}Gr_{0.500}Alm_{0.250}$)

Table 2.3 - Mineralogical and solid solution compositions of mantle rocks used during fluid-rock interaction for Chapter 3 and 4.

For Chapters 3 and 4, the mineralogy (geochemistry) of the reactant rocks is benchmarked to nature using empirical data from natural samples: peridotites (Pearson et al., 2014), eclogites (Pearson et al., 2014; Sverjensky and Huang, 2015) and pyroxenites (Gonzaga et al., 2010; Farré-de-Pablo et al., 2020; Liu et al., 2022; Lu et al., 2022). Three lithologies represent each rock family with different mineral abundances and solid solution compositions (**Table 2.3**).

The decision to include pyroxenites was taken due to the predicted relationship between diamonds and pyroxenites, as suggested by (Kiseeva et al., 2016).

For Chapter 5, Natural data from Martian meteorites constrain the mineralogy and geochemistry of reactant mafic and ultramafic mantle rocks (**Table 2.4**): lherzolite (Howarth et al., 2014), dunite (Beck et al., 2006), clinopyroxenite (Treiman, 2005), orthopyroxenite (Gleason et al., 1997), and gabbro (Udry et al., 2017).

Rock	**Mineral composition (% in volume)**
Lherzolite	55% ol ($Fo_{0.65}Fa_{0.35}$), 35% opx ($En_{0.75}Fs_{0.25}$), 10% cpx ($Di_{0.26}Hd_{0.22}Ja_{0.01}En_{0.51}$)
Dunite	90% ol ($Fo_{0.78}$ $Fa_{0.22}$), 1% opx ($En_{0.80}Fs_{0.20}$), 4% cpx ($Di_{0.40}Hd_{0.12}Ja_{0.01}En_{0.47}$), 5% mag
Clinopyroxenite	15% ol ($Fo_{0.45}$ $Fa_{0.55}$), 80% cpx ($Di_{0.26}Hd_{0.30}Ja_{0.01}En_{0.43}$), 3% pl ($Ab_{0.59}An_{0.37}Kf_{0.04}$), 2% mag
Orthopyroxenite	95% opx ($En_{0.70}Fs_{0.30}$), 5% mag
Gabbro	2% ol ($Fo_{0.05}$ $Fa_{0.95}$), 46% cpx ($Di_{0.12}Hd_{0.43}Ja_{0.01}En_{0.44}$), 50% pl ($Ab_{0.48}An_{0.52}Kf_{0.00}$), 2% mag

Table 2.4 - Mineralogical and solid solution compositions of mantle rocks used during fluid-rock interaction for Chapter 5.

Step 4: Modelling fluid-rock interaction

The chemical mass transfer code EQ6 (Woolery, 1983, 1984, 1992) has been used to model metasomatic interaction. Pressure and temperature are fixed, leading to an isobaric and isothermal model. Oxygen fugacity is free to change to match the variation in the geochemistry of both solid and aqueous phases. During the modelled metasomatism, the fluid directly controls the precipitation of metasomatic minerals and the dissolution of the host rock. A step-by-step evolution of the metasomatic system is calculated, where each unit of the reaction progress (ξ) corresponds to 1.0 moles of the reactant rock being destroyed and absorbed by the fluid. The fluid-rock interaction proceeds until thermodynamic equilibrium is achieved. The

modelling results in the fluid speciation of aqueous anions, metal complexes, and neutral species, alongside the mineralogical and geochemical evolution of metasomatic minerals. As this process destroys a progressively higher amount of the reactant rock, the fluid reciprocates the dissolution reactions modifying the fluid composition and geochemistry of the metasomatic minerals precipitated.

Step 5: Analysis of results

If no errors are found in the output files, *ad-hoc* Python scripts are executed to plot the selected data. The scripts are built exploiting the organisation of the EQ6 output file, where every step (defined by the reaction progress ξ) has the same layout of results. The data are stored in tables and then used to produce single-model and multi-model plots. When natural data are available and significant, the models are plotted against them to verify the agreement.

2.3.2 Previous work

The procedure previously described has been tested using the extensive literature on diamond formation and inclusions, ultimately leading to the publication of Mikhail et al. (2021) (*Geochemical Perspective Letters*), in which I am the second author. Diamonds are metasomatic products (Shirey et al., 2013; Miller et al., 2014). Experimental data (Kessel et al., 2015; Förster et al., 2019) and the cation concentration in fluid inclusions (Navon et al., 1988; Weiss et al., 2015) show that aqueous fluids contain all the required elements to precipitate silicates under mantle conditions. These data are demonstrated to be coherent with syngenetic silicate inclusions in diamonds (Harris, 1968; Mikhail et al., 2019b).

The DEW model is designed to simulate fluid-rock interaction, so diamond formation is a suitable target for calibrating this procedure. Therefore, we tested if the DEW model is capable

of predicting the chemical evolution of garnet and clinopyroxene observed as silicate inclusions in mantle diamonds (Stachel and Harris, 2008). The environmental parameters selected are relevant for diamond formation in the SCLM (5 GPa, 1000 °C and logfO_2 = -1 to -6 ΔFMQ) (Stachel and Luth, 2015). We considered a fluid originally in equilibrium with a mafic eclogitic assemblage interacting with three different peridotites (lherzolite, harzburgite and dunite). The fluid has been calibrated through the fluid-rock equilibrium experimentally determined by Kessel et al. (2015) for a K-free mafic eclogite. The mineralogical and geochemical compositions of the host rocks are taken from natural data from Pearson et al. (2014).

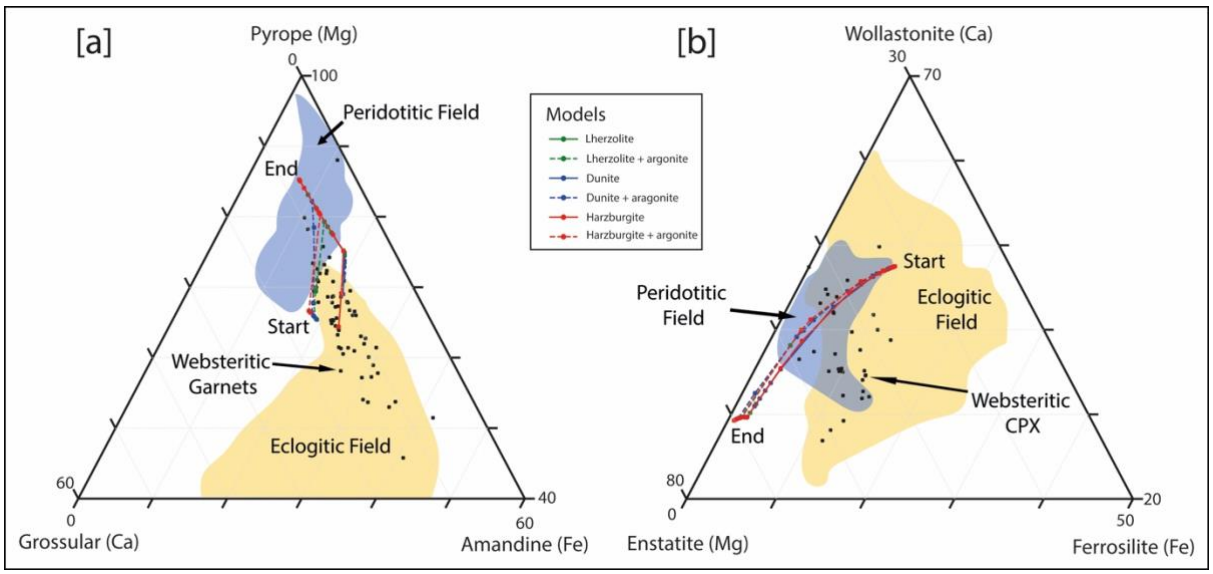

Figure 2.3 - Results of the metasomatic interaction between an eclogitic fluid and a set of peridotites for a) garnet and b) clinopyroxene at 5 GPa, 1000 °C and logfO_2 = -3 ΔFMQ. Figure reproduced from (Mikhail et al., 2021).

The models show that garnet, clinopyroxene and orthopyroxene are the main silicate phases precipitated during the metasomatic reaction, with olivine (Fo93) formed only in the very last step of the models and always less than < 1 vol.%. The metasomatic reaction converted a refractory garnet-peridotite into a fertile garnet-websterite. In **Fig. 2.2**, we plotted the

modelling outputs against the geochemistry of natural garnet and clinopyroxene inclusions in diamonds (Stachel and Harris, 2008). The mineral phases become progressively Mg-rich during the reaction, connecting the peridotitic and eclogitic fields through the websteritic "bridge" along a single reaction pathway. These models are capable of reproducing natural data, and metasomatic minerals are shown to be susceptible to variations in the fluid composition, as expected. For example, the geochemistry of both garnet and clinopyroxene shift to Ca-richer composition by adding aragonite to the system. Our modelling approach is, therefore, capable of reproducing natural data with good agreement.

CHAPTER 3

THE IMPORTANCE OF CARBON TO THE FORMATION AND COMPOSITION OF SILICATES DURING MANTLE METASOMATISM

3.1 ABSTRACT

Mineral and fluid inclusions in mantle diamonds provide otherwise inaccessible information concerning the nature of mantle metasomatism and the role of fluids in the mass transfer of material through the Earth's interior. We explore the role of the carbon concentration during fluid-rock metasomatism in generating the range of garnet and clinopyroxene compositions observed in diamonds from the sub-continental lithospheric mantle. We use the Deep Earth Water model to predict the results of metasomatic interactions between silicic, carbonatitic and peridotitic fluids and common mantle rocks (peridotites, eclogites and pyroxenites) at 5 GPa, 1000 ºC, across a range of redox conditions (logfO_2 = -2 to -4 ΔFMQ), and a wide range of initial carbon concentrations in the metasomatic fluids. Our results show that the predicted compositions of metasomatic garnets and clinopyroxenes are controlled by the initial compositions of the fluids and the rocks, with subsequent mineral-specific geochemical evolution following definable reaction pathways. Model carbon-rich, metasomatic fluids that can form diamond (initial C- content > 5.00 molal) result in Mg-rich garnets and clinopyroxenes typical of peridotitic, eclogitic, and websteritic inclusions in diamonds. However, model carbon-poor, metasomatic fluids that do not form diamond can result in Mg-poor, Ca-rich garnets and clinopyroxenes. Such garnets and clinopyroxenes do nevertheless occur as inclusions in diamonds. In our models, the abundance of carbon in the fluids controls the behaviour of the bivalent ions through the formation of aqueous Mg–Ca–Fe–C complexes

which directly govern the composition of garnets and clinopyroxenes precipitated during the metasomatic processes. As the C-rich initial fluids can form the higher Mg-eclogitic, peridotitic, and websteritic inclusions in diamonds, these inclusions can be syngenetic (metasomatic) or possibly protogenetic. However, in our models, the relatively Mg-poor, Ca- and Fe-rich eclogitic garnet and clinopyroxene inclusions found in mantle diamonds formed from C-poor fluids that do not form diamonds. These inclusions most likely reflect a metasomatic event prior to being incorporated into their host diamonds, or they could represent protolith-based protogenetic geochemistry. Therefore, the paragenetic groups used to classify diamonds should not be considered a genetic classification, as the role of the fluid/melt appears to be more relevant than the one played by the host rock.

Keywords: Diamond inclusions, fluid-rock metasomatism, thermodynamic modelling

3.2 INTRODUCTION

Experimental solubility data (Kessel et al., 2005a, b; Manning, 2013; Förster et al., 2019) and the cation concentration of fluid inclusions in diamonds (Navon et al., 1988; Weiss et al., 2015) show that aqueous fluids in equilibrium with mantle rocks contain all the rock-forming major and trace elements required to precipitate mantle-forming silicates (olivine, pyroxene, garnet). Therefore, the interaction(s) between rocks, fluids, and melts is Earth's most efficient mechanism for the mass transfer of material throughout the solid Earth. However, direct samples are scarce, with melt inclusions in silicates and fluid inclusions in diamonds being rare exceptions (Weiss et al., 2022). Owing to their robust and inert nature, mantle diamonds are extraordinary archives which provide otherwise inaccessible samples of solids, liquids, and gaseous material from Earth's interior. Diamonds have formed over more than 75% of Earth's history (Gurney et al., 2010; Koornneef et al., 2017; Gress et al., 2021), with most forming in

the sub-continental lithospheric mantle (120 – 180 km; Stachel and Harris, 2008; Stachel et al., 2022). Therefore, the geochemistry of diamond inclusions preserves the most detailed and intact history of mantle metasomatism.

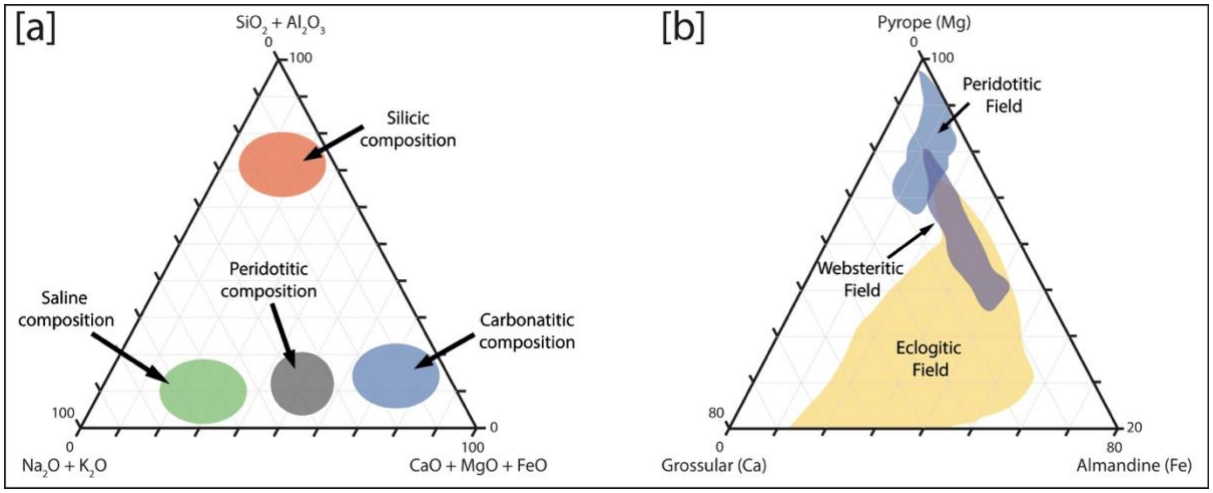

Figure 3.1 - Fluid and solid inclusions in diamonds: a) Fluid inclusion compositions; (Weiss et al., 2022); b) Mineral inclusions from numerous sources (see Methods). The poorly defined websteritic data cluster connects the peridotitic and eclogitic fields and represents different steps of a metasomatic evolution (Mikhail et al., 2021).

Diamonds are metasomatic precipitates (Shirey et al., 2013; Miller et al., 2014). Their crystallisation can be driven by the transport of carbon-bearing material across adiabatic, isobaric, and isothermal geochemical gradients (Jacob et al., 2014, 2016; Luth and Stachel, 2014; Palyanov et al., 2015; Stagno et al., 2015; Sverjensky and Huang, 2015; Mikhail et al., 2021).

The geochemistry of fluid inclusions in diamonds reveals four compositional groups, termed silicic, peridotitic, carbonatitic and saline (Navon et al., 1988; Izraeli et al., 2001; Tomlinson et al., 2006; Weiss et al., 2009, 2014, 2022; Timmerman et al., 2021) (**Fig. 3.1a**). The origin of diamond-forming fluids has been examined by experimental (e.g., Kessel et al., 2015; Bureau

et al., 2018; Förster et al., 2019; Sonin et al., 2022; Meltzer and Kessel, 2022) and theoretical approaches (Huang and Sverjensky, 2020; Mikhail et al., 2021), alongside studies predicting the geochemistry of diamond-forming fluids which would be in equilibrium with solid silicate inclusions (e.g., Stachel and Harris, 2008; Aulbach et al., 2008; Mikhail et al., 2019a).

Compared with the geochemistry of the fluid inclusions in diamonds, the composition of the mineral inclusions is more diverse (e.g., garnet compositions in **Fig. 3.1b**). Many mineral groups have been found as inclusions in diamonds, including sulfides, silicates, oxides, carbonates, and metallic phases (Stachel and Harris, 2008). However, one can subdivide these minerals into four groups: peridotitic, eclogitic, websteritic, and exotic metallic phases (Stachel et al., 2022).

The inclusion classification schemes for both fluids and minerals are empirical; therefore, fluid and mineral classifications do not diagnostically inform us about petrogenetic processes (Mikhail et al., 2021). In particular, the diversity of the petrological characteristics and the complexity of structural and textural elements leave the interpretation of the genetic relationships between diamonds and their mineral inclusions unclear. The mineral inclusions either reflect a pre-metasomatic heterogeneity in the host rock in the upper mantle (Pasqualetto et al., 2022), or they are the result of metasomatism coeval with diamond formation (Aulbach et al., 2002; Kiseeva et al., 2016; Mikhail et al., 2019b), or both options. Therefore, diamonds and their mineral inclusions can be either syngenetic (Harris, 1968; Mikhail et al., 2019b) or protogenetic (Nestola et al., 2017).

This contribution aims to investigate the geochemistry of silicates formed during isobaric (5 GPa) and isothermal (1000 ºC) fluid-rock metasomatism benchmarked to the geochemistry of diamond inclusions. Specifically, we focused on garnets and clinopyroxenes because both are present in significant abundance in peridotitic, eclogitic, and websteritic paragenetic groups (Stachel et al., 2022).

3.3 METHOD

3.3.1 Modelling approach

Conceptually, our computational thermodynamic model involves two steps. Firstly, a fluid is equilibrated with a rock (EQ3 in **Fig. 3.2**). Secondly, this fluid migrates and interacts with a collection of mineral phases (a rock) at the same (fixed) pressure and temperature (EQ6 in **Fig. 3.2**). The fluid in step 2 is out of equilibrium with the rock, and this drives irreversible chemical reactions which produce new mineral phases while concurrent changes to the geochemistry of the fluid are reciprocated (e.g., Huang and Sverjensky, 2020; Mikhail et al., 2021).

3.3.2 Model parameterisation

The range of initial carbon contents of the fluids used in the modelling can be related to different geological contexts, from the breakdown of hydrous wadsleyite into olivine + H_2O during the rising of a plume in the subcontinental lithosphere (low carbon fluids) to a fluid migrating from sediments carried downwards by the slab in a subduction zone (high carbon fluids; Poli, 2015; Tumiati et al., 2017; Yaxley et al., 2021). The P-T-X-fO_2 conditions we used (P = 5 GPa, T = 1000 ºC, logfO_2 = -2 to -4 ΔFMQ) overlap with the average P-T-X-fO_2 conditions for lithospheric diamond inclusion formation where the average inclusion entrapment temperature is 1155 ± 105 °C (n = 444) and pressure is 5.3 ± 0.8 GPa (n = 157) (Stachel and Harris, 2008; Stachel and Luth, 2015).

Fluid-rock interaction is complex and dynamic, where solid and fluid phases interact progressively. This results in irreversible geochemical evolution. Thermodynamic modelling of fluid-rock interaction above 0.5 GPa was precluded until the dielectric constant of water was constrained at ≤ 6 GPa (Sverjensky et al., 2014a). Therefore, we can apply the Helgeson-Kirkham-Flowers (HKF) equations of state for aqueous speciation (Helgeson and Kirkham, 1974a, b, 1976; Helgeson et al., 1981; Tanger and Helgeson, 1988; Shock and Helgeson, 1988;

Sverjensky et al., 1997) up to 6 GPa and 1200 ºC (Pan et al., 2013; Sverjensky et al., 2014a; Facq et al., 2014). As a result, it is now possible to model the fluid speciation of aqueous anions, metal complexes, and neutral species and their interaction with minerals across pressure and temperature conditions that resemble those from the surface and down to ca. 150 km inside planet Earth (Huang and Sverjensky, 2019, 2020; Mikhail et al., 2021).

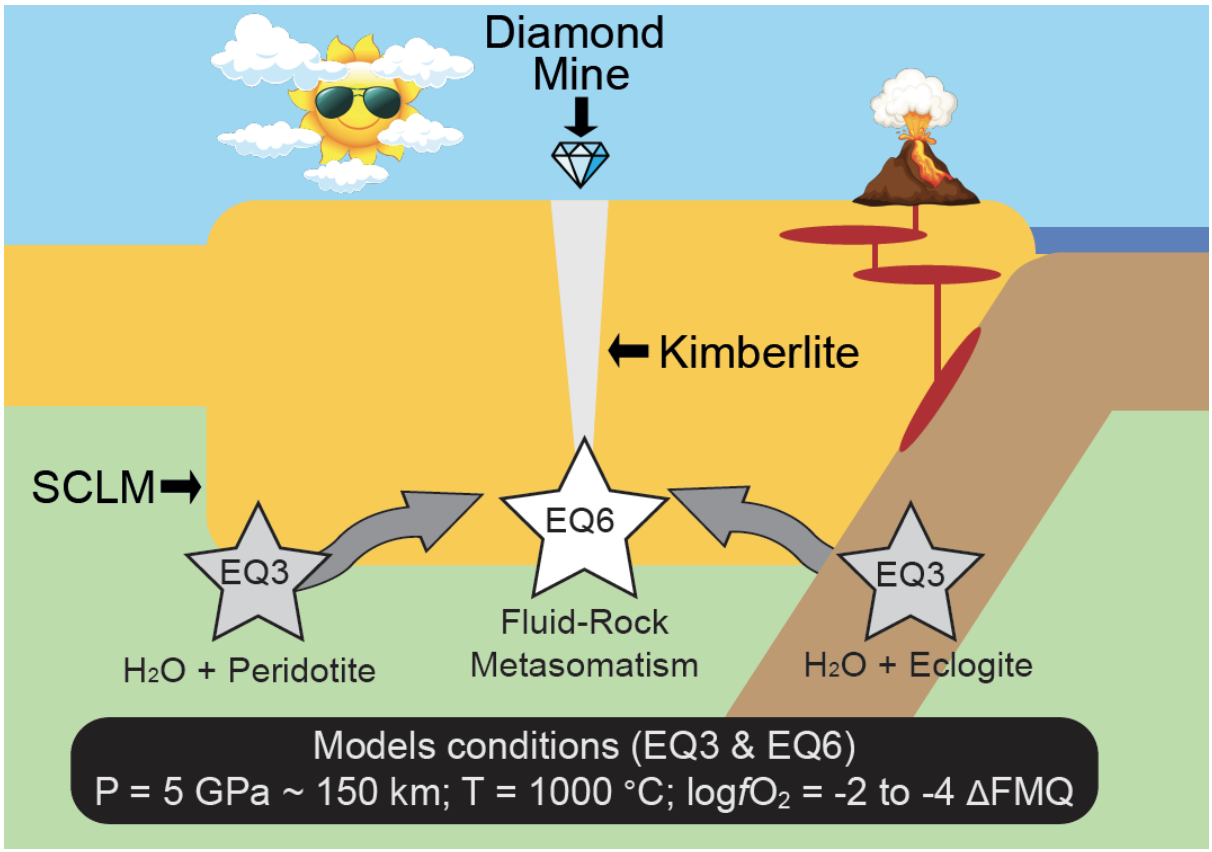

Figure 3.2 - Cartoon illustrating our conceptual modelling approach. We calculate the fluid composition for a given rock in equilibrium with water (EQ3), and then we compute the reaction of the resulting fluid with different lithologies (EQ6). Note that there are no spatial dimensions to our models. The fluid migration arrows shown above illustrate – contextually – the formation and migration of a mantle fluid which migrates into the cratonic lithosphere and reacts with rocks that it encounters (i.e., simulating fluid metasomatism in the SCLM).

The initial fluid compositions used are designed to mirror the fluids found as diamond inclusions described in the literature (i.e., silicic, peridotitic and carbonatitic; Weiss et al., 2009, 2022; **Fig. 3.1a**), which are equilibrated with a specific mantle rock (e.g., mineral assemblage; **Table 3.1**, **Table B.1 – B.3**). The silicic fluid is based on an experimental calibration of aqueous fluid in equilibrium with a mafic eclogite Kessel et al. (2015) (later referred to as an eclogitic fluid), documented in (Huang and Sverjensky, 2020). For the peridotitic and carbonatitic fluids, we chose the peridotite and carbonated dunite used to model the fluid endmembers to form Panda diamonds (Huang and Sverjensky, 2020), with garnet instead of spinel to match the higher temperature and pressure. We assumed an ideal site-mixing of garnet (pyrope, grossular and almandine) and dolomite (calcite, magnesite and siderite) endmembers and a non-ideal site-mixing of clinopyroxene endmembers (diopside, clinoenstatite, hedenbergite and jadeite). The clinopyroxene solid solutions were calibrated using natural samples of diamond inclusions as described previously (Huang and Sverjensky, 2020; Mikhail et al., 2021). To study the influence of carbon abundance and speciation on the geochemistry of silicate minerals, we ran models with a fixed initial amount of carbon at $\log fO_2$ = -3 ΔFMQ (from 0 to 1.0 molal; **Table 3.1** and **B.3**) for the eclogitic and peridotitic fluids. Due to the nature of the carbonatitic fluid, it was impossible to constrain the amount of carbon with a fixed value as it would have affected the entire mineral assemblage (e.g., carbonates). Therefore, carbon was set in equilibrium with diamond for the carbonatitic fluid, and the model calculated the most stable mineral assemblage in the system. Finally, to allow the like-for-like comparison with the carbonatitic fluid, we also simulated a suite of peridotitic and eclogitic fluid-rock reactions in equilibrium with diamond (labelled as Type: Diamond in **Table 3.1** and **B.2**).

Fluid	Type	Name	C	K	Na	Ca	Mg	Fe	Al	Si	Cl	pH
Eclogitic	Low-C fluids	E_0.00	0.00	0.00	1.05	0.68	0.01	0.06	1.16	11.57	0.00	4.49
		E_0.25	0.25	0.00	1.05	0.69	0.05	0.07	1.19	11.52	0.00	4.51
		E_0.50	0.50	0.00	1.04	0.70	0.09	0.09	1.21	11.46	0.00	4.52
		E_0.75	0.75	0.00	1.04	0.72	0.13	0.10	1.23	11.41	0.00	4.53
		E_1.00	1.00	0.00	1.04	0.73	0.16	0.12	1.25	11.36	0.00	4.54
	Diamond	E_dia	3.13	0.00	1.05	0.84	0.42	0.22	1.37	10.91	0.00	4.60
Peridotitic	Low-C fluids	P_0.00	0.00	2.45	2.00	0.78	0.21	1.71	0.10	2.36	8.00	4.51
		P_0.25	0.25	2.41	2.00	0.78	0.33	1.69	0.10	2.46	8.00	4.53
		P_0.50	0.50	2.37	2.00	0.79	0.46	1.67	0.10	2.56	8.00	4.54
		P_0.75	0.75	2.34	2.00	0.80	0.58	1.65	0.10	2.66	8.00	4.55
		P_1.00	1.00	2.30	2.00	0.81	0.70	1.63	0.11	2.78	8.00	4.56
	Diamond	P_dia	5.58	1.91	2.00	1.03	2.48	1.36	0.14	4.25	8.00	4.73
Carbonatitic	Diamond	C_dia	17.96	0.50	0.50	11.13	3.01	0.68	0.72	0.08	1.00	5.80

Table 3.1 - Composition (molality concentration [moles/kg H_2O]) of eclogitic, peridotitic, and carbonatitic fluids at 5 GPa, 1000 ºC, and logfO_2 = -3 ΔFMQ.

The mineralogy (geochemistry) of the reactant rocks is benchmarked to nature using empirical data from natural samples: peridotites (Pearson et al., 2014), eclogites (Pearson et al., 2014; Sverjensky and Huang, 2015) and pyroxenites (Gonzaga et al., 2010; Farré-de-Pablo et al., 2020; Liu et al., 2022; Lu et al., 2022). Three lithologies represent each rock family with different mineral abundances and solid solution compositions (**Table 3.2**). The decision to include pyroxenites was taken due to the predicted relationship between diamonds and pyroxenites, as suggested by (Kiseeva et al., 2016).

Rock	Mineral composition (% in volume)
Lherzolite	51% ol ($Fo_{0.933}Fa_{0.067}$), 18% opx ($En_{0.938}Fe_{0.062}$), 26% cpx ($Di_{0.294}Hdn_{0.088}Ja_{0.015}En_{0.603}$), 5% grt ($Py_{0.733}Gr_{0.137}Alm_{0.130}$)
Harzburgite	71% ol ($Fo_{0.933}$ $Fa_{0.067}$), 24% opx ($En_{0.938}Fe_{0.062}$), 5% grt ($Py_{0.733}Gr_{0.137}Alm_{0.130}$)
Dunite	83% ol ($Fo_{0.933}$ $Fa_{0.067}$), 5% opx ($En_{0.938}Fe_{0.062}$), 7% cpx ($Di_{0.294}Hdn_{0.088}Ja_{0.015}En_{0.603}$), 5% grt ($Py_{0.733}Gr_{0.137}Alm_{0.130}$)
Eclogite type 1	41% cpx ($Di_{0.200}Hdn_{0.100}Ja_{0.700}En_{0.000}$), 26% grt ($Py_{0.600}Gr_{0.100}Alm_{0.300}$), 33% coe
Eclogite type 2	19% cpx ($Di_{0.200}Hdn_{0.100}Ja_{0.700}En_{0.000}$), 39% grt ($Py_{0.333}Gr_{0.334}Alm_{0.333}$), 42% coe
Eclogite type 3	25% cpx ($Di_{0.200}Hdn_{0.100}Ja_{0.700}En_{0.000}$), 75% grt ($Py_{0.200}Gr_{0.600}Alm_{0.200}$)
Websterite	5% ol ($Fo_{0.920}$ $Fa_{0.080}$), 40% opx ($En_{0.750}Fe_{0.250}$), 50% cpx ($Di_{0.560}Hdn_{0.020}Ja_{0.020}En_{0.400}$), 5% grt ($Py_{0.500}Gr_{0.250}Alm_{0.250}$)
Orthopyroxenite	3% ol ($Fo_{0.890}$ $Fa_{0.110}$), 92% opx ($En_{0.900}Fe_{0.100}$), 5% grt ($Py_{0.700}Gr_{0.100}Alm_{0.200}$)
Clinopyroxenite	5% ol ($Fo_{0.930}$ $Fa_{0.070}$), 90% cpx ($Di_{0.700}Hdn_{0.025}Ja_{0.250}En_{0.025}$), 5% grt ($Py_{0.250}Gr_{0.500}Alm_{0.250}$)

Table 3.2 - Mineralogical and solid solution compositions of mantle rocks used during fluid-rock interaction. This table is reproduced from Chapter 2 (Paragraph 2.3.1).

The model outputs a large amount of data (**Table B.4 – B.6**). The chemistry of fluids and metasomatic minerals is relevant for this study at each reaction stage until the system is fully equilibrated. Reaction progress is quantified using the reaction variable ξ, which expresses the destruction of 1.0 mole of each reactant mineral per 1.0 kg of H_2O in the initial fluid. To compare with natural data, we plotted the model results against a database of lithospheric diamond inclusion geochemistry, including the major element data for olivine (n = 1334), orthopyroxene (n = 446), clinopyroxene (n = 926) and garnet (n = 2628) (Gurney and Boyd, 1982; Gurney et al., 1984; Viljoen et al., 1998; Jacob et al., 2000; Tappert et al., 2005, 2009;

Stachel and Harris, 2008; De Stefano et al., 2009; Sobolev et al., 2009; Bulanova et al., 2010; Dobosi and Kurat, 2010; Miller et al., 2014; Mikhail et al., 2019b).

3.4 RESULTS

The results of the model runs are given in **Table B.4 – B.6**. This study focuses on the composition of the fluid and solid components, including the solid solution geochemistry of each applicable phase and the speciation of aqueous components dissolved in the fluid as a function of reaction progress (ξ). The metasomatic minerals formed during the reaction are silicates (olivine, pyroxene, garnet, coesite and meionite), oxides (magnetite and hematite), hydroxides (brucite), carbonates (dolomite), and native phases (diamond). Dolomite is formed only as an intermediate product, and the fluid reabsorbs it as the metasomatic process continues (**Table B.4**). Except for minor meionite, the mineral phases precipitated in our models are consistent with those found as inclusions in mantle diamonds (Stachel et al., 2022). Meionite is formed because the system needs to compensate for the high activities of calcium and carbon in the early stages of the fluid-rock interaction under conditions where carbonates and clinopyroxenes are not stable. As the reaction progresses, meionite is usually replaced by clinopyroxene, carbon-rich aqueous species, and occasionally, diamond. An exception is an eclogitic fluid reacting with eclogite, where meionite is preserved throughout the metasomatic process. Our models show that the precipitation of metasomatic garnets and clinopyroxenes with chemical compositions covering almost entirely the range of silicate minerals found as inclusions in diamonds is possible during fluid metasomatism of the SCLM. Garnet and clinopyroxene are present in the final stages of every model presented in this work, along with orthopyroxene and, sometimes, olivine (**Table B.4**). Herein, we focus on the chemical

evolution of garnets and clinopyroxenes because these phases are present and common in all three paragenetic diamond inclusion groups.

3.4.1 Reaction products as a function of fluid type (diamond-forming fluids)

Selected models charting the geochemical evolution of precipitated garnets and clinopyroxenes are shown in **Fig. 3.3a – f**. Consistent with the findings for eclogitic fluid-rock metasomatism reported previously (Mikhail et al., 2021), varying the silicate mineral abundances and solid-solution compositions in the host rock does not strongly influence the geochemistry of the precipitates from a given fluid. These data show, as can be expected, that those reactions with the most significant chemical disequilibrium between fluid and rock produce the broadest compositional range of silicate precipitates. For example, model runs for an eclogitic fluid reacting with a lherzolite show a wide variation in garnet and clinopyroxene compositions (**Fig. 3.3c – d**).

We find the composition of garnets precipitated from both the eclogitic and peridotitic fluids reacting with all mantle lithologies overlaps with natural diamond inclusion data on the pyrope-grossular-almandine ternary, with garnet compositions transecting the fields encompassing high-Mg eclogitic, websteritic, and peridotitic garnet inclusion compositions (**Figs. 3.3a** and **3.3c**). The composition of clinopyroxenes precipitated from the peridotitic fluid shows Mg-enrichment and Fe-depletion outside the range observed in the natural diamond inclusion dataset (**Fig. 3.3b**). Instead, the composition of clinopyroxenes precipitated from the eclogitic fluid shows substantial overlap with the natural diamond inclusion dataset in wollastonite-enstatite-ferrosilite space, crossing the field for eclogitic, websteritic, and peridotitic compositions (**Fig. 3.3d**). A similar trend is observed for the wollastonite-enstatite-ferrosilite-jadeite space (**Fig. B.2a – c**).

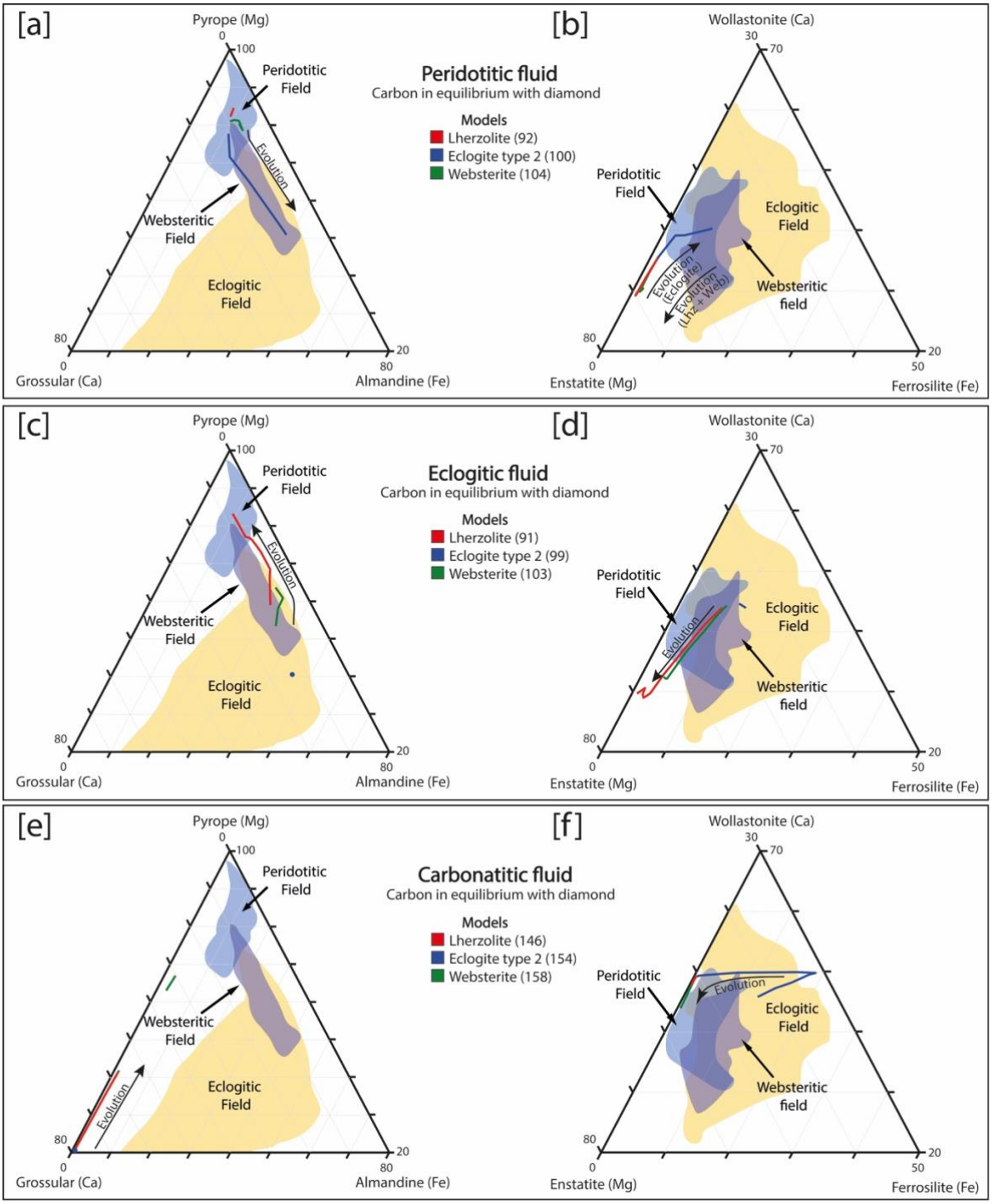

Figure 3.3 - The geochemistry of garnets and clinopyroxenes precipitated during progressive fluid-rock interaction for peridotitic (a, b), eclogitic (c, d), and carbonatitic (e, f) diamond-forming fluids with a range of host rocks (lherzolite, eclogite type 2, and websterite) at 5 GPa, 1000 ºC, and logfO_2 = -3 ΔFMQ. The initial amount of carbon in the fluids is determined by equilibrium with diamond (diamond-forming fluids) and varies from about 3 to 18 molal. The

numbers in parentheses refer to the model run number. Additional plots for clinopyroxene are shown in Fig. B.2a – c.

For the carbonatitic fluid, we find that the garnets produced have hereto unseen, very high, grossular contents because of the elevated Ca-content (dissolved Ca-carbonate) in the system (**Fig. 3.3e**) and produce clinopyroxenes with appropriate Ca/Mg ratios and severely depleted Fe contents (**Fig. 3.3f**). This means that [1] garnets found as inclusions in diamonds may have yet to experience carbonatitic metasomatism, or [2] the geochemistry of the carbonatitic fluids in our model is not a good match for the carbonatitic fluids in nature. As no experimental studies show the primary composition of diamond-forming carbonatitic fluids and fluid inclusions in natural diamonds are not primary (compositionally), the calibration of a carbonatitic fluid through natural or experimental data is not feasible at present. Therefore, we do not consider models involving this carbonatitic fluid furthermore. Still, we provide ternary diagrams showing the results for carbonatitic fluid models (**Fig. B.1** and **B.2**).

3.4.2 Reaction products as a function of the carbon content of the fluid

The trends described above for the models with carbon-rich initial fluids (i.e., diamond-forming fluids) serve as reference trends (black lines) in **Figs. 3.4a – d**. Among the most abundant dissolved carbon species in these fluids include $Ca(HCOO)^+$, $Fe(HCOO)^+$ and $Mg(SiO_2)(HCO_3)^+$ **(Table B.3** and **B.6).** Therefore, a rational assumption would be that aqueous Mg–Ca–Fe–C complexes will exert control on the behaviour of Mg^{2+}, Ca^{2+} and $Fe^{2+,}$ which would be reflected in the composition of calcium-bearing ferromagnesian silicates. Indeed, we find that the carbon content of the fluid greatly influences the chemical composition of garnets and clinopyroxenes precipitated during fluid-rock interaction.

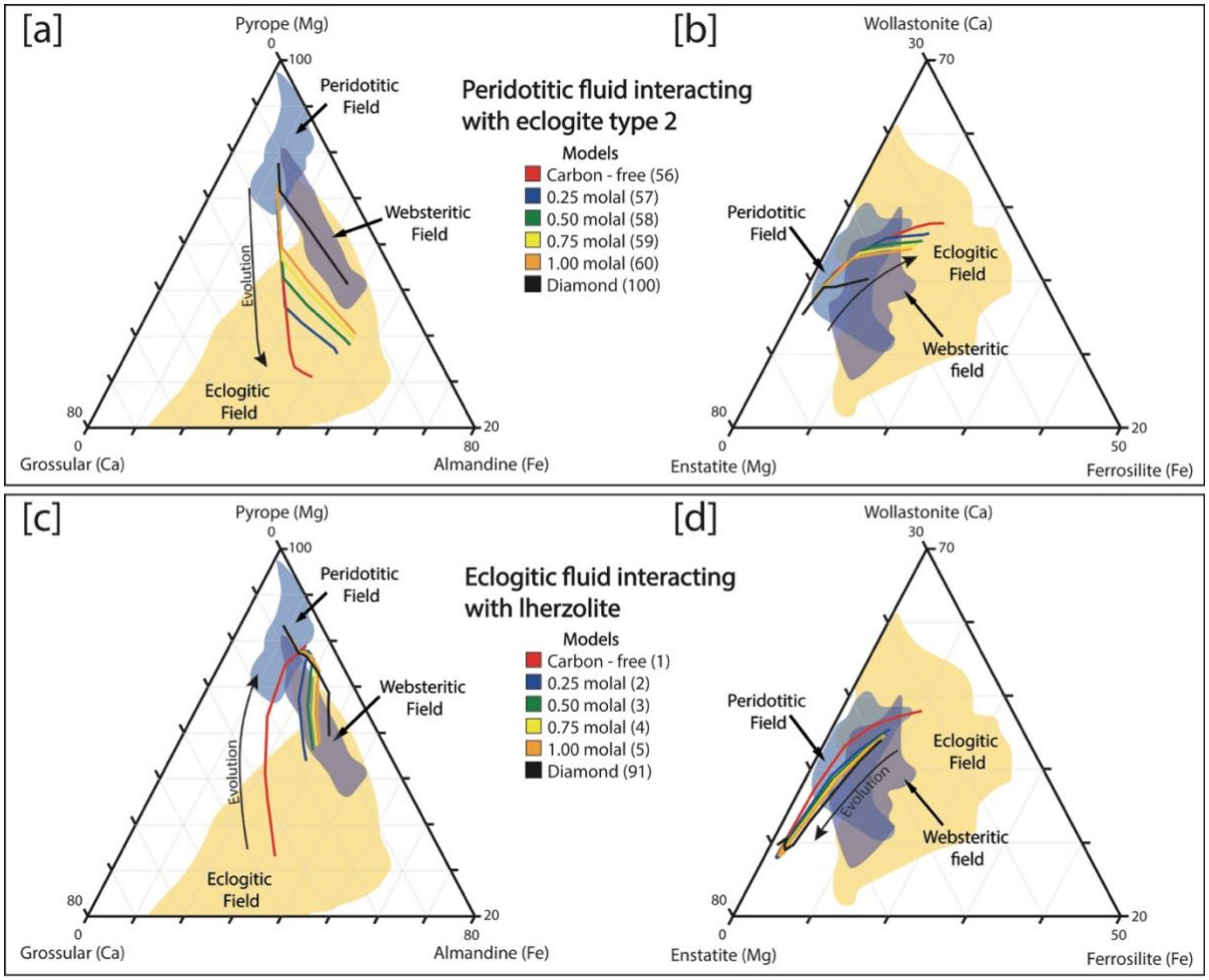

Figure 3.4 - Results for models with variable carbon contents. Garnet and clinopyroxene chemical compositions resulting from the interaction between peridotitic (a, b) and eclogitic (c, d) fluids with a range of host rocks (lherzolite, eclogite type 2, and websterite) at 5 GPa, 1000 ºC, and logfO_2 = -3 ΔFMQ. The amount of carbon varies from carbon-free to those in equilibrium with diamond. The numbers in parentheses refer to the model run number. Additional plots for clinopyroxene are shown in Fig. B.2d and B.2e.

In short, the lower the carbon content in the fluid, the lower the Mg-content in garnet and clinopyroxene precipitated (**Figs. 3.4a – d, Fig. B.2d** and **B.2e**). For example, it can be seen in **Figs. 3.4a** and **3.4c** that model carbon-poor fluids (less than or equal to 1.0 molal) show a very different chemical evolution to the carbon-rich, diamond-forming fluid in terms of the

predicted garnet compositions. In fact, the lowest carbon fluids (C-free) are consistent with garnet with pyrope contents of only 30% (**Figs. 3.4a** and **3.4c**). The same fluids are consistent with clinopyroxenes with enstatite contents as low as about 50%, and high wollastonite and ferrosilite contents (**Figs. 3.4b** and **3.4d**). The range of predicted model clinopyroxene compositions results in model trajectories which cross from the truly eclogitic (Fe-rich + Mg-poor) areas of these ternary diagrams into the Mg-rich and definitively peridotitic domain(s) (**Figs. 3.4b** and **3.4d**).

3.5 DISCUSSION

3.5.1 Chemical evolution during carbon-bearing fluid-rock interaction

The systems investigated in this study are isobaric and isothermal, where each run has a fixed starting fO_2. We observe minor (and trivial) variations in oxygen fugacity (in the second decimal place) and pH during each run. Consequently, the driving force for metasomatism is the chemical gradient established between the system's two components, a model rock and a model fluid. Our models predict that fluid-rock interaction will result in progressive silicate formation with evolving major element compositions. Both fluids and rocks play a role in mineral evolution. Counter-intuitively, host rock mineralogy is not always reflected in the geochemistry of the precipitates at each reaction stage. Instead, the geochemistry of the fluid dominates the nature of mineral precipitates in the early stages (low ξ). However, the mineral composition of the precipitates eventually converges with those of the host rock at high ξ. For example, the first garnets and pyroxenes precipitating from an eclogitic fluid reacting with a lherzolite are grossular- and diopside-rich, but the final garnets precipitating at the end of the same reaction pathway are relatively pyrope- and enstatite-rich (**Figs. 3.3c** and **3.4c**). Additionally, the clinopyroxenes formed by a peridotitic fluid reaction with a lherzolite and

websterite increase their enstatite component when the host rock is more Mg-rich than the peridotite which formed the peridotitic fluid (**Fig. 3.3b**).

We use data from lithospheric diamond inclusions (**Fig. 3.1b**) as a calibrant for model accuracy. Both eclogitic and peridotitic fluids precipitate garnet that transect (peridotitic fluid; **Fig. 3.4a**) or straddle the spread of natural data (eclogitic fluid; **Fig. 3.4c**). Carbon-poor (0.00 to 1.00 molal) fluids do not produce diamond in our models, and the composition of the resulting metasomatic garnet is Ca-rich. In contrast, diamond-forming fluids in our model produce garnet with >50% pyrope. These constraints prevent the prediction of the formation of pyrope-poor eclogitic garnet together with diamond during the same metasomatic events. However, the majority of eclogitic garnet inclusions in diamonds are pyrope-poor (**Fig. 3.1b**). A similar trend is observed for clinopyroxene, and both peridotitic and eclogitic overlap substantially with natural data. Diamond-forming fluids (initial C- content > 5.00 molal) precipitate sub-calcic clinopyroxenes (<45% Wo), while carbon-poor fluids are responsible for higher calcium content (**Fig. 3.4b** and **3.4d**).

Whilst far from encompassing the range of garnet and clinopyroxene major element compositions found in lithospheric diamonds, these models corroborate the notion that eclogitic, websteritic, and peridotitic garnet and clinopyroxene inclusions in lithospheric mantle diamonds can be genetically related to one another by the evolution of a single metasomatic event (Mikhail et al., 2021). We show that this notion holds, non-exclusively, for garnets and clinopyroxenes precipitated during the metasomatic interaction of eclogitic and peridotitic fluid with the main mantle-forming rocks (peridotite, websterite, and eclogite).

Previous experimental studies predict the coexistence of carbonates with native carbon (Yaxley and Brey, 2004; Poli et al., 2009; Dasgupta and Hirschmann, 2010; Poli, 2015), whereas our models do not predict abundant carbonate precipitation. Two reasons can be addressed: [1] the systems in this study are too reducing to stabilise carbonate minerals ($\log fO_2 \leq 0$ ΔFMQ), and

[2] the systems are carbon undersaturated. However, some of our models precipitate carbon-rich minerals (meionite, dolomite) alongside diamond. These minerals are often reabsorbed by the fluid or replaced during the metasomatic process (**Table B.4**). Therefore, if we increased the carbon content of the fluid, we would force the precipitation of carbonates and native carbon. Nevertheless, forming solid carbon phases is not the objective of this study as we focus on the range of garnet and clinopyroxene compositions produced during fluid-rock metasomatism.

3.5.2 Chemical evolution during carbon-poor fluid-rock interaction

Any individual diamond-hosted mineral inclusion is either syngenetic (Harris, 1968; Mikhail et al., 2019b) or protogenetic (Nestola et al., 2017; Pasqualetto et al., 2022)to the host diamond. If syngenetic, the formation of the inclusion in a diamond is the result of carbon-rich fluid metasomatism, according to our models. Our data imply that diamond-forming fluids cannot produce pyrope-poor garnet and wollastonite + ferrosillite-rich clinopyroxene under the conditions employed in this study. This may suggest that pyrope-poor garnet and wollastonite + ferrosillite-rich clinopyroxene inclusions are protogenetic, and their geochemistry should reflect their protolith (eclogite). Alternatively, they may reflect a previous metasomatic event before being incorporated into diamond. In both cases, the inclusions can be thought of as protogenetic, and these samples would be incredibly valuable tracers of metasomatism, mantle melting, and subduction events through deep time.

Our models predict that the amount of carbon strongly influences garnet and clinopyroxene major element compositions precipitated from the fluid. As indicated above, most carbon-poor fluids form Mg-poor and Ca-rich garnets (**Figs. 3.4a** and **3.4c**) and clinopyroxenes (**Figs. 3.4b** and **3.4d**). Metasomatic reactions for both carbon-poor peridotitic fluids (**Fig. 3.4a** and **3.4b**) and carbon-poor eclogitic fluids (**Fig. 3.4c** and **3.4d**) result in the precipitation of garnets and

clinopyroxenes deep in the eclogitic field of data, where Ca-rich phases dominate. Instead, carbon-rich fluid initially in equilibrium with diamond resulted in Mg-rich garnet (**Figs. 3.3a** and **3.3c**) and clinopyroxene (**Figs. 3.3b** and **3.3d**), covering the whole range of peridotitic and websteritic inclusions but barely entering the low-Mg eclogitic field.

As anticipated, we attribute the effects of variable carbon concentration on the silicate product minerals to the speciation of bivalent ions as Mg–Ca–Fe–C aqueous complexes during the metasomatic process. The model Mg-rich aqueous species are more abundant in the more-oxidized carbon-rich systems, consistent with experimental data (Tiraboschi et al., 2018). Evidence for the role of oxygen fugacity on the aqueous speciation is found by examining the effect of different oxygen fugacities ($\log fO_2$ = -2 to -4 ΔFMQ) on the composition of silicate precipitates during the fluid-rock interaction (**Fig. B.3**). The amount of carbon in the fluid and its speciation are susceptible to variations in the redox conditions (**Table 3.1**, **Table B.2** and **B.3**). By lowering the oxygen fugacity, the total Mg/total C ratio decreases because of the differences in the Mg-silicate-bicarbonate and Ca-formate aqueous complexes. This means a proportional higher availability of Ca-formate complexes, leading to the formation of Ca-rich silicates, which cross deeper into the eclogitic field.

3.5.3 Implications for diamond-inclusion petrogenesis

Carbon speciation controls silicate composition and it is also linked to the diamond formation. However, diamond is not formed in the carbon-undersaturated models in this study (**Table B.4**). In our models, Mg-poor garnets and clinopyroxenes form from low-carbon fluid metasomatism. Therefore, these data imply that Mg-poor eclogitic diamond inclusion did not form during the metasomatic event which formed their host diamond. These inclusions are therefore likely protogenetic. Thus, their geochemistry should strongly reflect an eclogite protolith or, alternatively, a metasomatic event prior to the formation of the host diamond.

Conversely, our data also show that carbon-rich fluid metasomatism results in the formation of Mg-rich garnets and clinopyroxenes. This result implies that peridotitic and websteritic garnets and clinopyroxenes can be either syngenetic or protogenetic.

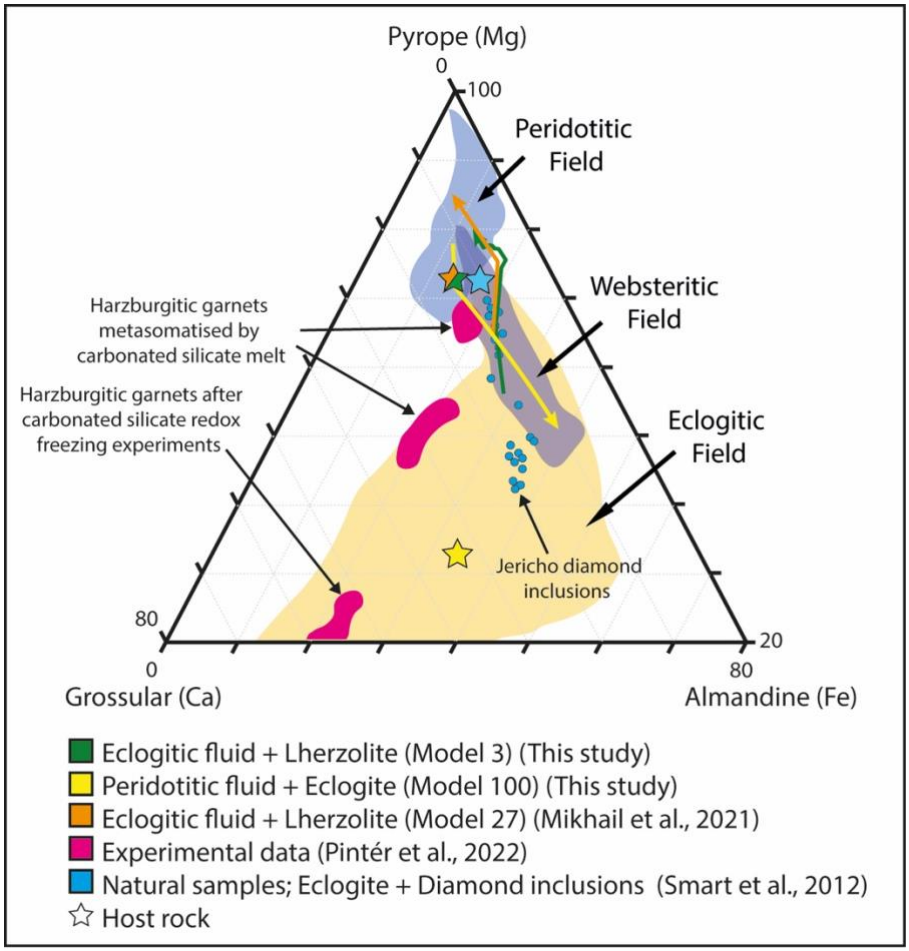

Figure 3.5 - Garnet evolution during melt/fluid metasomatism observed in a) natural samples (blue points; Smart et al., 2012), b) experimental samples (red fields; Pintér et al., 2022), and c) modelling (orange and green arrows; Mikhail et al. (2021) and this study).

Testing our models is challenging due to a dearth of data from natural samples and/or high-pressure experiments. Therefore, we compare our model trajectories with the scarce data available. These are [1] a unique sample extracted from the Jericho kimberlite (NW Slave

Craton, Canada; Kopylova and Hayman, 2008) and [2] a recent set of experiments designed to simulate hydrous melt metasomatism in the SCLM (Pintér et al., 2022). Firstly, as with most kimberlites, Jericho provides a suite of mantle xenoliths spanning a wide range of lithologies (eclogite, coarse and deformed peridotite, megacrystalline websterite and ilmenite–garnet wehrlite; Kopylova et al., 1999). Among these, there is a sample of diamondiferous eclogite which has generated a unique dataset: the geochemistry of garnets from diamond inclusions and the geochemistry of garnets from a certified host rock (Smart et al., 2012). These data indicate that diamond-hosted garnets in a single xenolith can show major element heterogeneity between individual diamonds in the same source rock and be all distinct from their host eclogite (**Fig. 3.5**). Secondly, Pintér et al. (2022) simulated the interaction between hydrous carbonated silicate melts and harzburgite, and the resulting geochemistry of their metasomatic garnet (**Fig. 3.5**). These comparisons show that our model trajectories are coherent with natural data from Jericho diamond inclusions, where the interaction between a high-MgO eclogite and a carbonated melt/fluid is responsible for a broad range of websteritic and eclogitic garnets (Smart et al., 2012).

The experimental garnet is more grossular-rich than our model garnet, but they do show the same directional compositional trend, with an evolution towards more Mg-rich endmembers during metasomatism (**Fig. 3.5**). Therefore, these comparative datasets prove that a single metasomatic event is capable of forming silicates with different chemical compositions, and these minerals mostly reflect the elemental composition of the fluid/melt instead of the geochemistry of the host rock. Therefore, the paragenetic groups used to classify diamonds (Stachel and Harris, 2008) should not be considered a genetic classification, as the role of the fluid/melt appears to be more relevant than the one played by the host rock.

3.6 CONCLUSIONS

We modelled the interaction between three fluid compositions found in fluid inclusions in diamonds (peridotitic, eclogitic and carbonatitic) with a broad range of mantle rocks (peridotites, eclogites and pyroxenites) at conditions relevant to the diamond formation (1000ºC, 5 GPa, logfO_2 = -2 to -4 ΔFMQ) to simulate fluid-rock metasomatism. We specifically focused on a wide range of initial carbon concentrations in the metasomatic fluids to explore the effects on the chemical evolution of garnet and clinopyroxene during metasomatic processes. We studied how different fluids, rocks, amounts of carbon, and environmental conditions can influence the major element compositions of silicate inclusions in diamonds.

Our results show that the driving force for silicate evolution is the chemical gradient established between the host rock and the fluid, leading to the possibility of connecting different paragenetic groups along a single reaction pathway in an isobaric and isothermal system. Both fluids and host rocks play an important role in controlling the silicate chemical evolution: the fluid is responsible for the initial composition of metasomatic minerals, and later, when the magnitude of fluid-rock interaction increases, the host rock becomes dominant. These data highlight how paragenetic groups of inclusions from diamonds are not necessarily directly related to a particular geological environment in every case. Instead, the traditional paragenetic groups can reflect the extent of the metasomatic process and the nature of the original metasomatic fluid.

Importantly, the amount of carbon in the initial fluid strongly influences the compositions of the silicate minerals formed during metasomatism. Carbon-poor fluids are necessary to form Mg-poor, Ca-rich garnets and clinopyroxenes from the chosen starting bulk composition, but do not form diamond under the conditions we examined. This result suggests that a syngenetic origin of diamonds and low-Mg eclogitic inclusions may not be feasible during the same metasomatic event. Such inclusions in diamonds may well be protogenetic. Instead, carbon-

rich fluids can precipitate Mg-rich minerals and diamond. Therefore, peridotitic and websteritic inclusions in diamonds can be either syngenetic or protogenetic, and no single notion can be championed beyond a reasonable doubt without direct evidence from the sample(s) in question. We suggest that focus should be directed towards diamonds containing multiple inclusions of the same mineral group (especially garnet and clinopyroxene), where each inclusion is examined for its crystallographic orientation, major and trace element geochemistry, and relative geochronology.

CHAPTER 4

FLUID-ROCK METASOMATISM AS A SOURCE OF MANTLE PYROXENITES

4.1 ABSTRACT

Pyroxenites represent a significant lithology in the Earth's mantle. Their origin is commonly linked with melt-metasomatism, where different grades of magma hydration have been invoked to explain the specific geochemical, mineralogical, and textural characteristics. Here use the Deep Earth Water model simulations under mantle conditions (5 GPa, 1000 ºC, and logfO_2 = ΔFMQ -2 to -4) to assess the likelihood that pyroxenites might be related to fluid-metasomatism. We react eclogitic, peridotitic, and carbonatitic fluids with a range of mantle lithologies (eclogites, peridotites, and websterites) and find that the resulting rock is richer in pyroxene than the initial rock. Most of our models result in the formation of a metasomatic pyroxenite, alongside fertile peridotites (wehrlite) and eclogite when the formation of metasomatic olivine or coesite is triggered. Therefore, our data show that fluid-metasomatism can re-fertilize refractory peridotites and eclogites.

4.2 INTRODUCTION

4.2.1 Occurrence and role of pyroxenites in the Earth's mantle

Pyroxenites are mostly metasomatic rocks, where melt-rock and fluid-rock interactions are held responsible for their genesis. However, the origin and geochemistry of the melts and fluids remain enigmatic. Pyroxenites are defined as ultramafic rocks with >90% pyroxenes by volume. Typical minor phases include olivine, garnet, spinel, and hydrous phases such as

amphiboles, micas, and talc. Pyroxenites are observed in association with peridotites in several geological settings, including ophiolites (Kaczmarek et al., 2015; O'Driscoll et al., 2015), orogenic peridotites (Melcher and Meisel, 2004; Malaspina et al., 2006) and volcanic xenoliths (Wang et al., 2008; Bénard and Ionov, 2013), with a wide variety of textural and structural characteristics.

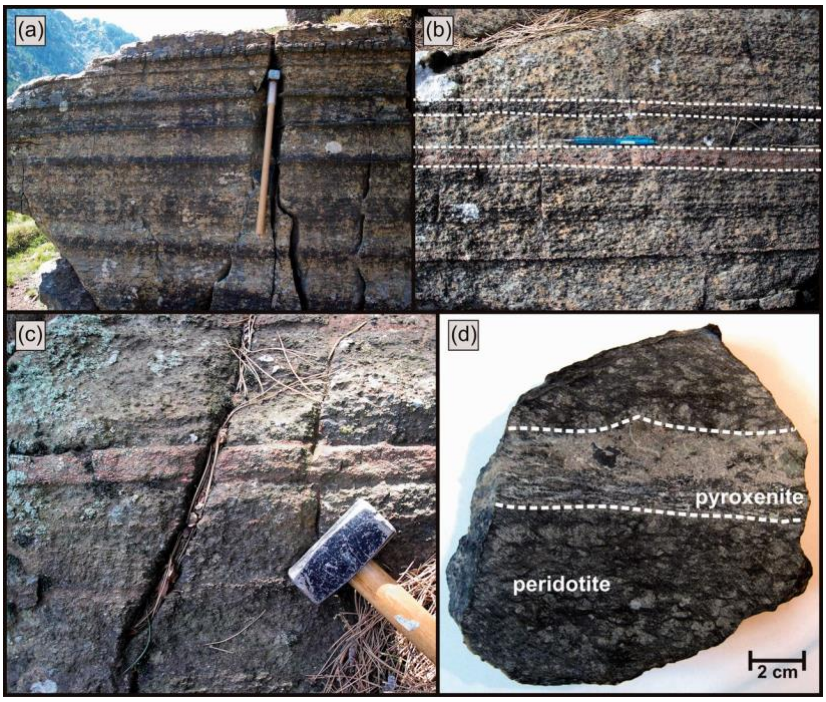

Figure 4.1 – Centimetres-thick layers of pyroxenite embedded in mantle peridotites from Monte Castellaro (a) and Suvero ultramafic bodies (b, c) (External Liguride Units, Northern Apennines, Italy). The layers are parallel to the tectonic foliation. d) is a representative hand sample showing orthopyroxene rims at the boundary with the host peridotite. Figure from Borghini et al. (2016).

Pyroxenites are often found as veins or layers (**Fig. 4.1**) within peridotite massifs and peridotite xenoliths from the mantle with sharp boundaries separating the thin pyroxenite component(s) from their host peridotite (Halama et al., 2009; Bénard and Ionov, 2013). Reaction textures,

such as reabsorbed olivine associated with hydrous minerals such as phlogopite and amphiboles, are common (e.g., Wang et al., 2016; Basch et al., 2019; Pellegrino et al., 2020). Globally, the spatial distribution of mantle pyroxenites is unknowable, but their abundance in the terrestrial mantle has been estimated to be about 10% (Bodinier and Godard, 2014). The physical properties of pyroxenites define their importance to mass transfer in the mantle because a rock with >90% pyroxene has a much lower melting temperature than a peridotite (Yoder and Tilley, 1962). Major element, trace element, and stable isotope data have been used to suggest that pyroxenites are major sources for arc, mid-ocean ridge, and ocean island melts (Sobolev et al., 2007; Soderman et al., 2023; Vlastélic et al., 2023; Bowman and Ducea, 2023). Pyroxenites are also considered critical in mechanical coupling (Moore and Lockner, 2010; Hirauchi et al., 2013) and the mobilisation of incompatible trace elements (Malaspina et al., 2009; Marschall and Schumacher, 2012) in the mantle wedge above the subducting slab. Therefore, establishing the possible range of the petrogenesis of mantle pyroxenites is necessary to accurately explain the origin of melt source(s).

Despite their importance to all major primary basalt sources and their potential to influence mass transfer throughout the otherwise solid Earth (Sverjensky et al., 2014b), the genesis of pyroxenites remains debated. Many different scenarios can be considered for their formation: [1] silicate melt metasomatism of peridotites (Laukert et al., 2014; Endo et al., 2014; Borghini et al., 2016; Sklyarov et al., 2021); [2] dehydration of silica-enriched serpentinite (Scambelluri et al., 2001; Padrón-Navarta et al., 2011); [3] partial melting of recycled crustal lithologies (Pearson et al., 1993; Hofmann, 2007; Varas-Reus et al., 2018); [4] stalled segregated melts via partial melting of the asthenosphere (Warren et al., 2009; Gysi et al., 2011), and [5] aqueous fluid-rock metasomatism of (McInnes et al., 2001; Grant et al., 2016; Mikhail et al., 2021). Additionally, the role of hydrous melts (the grey zone between fluid and melt metasomatism)

has been invoked to explain the textural and mineralogical characteristics that define different peridotite-pyroxenite complexes (Timina et al., 2015; Azevedo-Vannson et al., 2021).

In this contribution, we do not attempt to explain the petrogenesis of any specific peridotite-pyroxenite complex, nor do we try to solve for the origin of all pyroxenites. Instead, we present a thermodynamic modelling approach to evaluate the potential for fluid metasomatism as one possible origin of mantle pyroxenites. We use the Extended Deep Earth Water model (Huang and Sverjensky, 2019) to simulate fluid-rock interaction at isobaric (5 GPa) and isothermal (1000 ºC) conditions and provide a new petrogenic model for pyroxenite formation driven solely by (melt-free) fluid-rock metasomatism.

4.2.2 Fluid as a metasomatic agent

A silicate melt comprises a liquid with a three-dimensional polymerised network of Si or Si-Al tetrahedrons, but there is no empirical definition of a metasomatic fluid. The only direct samples of aqueous agents from Earth's sub-lithospheric mantle are found in diamond inclusions, the geochemistry of which has generated the term High-Density fluids (HDFs) (Weiss et al., 2022). The term fluid is widely used in mantle petrology, where the postulated middle ground between fluid and melt is called a hydrous melt. However, there is a continuous solubility curve between SiO_2 (melt) and H_2O (fluid) in the SiO_2-H_2O system (Newton and Manning, 2008), so the position of hydrous melts is difficult to define. The term fluid is used to define a solvent which acts as a mobilising agent where the framework is not polymerised but is thought to be dominated by H_2O above the second critical endpoint (the termination of the solidus in a P–T space; Wyllie and Ryabchikov, 2000; Kessel et al., 2005b).

Distinctions between fluid and melt metasomatisms are made using incompatible trace element systematics underpinned by indirect experimental solubility data (Griffin and Ryan, 1995; Halama et al., 2009; Bénard and Ionov, 2013). However, whether the mobilising agent is a melt

or aqueous fluid, it can dissolve and transport all the rock-forming components. Therefore, melts and fluids as metasomatic agents can precipitate similar mineral phases depending on their geochemistry (e.g., silicate minerals; Huang and Sverjensky, 2019; Mikhail et al., 2021). In fact, aqueous fluids at upper mantle pressures can contain more than 45 wt.% solutes of the rock-forming elements in the form of aqueous ions, complexes, and neutral species ,(Huang and Sverjensky, 2019; Mikhail et al., 2021; **Fig. 4.2**). In this contribution, we do not attempt to define the physical properties of a metasomatic fluid. Herein, a fluid is described as a metasomatic agent produced by equilibrating water with a mantle rock.

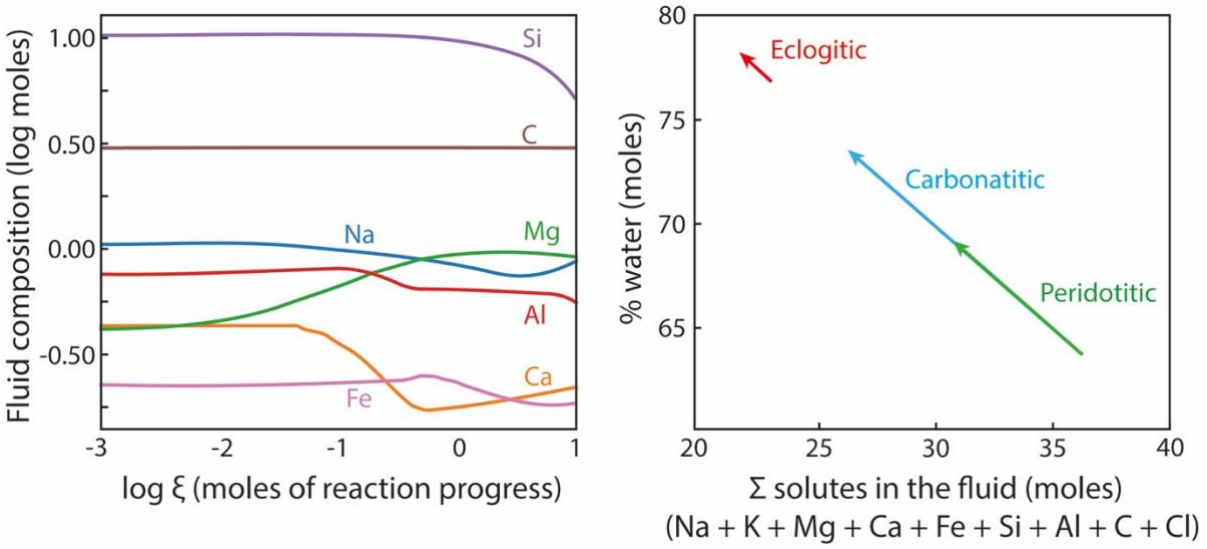

Figure 4.2 - Example model results. a) Composition of eclogitic fluids reacting with a peridotite; b) Total amount of solutes in eclogitic, peridotitic, and carbonatitic fluids reacting with an eclogite. The water content increases as the metasomatic reaction progress due to the precipitation of metasomatic minerals. 5 GPa, 1000 ºC, and logfO_2 = -3 ΔFMQ.

4.3 METHODS

4.3.1 Modelling approach

Our modelling approach involves a carbon-rich fluid interacting with a mantle rock at isobaric and isothermal conditions. The fluid is not in equilibrium with the reactant rock, and a chemical gradient is thus established. This chemical gradient drives the metasomatic reactions through irreversible chemical mass transfer, and the chemical composition of fluid and rock change, forming metasomatic minerals that evolve throughout the process. We used the aqueous speciation and solubility code EQ3 and the chemical mass transfer code EQ6 (Wolery, 1992) modified for upper mantle temperatures and calibrated with experimental solubilities (Huang and Sverjensky, 2019). The code applies the Helgeson-Kirkham-Flowers (HFK) equations of state for aqueous (Helgeson and Kirkham, 1974a, b, 1976; Helgeson et al., 1981; Tanger and Helgeson, 1988; Shock and Helgeson, 1988; Sverjensky et al., 1997) valid up to 6 GPa and 1200 ºC (Pan et al., 2013; Sverjensky et al., 2014a; Facq et al., 2014).

4.3.2 Model parameterisation

The input variables are the fluid geochemistry and the reactant rock mineralogy. Environmental parameters are fixed (P = 5 GPa; T = 1000 ºC; logfO_2 = -2 to -4 ΔFMQ). The initial fluid compositions are based on the three endmembers observed in diamond fluid inclusions (i.e., eclogitic, peridotitic and carbonatitic; Weiss et al. 2022). The eclogitic fluid has been calibrated from the fluid-eclogite equilibrium reported by Kessel et al. (2015). The peridotitic and carbonatitic fluids have been modelled on the fluid endmembers from the Panda formation and respectively set in equilibrium with a peridotite and carbonated dunite (Huang and Sverjensky, 2020). An ideal site-mixing of garnet (pyrope, grossular and almandine) and dolomite (calcite, magnesite and siderite) endmembers and a non-ideal site-mixing of clinopyroxene endmembers (diopside, clinoenstatite, hedenbergite and jadeite) have been assumed.

Fluid	ΔFMQ	C	K	Na	Ca	Mg	Fe	Al	Si	Cl	pH
Eclogitic	-3	3.13	0	1.05	0.84	0.42	0.22	1.37	10.91	0	4.6
Perioditic	-3	5.58	1.91	2	1.03	2.48	1.36	0.14	4.25	8	4.73
Carbonatitic	-3	17.96	0.5	0.5	11.13	3.01	0.68	0.72	0.08	1	5.8

Table 4.1 – Composition (molality concentration [moles/kg H_2O]) of eclogitic, peridotitic, and carbonatitic fluids (1000 ºC, 5 GPa, logfO_2 = -3 ΔFMQ). Carbon in equilibrium with diamond.

Rock	Mineral composition (% in volume)
Lherzolite	51% ol ($Fo_{0.933}Fa_{0.067}$), 18% opx ($En_{0.938}Fe_{0.062}$), 26% cpx ($Di_{0.294}Hdn_{0.088}Ja_{0.015}En_{0.603}$), 5% grt ($Py_{0.733}Gr_{0.137}Alm_{0.130}$)
Harzburgite	71% ol ($Fo_{0.933}$ $Fa_{0.067}$), 24% opx ($En_{0.938}Fe_{0.062}$), 5% grt ($Py_{0.733}Gr_{0.137}Alm_{0.130}$)
Dunite	83% ol ($Fo_{0.933}$ $Fa_{0.067}$), 5% opx ($En_{0.938}Fe_{0.062}$), 7% cpx ($Di_{0.294}Hdn_{0.088}Ja_{0.015}En_{0.603}$), 5% grt ($Py_{0.733}Gr_{0.137}Alm_{0.130}$)
Eclogite type 1	41% cpx ($Di_{0.200}Hdn_{0.100}Ja_{0.700}En_{0.000}$), 26% grt ($Py_{0.600}Gr_{0.100}Alm_{0.300}$), 33% coe
Eclogite type 2	19% cpx ($Di_{0.200}Hdn_{0.100}Ja_{0.700}En_{0.000}$), 39% grt ($Py_{0.333}Gr_{0.334}Alm_{0.333}$), 42% coe
Eclogite type 3	25% cpx ($Di_{0.200}Hdn_{0.100}Ja_{0.700}En_{0.000}$), 75% grt ($Py_{0.200}Gr_{0.600}Alm_{0.200}$)
Websterite	5% ol ($Fo_{0.920}$ $Fa_{0.080}$), 40% opx ($En_{0.750}Fe_{0.250}$), 50% cpx ($Di_{0.560}Hdn_{0.020}Ja_{0.020}En_{0.400}$), 5% grt ($Py_{0.500}Gr_{0.250}Alm_{0.250}$)
Orthopyroxenite	3% ol ($Fo_{0.890}$ $Fa_{0.110}$), 92% opx ($En_{0.900}Fe_{0.100}$), 5% grt ($Py_{0.700}Gr_{0.100}Alm_{0.200}$)
Clinopyroxenite	5% ol ($Fo_{0.930}$ $Fa_{0.070}$), 90% cpx ($Di_{0.700}Hdn_{0.025}Ja_{0.250}En_{0.025}$), 5% grt ($Py_{0.250}Gr_{0.500}Alm_{0.250}$)

Table 4.2 – Starting mineralogical and solid solution compositions of mantle rocks used during fluid-rock interaction. This table is reproduced from Chapter 3 (Paragraph 3.3.2).

The clinopyroxene solid solutions were calibrated using natural samples of diamond inclusions as described previously (Huang and Sverjensky, 2020; Mikhail et al., 2021). Carbon is set in equilibrium with diamond to avoid arbitrary constraints which may impact the results (Tiraboschi et al., 2018). These high-carbon fluids can be genetically related to sediments carried downwards by the slab in a subduction zone (Poli, 2015; Tumiati et al., 2017; Yaxley et al., 2021) (**Table 4.1, Table C.1, Table C.2**). The mineralogical composition and geochemistry of the reactant rocks have been constrained through natural data: peridotites (Pearson et al., 2014), eclogites (Pearson et al., 2014) and pyroxenites (Gonzaga et al., 2010; Farré-de-Pablo et al., 2020; Liu et al., 2022; Lu et al., 2022) (**Table 4.2**).

4.4 RESULTS

Our work focuses on the modal variation of silicate minerals along the modelled fluid-rock interactions. Full results are given in Appendix C.

4.4.1 Reaction products for fluid-rock interaction

The minerals formed during the metasomatic reaction are silicates (olivine, pyroxenes, garnet, coesite and meionite), oxides (magnetite and hematite), carbonates (dolomite, aragonite), hydroxides (brucite), and native phases (diamond) (**Table 4.3** and **Table C.3**). Fluid composition changes progressively throughout the reaction (**Fig. 4.2a**), congruent with changes to the host rock composition via dissolution and precipitation. (**Fig. 4.3**). The host rock is therefore progressively replaced by metasomatic minerals.

Run	Fluid	Initial Rock	Initial Mineralogy (vol %)	ΔlogfO_2	Final Mineralogy (vol %)	Final rock
91	Ecl	Lhz	Cpx (26.4), Grt (4.6), Opx (18.5), Ol (50.5)	-0.1	Cpx (16.8), Grt (6.5), Opx (75.2), Magnetite (1.4), Olivine (0.1)	Web
92	Per	Lhz	Cpx (26.4), Grt (4.6), Opx (18.5), Ol (50.5)	0.1	Cpx (34.0), Grt (10.5), Opx (55.2), Magnetite (0.3)	Web
97	Ecl	Ecl T1	Cpx (41.6), Grt (25.7), Coe (32.7)	0.0	Meionite (50.8), Cpx (35.2), Grt (0.7), Coe (13.3)	Ecl
98	Per	Ecl T1	Cpx (41.6), Grt (25.7), Coe (32.7)	0.2	Cpx (55.1), Grt (30.2), Mei (14.0), Coe (0.3), Diamond (0.5)	Ecl
103	Ecl	Web	Cpx (50.4), Grt (4.6), Opx (40.5), Ol (4.5)	-0.1	Cpx (57.0), Grt (13.3), Opx (29.7)	Web
104	Per	Web	Cpx (50.4), Grt (4.6), Opx (40.5), Ol (4.5)	0.1	Cpx (58.3), Grt (15.2), Opx (25.1), Magnetite (1.4)	Web
146	Carb	Lhz	Cpx (26.4), Grt (4.6), Opx (18.5), Ol (50.5)	0.3	Cpx (49.2), Mag (2.1), Mei (7.1), Ol (40.2), Diamond (1.5)	Wehr
152	Carb	Ecl T1	Cpx (41.6), Grt (25.7), Coe (32.7)	0.5	Cpx (58.1), Magnetite (2.3), Mei (37.7), Diamond (1.9)	Clinopx
158	Carb	Web	Cpx (50.4), Grt (4.6), Opx (40.5), Ol (4.5)	0.5	Cpx (71.8), Grt (5.3), Magnetite (4.5), Olivine (16.9), Diamond (1.6)	Wehr

Table 4.3 - Final mineralogy after fluid-rock interaction for selected models. Temperature and pressure are fixed respectively at 1000 ºC and 5 GPa. The oxygen fugacity is initially fixed at logfO_2 = -3 ΔFMQ, but small variations occur during the metasomatic interaction.

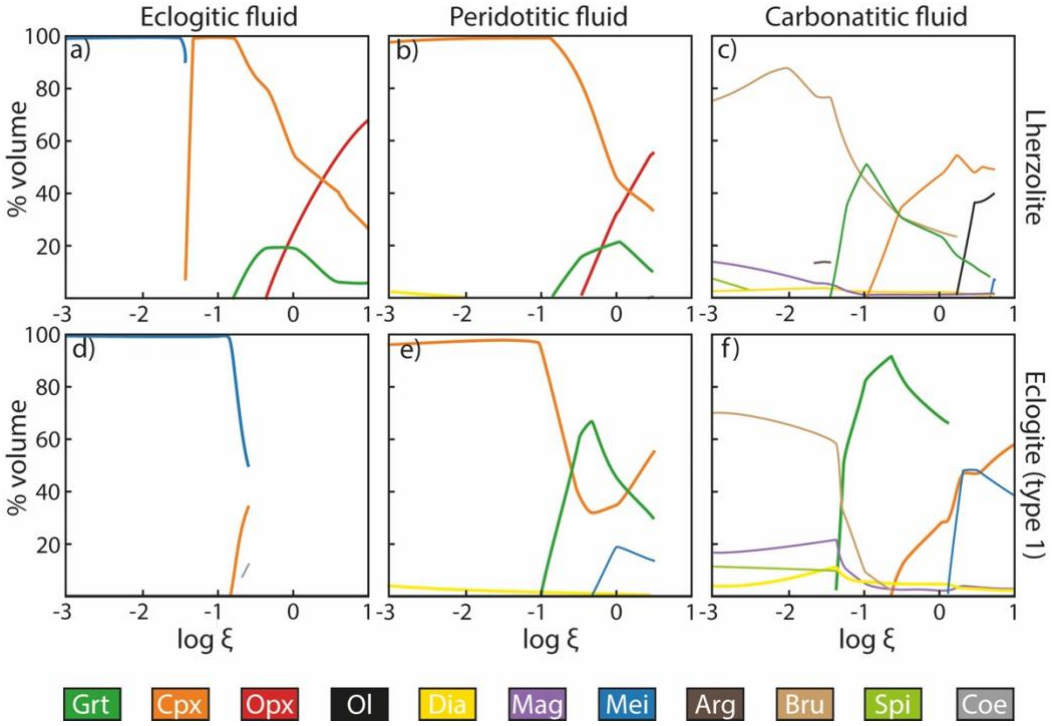

Figure 4.3 – Example of geochemical evolution of metasomatic minerals during the interaction between eclogitic, peridotitic, and carbonatitic fluids with lherzolite and eclogite (5 GPa, 1000 ºC, and logfO_2 = -3 ΔFMQ). The continuous variation in the fluid geochemistry changes the relative amounts of metasomatic minerals in the system. The progressively higher availability of aqueous silica stabilises silicates at the expense of non-silicate minerals. The reaction progress variable (ξ) corresponds to the destruction of 1.0 mole of each reactant mineral. [Mei: Meionite, Cpx: Clinopyroxene, Grt: Garnet, Opx: Orthopyroxene, Mag: Magnetite, Ol: Olivine, Dia: Diamond].

In the first stages, the fluid is the dominant component of the system. Increasing the magnitude of the metasomatic reaction, the host rock becomes progressively more influential and contributes to the availability of elements in the fluid. These variations in the geochemistry of the fluid due to a higher amount of host rock dissolved trigger dissolution and precipitation reactions, changing the relative proportions between minerals in the system. The presence and

abundance of oxides, hydroxides, carbonates, and native phases are related to the redox conditions of the system, which deeply influence the availability of aqueous silica in the system. The solubility of aqueous silica diminishes when lowering the oxygen fugacity, preventing the precipitation of silicates in favour of non-silicate minerals (**Fig. C.1**). As the magnitude of fluid-rock interaction increases, aqueous silica becomes more abundant in all the models, regardless the initial oxygen fugacity of the system, and the precipitation of silicates is thus favoured. The mineral transitions shown in **Fig. 4.3** are related to the instability of the metasomatic minerals when increasing the content of aqueous silica in the fluid, and they are mostly unrelated to variations in the redox conditions of the system. Still, in isolated cases, these transitions mark a small variation in the oxygen fugacity of the system (< 0.1 $\Delta \log fO_2$), especially when redox–sensitive minerals such as magnetite and diamond are involved. A noticeable exception is meionite ($Ca_4Al_6Si_6O_{24}CO_3$), a silicate connected to the high chemical activities of calcium and carbon in the early stages of the fluid-rock interaction when carbonates and other Ca-rich silicates are still unstable. Usually, meionite is later replaced by clinopyroxene (**Fig. 4.3a**), carbon-rich aqueous species, and occasionally diamond. When eclogitic fluid reacts with eclogites, meionite is preserved throughout the metasomatic process (**Fig. 4.3d**). Diamond is remarkably stable when the metasomatic process involves carbonatitic fluids (**Fig. 4.3c** and **4.3f**; **Table C.3**).

4.4.2 Evolution of metasomatic minerals during a fluid-rock interaction

Silicates are the principal solid phases formed in our models in later stages (**Table 4.3** and **Fig. 4.3**). Their chemical composition and abundance progressively change until the thermodynamic equilibrium of the system is attained, with the chemical and mineralogical evolution of the metasomatic rock showing a progressive increase of Mg-content of the ferromagnesian minerals.

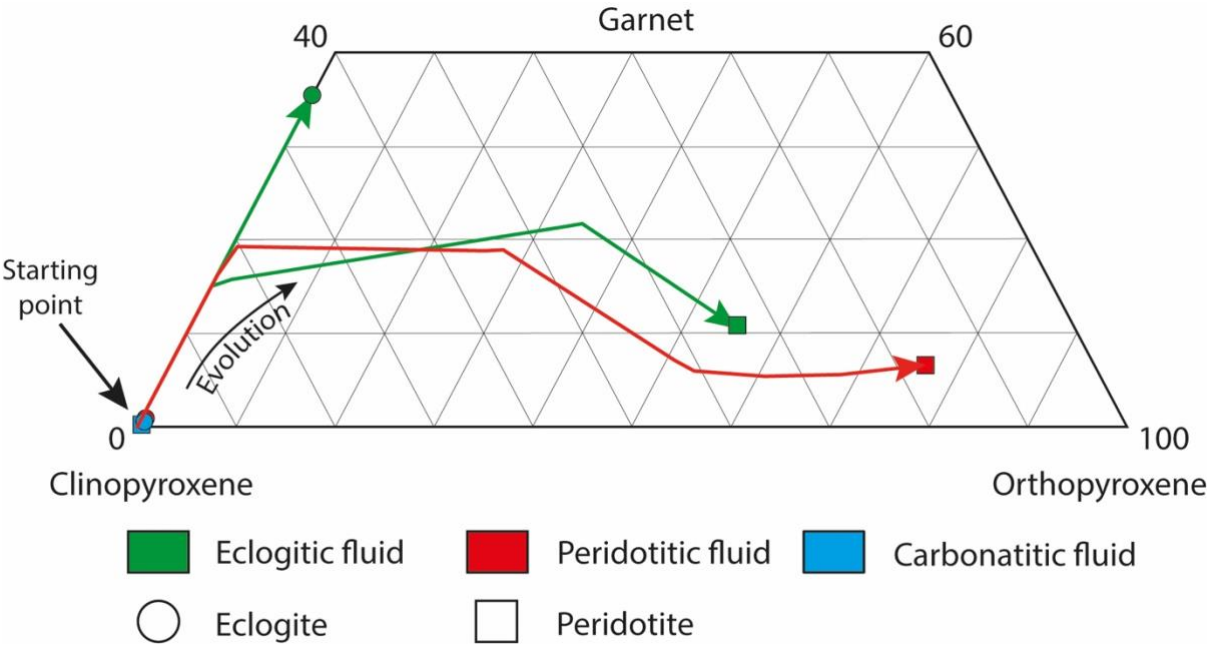

Figure 4.4 - Selected model results for the evolution of the metasomatic interaction (5 GPa, 1000 ºC, and logfO_2 = -3 ΔFMQ). The progression of the metasomatism stabilises Mg-rich minerals, increasing the relative amount of orthopyroxene and garnet along different pathways related to the bulk composition of the system. The final rocks are therefore richer in pyroxene and garnet than the initial host rocks (**Table 4.3** and **Table C.3**). The detailed parameters of each model are listed in **Table 4.1** and **Table 4.2**.

At logfO_2 = -3 ΔFMQ, peridotitic fluids and eclogitic fluids interacting with Mg-rich lithologies (peridotite, websterite, and orthopyroxenite) (**Fig. 4.3a** and **Fig. 4.3b**), result in Mg/Ca ratio high enough to trigger the formation of enstatite-rich pyroxene and pyrope-rich garnets (**Fig. 4.4)**. Therefore, these interactions lead to the formation of websterite and orthopyroxenite. Instead, Mg-rich minerals are unstable in models where peridotitic and eclogitic fluids interact with Ca-rich lithologies (eclogite and clinopyroxenite). In such cases, if the initial host rock is coesite-rich (eclogite type 1 and type 2) (**Fig. 4.3d** and **Fig. 4.3e)**, the abundance of aqueous silica triggers the formation of metasomatic coesite, and the final

metasomatic rock is an eclogite. If the initial host rock is coesite-free (eclogite type 3 and clinopyroxenite), Ca-rich pyroxene and garnet are favoured, and the final metasomatic assemblage is a clinopyroxenite (**Fig. 4.4** and **Table C.3**). Variations in oxygen fugacity influence the composition of pyroxene and the orthopyroxene/clinopyroxene ratio in models involving peridotitic and eclogitic fluids (**Fig. C.1** and **Table C.3**), alongside variations in the amount of metasomatic coesite. This redox-sensitive behaviour of the pyroxene and coesite can be attributed to variations in the availability of aqueous silica and speciation of the aqueous phase (in particular, Mg–Ca–Fe–C complexes) when the oxygen fugacity of the system changes.

For carbonatitic fluids, the high Ca content in the system prohibits the precipitation of abundant orthopyroxene, regardless of the initial oxygen fugacity of the system (**Fig. 4.3** and **Fig. C.1**). The precipitation of clinopyroxene associated with grossular-rich garnet is favoured, and the Mg in the fluid is exhausted through the formation of olivine and Mg-rich endmembers (pyrope and diopside). The metasomatic interaction with an orthopyroxene-poor host rock (eclogite, clinopyroxenite and dunite) (**Fig. 4.3f**) results in a clinopyroxenite, or eclogite, when coesite is stable. Instead, if the host rock is orthopyroxene-rich (lherzolite, websterite and orthopyroxenite) (**Fig. 4.3c**), the final rock is a wehrlite (**Fig. 4.4).**

Therefore, most of the resulting rocks span the whole range of natural pyroxenites (from clinopyroxenite to orthopyroxenite), alongside fertile peridotites (wehrlite) and eclogite when the formation of metasomatic olivine or coesite is triggered (**Fig. 4.4**, **Table 4.3, Table C.3**).

4.5 DISCUSSION

4.5.1 The metasomatic products after fluid-rock interaction

Fluid composition controls the minerals formed in the first stages of our models when the host rock is a passive bystander. The host rock progressively gains influence as fluid-rock interaction proceeds, driving the metasomatism in the final stages. Among all the minerals in the host rock, pyroxenes show the highest reactivity, directly controlling the elements released into the fluids and, therefore, the direction of the metasomatic evolution. Olivine and garnet have minor influence but do provide sources of elements. Our models show that a fluid-metasomatism can result in a two-pyroxene association (websterite), as reported by Mikhail et al. (2021), but only when the Mg content is high enough to allow the precipitation of orthopyroxene (peridotitic fluid; eclogitic and carbonatitic fluid interacting with orthopyroxene-rich rocks). Instead, when orthopyroxene is unstable due to a high Ca/Mg ratio (eclogitic and carbonatitic fluid interacting with orthopyroxene-poor rocks), the system evolves toward a clinopyroxenite, a wehrlite or an eclogite (**Fig. 4.4**, **Table 4.3, Table C.3**). Although the modelled fluids are carbon-rich and some experimental studies show carbonates to be stable at 5 GPa (Poli, 2015; Yaxley et al., 2021), the low oxygen fugacity in our models prevents the formation of abundant carbonates. Dolomite and meionite are the only carbonated phases formed, but the fluid reabsorbs them in favour of dissolved C-rich aqueous species in most cases (**Fig. 4.3**, **Table 4.3**). Meionite remains stable only at high Ca content (eclogitic fluid + eclogite), and diamond is preserved mostly when carbonatitic fluids are involved.

4.5.2 Deciphering the role of fluid vs melt metasomatism for the origin of pyroxenites

Our results are similar to recent experimental data, where pyroxenitic layers form during the interaction between hydrous melts and peridotites (Pintér et al., 2022). Thermodynamic modelling does not provide any spatial distribution of the metasomatic phases; therefore, the

fluid-rock interaction may result in a different texture when compared with the melt-rock interaction. However, fluids and melts have different physical properties under the pressure-temperature conditions of a mantle wedge. The density and rheology of fluids are lower than melts because of the absence of the silicate chains, resulting in a more flexible structure that enhances mobility. Fluids, therefore, can travel further along fractures (White et al., 2019) and grain boundaries (Watson and Lupulescu, 1993) and more easily readily traverse the mantle. Because of this, fluid-rock interaction should be more pervasive than melt-rock interaction. Interestingly, the diamond-pyroxenite association observed in our models is a close analogue to the connection previously reported during melt-rock interaction (Kiseeva et al., 2016). We do not doubt that some mantle pyroxenites are formed via melt metasomatism. However, our data show that fluid metasomatism can convert refractory peridotites and eclogites into fertile websterites. Unfortunately, distinguishing between fluid and melt metasomatism is complex. Still, this work indicates that hydrous phases (e.g., phlogopite and amphiboles) are not a reliable signature of aqueous fluid metasomatism in mantle rocks, *a priori*. The reverse is also true, where the absence of hydrous phases in natural pyroxenites should not be taken as evidence for fluid-absent metasomatism. For example, mantle diamonds are metasomatic precipitates from water-rich fluids, but hydrous phases are rarely observed as inclusions (e.g., Stachel et al., 2022). The application of trace element data seems most promising, where the enrichment of fluid-mobile elements (i.e., LILE) might be helpful to discriminators when compared with less fluid-mobile elements (i.e., REE). However, the abundance of ligand-forming anions (F^-, Cl^-) will significantly influence the fluid solubilities of the presumably less fluid mobile REE (Spera et al., 2007). Our data suggest that fluid metasomatism might form metasomatic mantle rocks (pyroxenites), which are virtually indistinguishable from those created via melt metasomatism, especially for non-pristine samples (i.e., altered rocks).

However, we also show that the fluids and melts should serve the same role in the mass transfer of rock-forming elements throughout the mantle.

4.6 CONCLUSIONS

Pyroxenites are metasomatic results of the interaction between melt and fluids with ultramafic rocks. We modelled fluid-rock metasomatism through the reaction between three fluids (eclogitic, peridotitic and carbonatitic) with a broad range of mantle rocks (peridotites, eclogites and pyroxenites) at relevant mantle conditions (1000 ºC, 5 GPa and logfO_2 = -2 to -4 ΔFMQ). We propose a mechanistic explanation for pyroxenite formation through fluid-rock interaction at isobaric and isothermal conditions. The high mobility of fluids can promote a more efficient infiltration into the host rock and result in textures compatible with the ones observed in natural pyroxenites. Fluids alone can be responsible for the sub-solidus metasomatic conversion of refractory peridotites and eclogites into fertile websterites without involving any partial melting. The composition and speciation of the fluid define the crystallisation pattern and directly influence the resulting metasomatic mineral associations. Eclogitic, peridotitic, and carbonatitic fluids have all the elements required for precipitating rock-forming silicates, and they do not necessarily precipitate hydrous phases as commonly believed. Therefore, fluid-rock interaction can produce the whole range of natural pyroxenites, and hydrous minerals are not a reliable signature for discerning melt and fluid metasomatism.

CHAPTER 5

METASOMATISM IS A SOURCE OF METHANE ON MARS

5.1 ABSTRACT

A strong greenhouse effect is required early in Martian history to permit the stability of liquid water on the surface. The abundance and antiquity of Martian volcanic centres suggest that early Mars was much more volcanically active than it is presently. On Earth, volcanic degassing regularly releases greenhouse gases such as CO_2 and H_2O into the atmosphere. For Mars, and the early Earth, the speciation of carbon released is likely to be more methane-rich because the interiors are, and were, more reducing than present-day Earth. The repeated findings of reduced carbon in association with high-temperature minerals in Martian igneous meteorites back up this assertion. Here we undertake a thermodynamic investigation simulating fluid-rock interaction and predict carbon speciation in magmatic fluids at the Martian crust-mantle boundary. We find methane is a major carbon species between 300 and 500 ºC where $\log fO_2$ is set at ΔFMQ (Fayalite – Magnetite – Quartz) equal to 0. When $\log fO_2$ is below FMQ, methane becomes the dominant species at all investigated temperatures (300 - 800 ºC). We find that ultramafic rocks produce more methane than mafic lithologies, independent of carbon content. We find that methanogenesis in the Martian crust is feasible over a wide range of conditions. The cooling of magmatic bodies is a viable source of methane on Mars in the present and, more so, in the past. Metasomatic methane must be considered a viable source of greenhouse gases in the early Martian atmosphere and cannot be ruled out as a source of methane in the atmospheres of telluric planets.

5.2 INTRODUCTION

The chemistry of a planet's atmosphere is an archive of surface and subsurface processes, including volcanism, weathering, meteoritic influx input and biological processes. However, differentiating between these possible sources for biologically significant carbonaceous compounds is not straightforward. For example, methane (CH_4) has repeatedly been observed in the Martian atmosphere, but the source of CH_4 remains enigmatic. Several hypotheses are open to examination, including [1] an extant subsurface biosphere, [2] hydrothermal activity, [3] the melting of clathrates or [4] present-day (non-eruptive) magmatism (Formisano et al., 2004; Mumma et al., 2009; Webster et al., 2013, 2018). Evidence from Martian meteorites indicates that the source domain for Martian basalts is likely to contain both solid macro-molecular and gaseous organic carbon components (e.g., CH_4) (Blamey et al., 2015). Significantly, this reduced carbon is associated with high-temperature magmatic minerals, suggesting a source directly from the Martian interior (Steele et al., 2012). Thus, a reduced carbon component present during Martian magmatism could be a primary source of observed CH_4 in the Martian atmosphere (Webster et al., 2018).

On Earth, abiotic methane in geological environments is associated with carbon-bearing aqueous fluids. The surface of Mars is a desert, but field observations show strong evidence of a subaerial hydrological system in the deep past (Baker et al., 1991). In addition, the Martian interior is not anhydrous, evidenced by the presence of hydrated magmatic minerals in Martian basalts (e.g., apatite and amphibole) (McCubbin et al., 2016). Notably, Martian basalts are relatively reduced compared with terrestrial samples ($\log fO_2$ = -1 to -3 ΔFMQ) (Herd et al., 2001, 2002; Hirschmann and Withers, 2008), which means the potential for abiotic igneous methane production is more likely on Mars than on Earth. Furthermore, petrological data show that the Martian mantle is likely heterogeneous, with H_2O concentrations ranging from 0.01 and 2.0 wt.% (Gross et al., 2013; McCubbin et al., 2016). This means a free-fluid phase should

be expected when silicate melts are generated and emplaced in the Martian crust during the cooling and oversaturation of the remnant melt phase. Herein we explore the potential for fluid-rock interaction as a source of atmospheric methane on Mars.

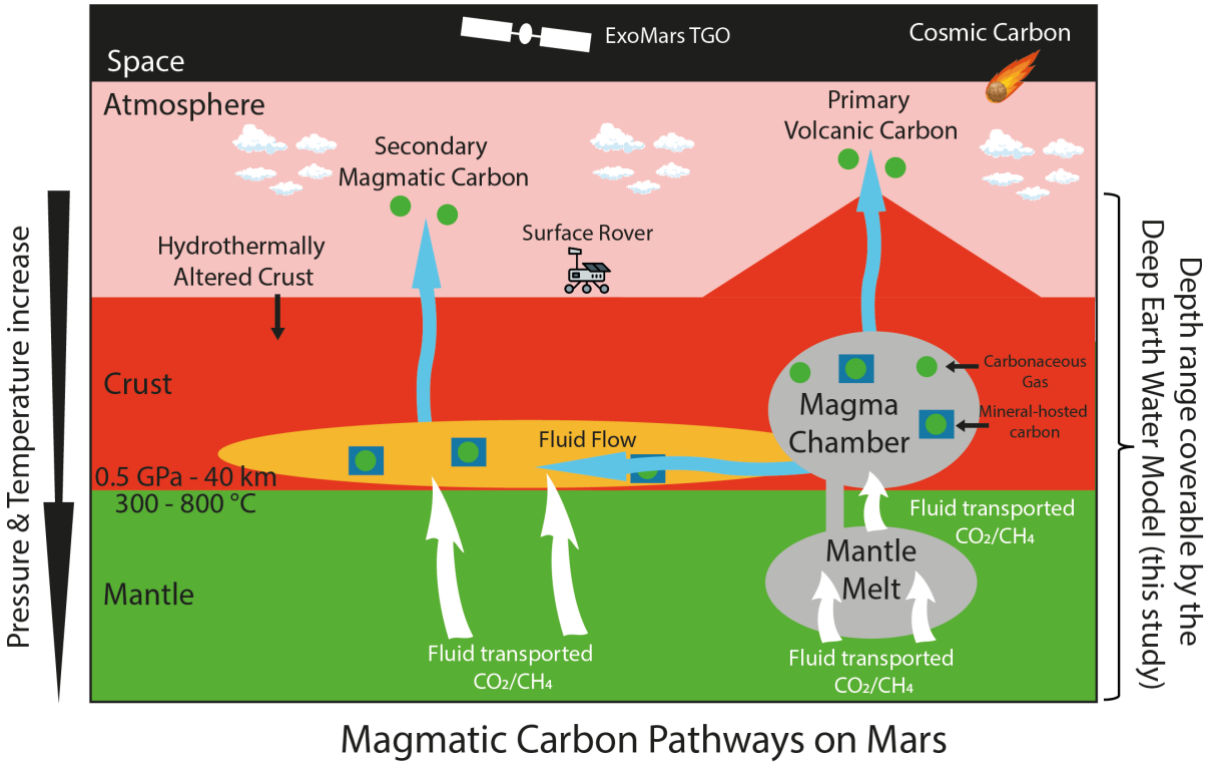

Figure 5.1 - Cartoon illustrating sources of carbon on Mars which showcases the focus of our research and our modelling approach. No spatial dimensions are considered in our model, *sensu stricto*. Instead, we control pressure, temperature, and composition and set these to correspond to the desired depth of a Martian subsurface environment.

5.3 METHODS

5.3.1 Modelling approach

We simulate fluid-rock interaction using the extended Deep Earth Water model (Huang and Sverjensky, 2019). We calculate the carbon speciation in the fluid phase as a function of the

system's composition, temperature, and oxygen fugacity. Our thermodynamic models involve two steps at isobaric and isothermal conditions. Firstly, a fluid is equilibrated with a rock. Then, secondly, during partial melting or fluid migration, the fluid interacts with a new mineral assemblage at fixed pressure and temperature conditions. During the second step, fluid and rock are not in equilibrium, with a resultant chemical driving force to promote the metasomatic interactions, during which irreversible chemical reactions produce new mineral phases while the fluid changes composition. Fluid–rock interaction is a complex and dynamic system where solid and fluid phases interact progressively, leading to an irreversible geochemical evolution. Thermodynamic modelling of fluid-rock interaction has been carried out using the Helgeson-Kirkham-Flowers (HKF) equations of state for aqueous speciation (Helgeson and Kirkham 1974a, b, 1976; Helgeson et al., 1981; Tanger and Helgeson, 1988; Shock and Helgeson, 1988; Sverjensky et al., 1997).

5.3.2 Model parameterisation

The P-T-X conditions we used (P = 0.5 GPa, T = 300-800 ºC, logfO_2 = ΔFMQ 0 to -3) are relevant to the depth where the crust-mantle boundary is considered to be located (~40 km) (Righter et al., 2008; Knapmeyer-Endrun et al., 2021). As no constraints for the geothermal gradient are available, we assumed a range of gradient between 6 ºC/km (cold planet) to 20 ºC/km (warm planet) (Heap et al., 2017; Azuma and Katayama, 2017). A range of geothermal gradients is also necessary to study how fluids evolve during cooling, such as the crystallisation of a magma ocean or the final stages of a magmatic intrusion.

The primary source of the solid macro-molecular carbon (MMC) and gaseous organic carbon components found in Martian basalts (Blamey et al., 2015) are unknown. However, the co-association with high-temperature magmatic minerals requires this source in the Martian interior (Steele et al., 2012). On Earth, fluids are mainly mobilised through magmatic and

metamorphic events related to plate tectonics. Mars may have experienced the same geodynamic environment in its history for the first part of its history (Lenardic et al., 2004; Lapen et al., 2017). Therefore, based on the assumption that Early Mars' interior is like Earth's, where peridotite is the dominant lithology, we modelled fluids initially in equilibrium with a spinel peridotite (peridotitic fluid) (Howarth et al., 2014) at different P-T-X conditions (**Table D.1**).

We used redox conditions compatible with the Martian crust and mantle ($\log fO_2$ = -3 to 0 ΔFMQ), determined by electron microprobe analysis of Fe-Ti oxides on Martian basalts (Herd et al., 2001, 2002). Despite the redox conditions suggesting graphite is stable under the environmental conditions used in this work (Hirschmann and Withers, 2008), we did not model carbon in equilibrium with graphite due to uncertainties in the activity coefficient of aqueous CO_2. Therefore, we set the amount of carbon at 0.5 molal. At 600 ºC and $\log fO_2$ = -2 ΔFMQ, we also varied the amount of carbon from 0.1 to 2.0 molal to study its influence on carbon speciation.

Rock	**Mineral composition (% in volume)**
Lherzolite	55% ol ($Fo_{0.65}Fa_{0.35}$), 35% opx ($En_{0.75}Fs_{0.25}$), 10% cpx ($Di_{0.26}Hd_{0.22}Ja_{0.01}En_{0.51}$)
Dunite	90% ol ($Fo_{0.78}$ $Fa_{0.22}$), 1% opx ($En_{0.80}Fs_{0.20}$), 4% cpx ($Di_{0.40}Hd_{0.12}Ja_{0.01}En_{0.47}$), 5% mag
Clinopyroxenite	15% ol ($Fo_{0.45}$ $Fa_{0.55}$), 80% cpx ($Di_{0.26}Hd_{0.30}Ja_{0.01}En_{0.43}$), 3% pl ($Ab_{0.59}An_{0.37}Kf_{0.04}$), 2% mag
Orthopyroxenite	95% opx ($En_{0.70}Fs_{0.30}$), 5% mag
Gabbro	2% ol ($Fo_{0.05}$ $Fa_{0.95}$), 46% cpx ($Di_{0.12}Hd_{0.43}Ja_{0.01}En_{0.44}$), 50% pl ($Ab_{0.48}An_{0.52}Kf_{0.00}$), 2% mag

Table 5.1 - Mineralogical and solid solution compositions of mantle rocks used during fluid-rock interaction. This table is reproduced from Chapter 2 (Paragraph 2.3.1)..

Natural data from Martian meteorites constrain the mineralogy and geochemistry of reactant mafic and ultramafic mantle rocks (**Table 5.1**): lherzolite (Howarth et al., 2014), dunite (Beck et al., 2006), clinopyroxenite(Treiman, 2005), orthopyroxenite (Gleason et al., 1997), and gabbro (Udry et al., 2017).

We calculate the fluid composition for a Martian peridotite in equilibrium with water at specific P-T-X (using EQ3), and then we model the fluid-rock interaction between the new metasomatic agent (high-density fluid) with different reactants (i.e., lithologies; using EQ6). We focus on the fraction of aqueous methane generated at 0.5 GPa (isobaric) between logfO_2 values of 0 and -3 ΔFMQ and cooling from 800 to 300 °C, designed to reflect the cooling of a system at the Martian crust-mantle boundary **(Fig. 5.1)**. We calculate and record carbon speciation throughout the metasomatic process and normalise the moles of each C-species to the total number of moles of carbon in the system (**Fig. 5.2**). Therefore, the percentage of fluid hosted CH_4 reported in this work relates to the fraction of CH_4 as a function of the total amount of carbon in the fluid.

5.4 RESULTS

Fluids in the crust do not behave as an isolated system as considered in simpler COH models (Frost and McCammon, 2008). Instead, fluids progressively interact with their environment. Our models chart the evolution of fluid and rock geochemistry as the system cools at the crust-mantle boundary (**Fig. 5.2**). The traditional approach to COH fluids cannot consider reactant mineralogy by design (Zhang and Duan, 2009; Dalou et al., 2019). In contrast, DEW models predict variations in the composition and speciation of fluids during their interaction with the surrounding minerals (Mikhail et al., 2021). We find that the metasomatic products after fluid-rock metasomatism are peridotites and clinopyroxenites. In addition, antigorite, biotite,

dolomite, chlorite, garnet, magnetite, paragonite, plagioclase, talc, and tremolite occasionally appear in the mineral assemblage (**Table D.2**).

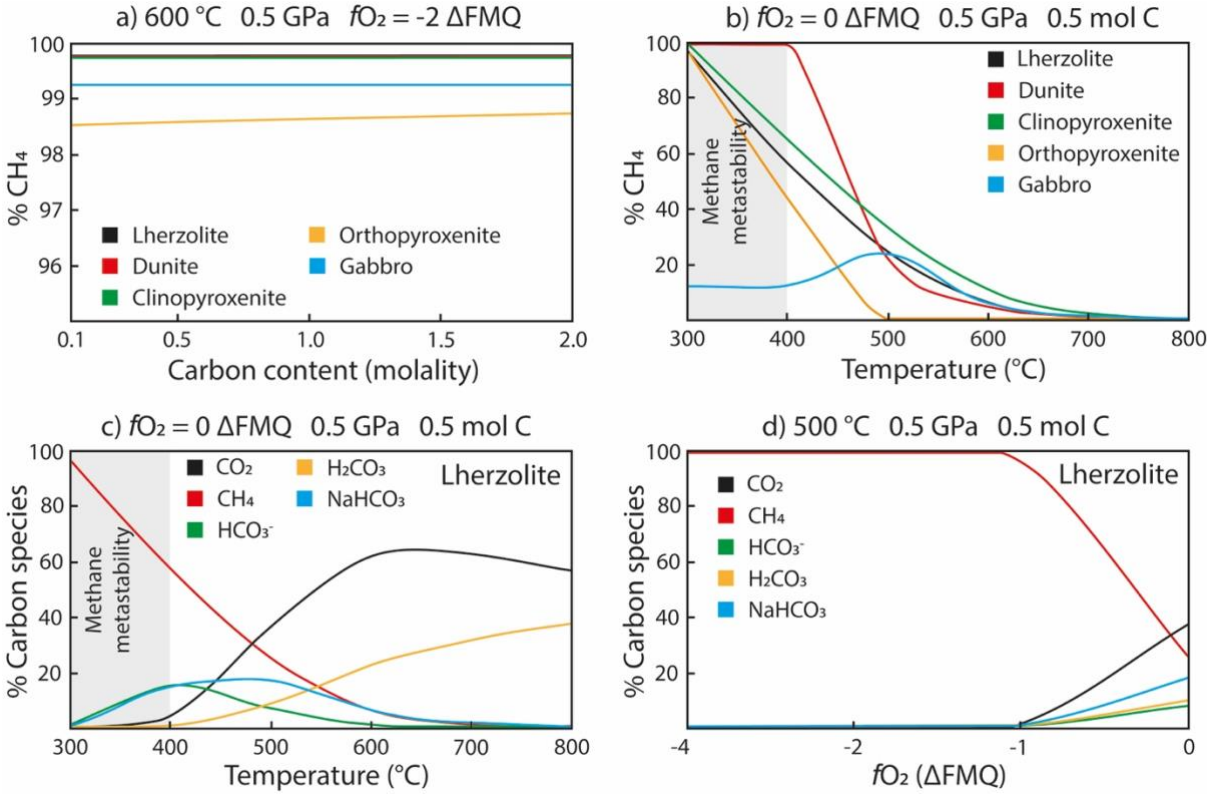

Figure 5.2 - Fraction of methane during the evolution of fluid-rock metasomatism. The main findings of this work plotted to show the fraction of methane in the fluid during metasomatism of a Range of Martian lithologies as a function of carbon content (a) and temperature (b), and the relative proportion of carbon species as a function of temperature (c) and oxygen fugacity (d). We find that the fraction of methane increases as the temperature and oxygen fugacity decrease. The total amount of carbon in the system does not affect carbon speciation. Methane metastability is reported as a grey field (Manning et al., 2013).

The most abundant carbon species in our fluids are CH_4, CO_2 and H_2CO3, followed by $NaHCO_3$ and HCO_3^- (**Table D.3, Fig. 5.2a** and **5.2b**). Other minor species (< 2%) are reported

in the database associated with this thesis. Solid carbon phases such as graphite and carbonates are rare, precipitating only when the fluid reacts with a gabbro at 300 ºC for the whole range of fO_2 in this study (a function of the concentrations of carbon and calcium in the systems) (**Table D.3**). Solid phases sequester about 75% of the total carbon in such cases. This drastically reduces the amount of carbon in the fluid and, therefore, the amount of methane by mass. At temperatures > 300 ºC, solid graphite and carbonates are unstable and dissolved into the fluid.

For systems where carbon molality is < 2.0, we find no relationship between the carbon content of the system and carbon speciation (**Fig. 5.2a**), aside from the absolute mass of all carbon species. We find that the composition of the reactant – the effective host rock lithology – plays a crucial role in carbon speciation during fluid-metasomatism (**Fig. 5.2b**). Lherzolite and clinopyroxenite produce similar carbon species; in contrast, dunite is the most suitable rock for methane production (**Fig. 5.2b**). Between 300 and 600 ºC, orthopyroxenite and gabbro produce less CH_4 than other lithologies. At T ≥ 700 ºC, all models predict about the same proportion of methane production, regardless of the reactant mineralogy and oxygen fugacity (**Fig. 5.2b**, **Fig. D.1, Fig. D.2**).

5.5 DISCUSSION

5.5.1 Influence of environmental parameters over methanogenesis

Methanogenesis is, therefore, particularly efficient when the fluid is equilibrated with ultramafic rocks, especially peridotites. Assuming that the Early Martian thermal state was similar to Earth (i.e., hotter than the present), Mars may have also experienced the emplacement of ultramafic intrusions (high-Mg rocks). If so, this would provide a perfect environment for methane production during fluid-rock metasomatism. Conversely, fluid-rock interaction with

more felsic rocks, such as gabbro, results in more oxidising conditions with the subsequent precipitation of graphitic and carbonate mineral phases, subtracting carbon from the fluid and reducing the total amount of methane.

Variations in the amount of methane between 300 and 600 ºC between lithologies reflect the stability of each mineral assemblage when reacting with the fluid at the selected P-T-X, which forces oscillations in the redox conditions of the system (**Table D.3**). Negative variations in oxygen fugacity are found when fluids react with lherzolite, dunite and clinopyroxenite, which directly impact the stability of methane. For models involving orthopyroxenite and gabbro, the ΔfO_2 is positive (i.e., increasing the oxygen fugacity of the system). This is particularly relevant at low temperatures, destabilising CH_4 in favour of more oxidised species such as CO_2, H_2CO_3, and solid phases such as graphite and calcite.

The cooling of these systems, associated with the lower oxygen fugacity of the Martian mantle and crust (Herd et al., 2002), promotes suitable conditions for methanogenesis in a magmatic environment, developing progressive CH_4-richer fluids as the temperature drops (**Fig. 5.2c**). The influence of temperature and lithology over carbon speciation is mitigated by lowering the oxygen fugacity (**Fig. 5.2d**, **Fig. D.3)**. Where $\log fO_2$ = -1 ΔFMQ, $NaHCO_3$ and HCO_3^- are no longer abundant, and instead, carbon is stabilised mainly in CH_4, H_2CO_3 and CO_2 **(Fig. 5.2c – d)**. Where $\log fO_2 \leq$ -2 ΔFMQ, methane is always the dominant carbon species. Therefore, our models show that methanogenesis is feasible over a broad range of conditions, and it is strongly affected by the mineralogy of the reactant rock, especially at relatively oxidised conditions (e.g., $\log fO_2$ = FMQ).

5.5.2 Calculation of methane content during fluid-rock metasomatism

Using the percentage of methane over the total carbon obtained in our models, it is possible to run a preliminary calculation of the amount of methane formed in the modelled systems. We

consider the amount of fluid circulating equal to 2 wt. % (Nekvasil et al., 2007; McCubbin et al., 2012; Gross et al., 2013) and a 0.5 molality of carbon. We utilise:

Equation 1 $$m_{CH_4} = V_{rock} \cdot \rho_{rock} \cdot X_{fluid} \cdot b_{carbon} \cdot M_{carbon} \cdot X_{CH_4} \cdot \frac{1}{1000}$$

Where:

m_{CH_4} = mass of methane in the fluid [g]

V_{rock} = volume of the reactant rock [m^3]

ρ_{rock} = molar mass of the rock [g/m^3]

X_{fluid} = amount of fluid interacting with the reactant rock [mol/mol]

b_{carbon} = carbon molality [mol/Kg] (1/1000 is a conversion factor from Kg to g)

M_{carbon} = molar mass of carbon [g/mol]

X_{CH_4} = fraction of methane over the total carbon of the system [%]

Lithology	**Rock density [Kg/m^3]**	**Rock molecular weight [g/mol]**	**Fluid/rock ratio [mol/mol]**	**CH_4 / C_{total} [%]**	**CH_4 (g) / 1 m^3 of reactant rock**
Lherzolite	3102	96.4	0.1	57	284
Dunite	3124	84.8	0.1	60	301
Clinopyroxenite	3297	160.4	0.2	66	349
Orthopyroxenite	3532	114.3	0.1	42	238
Gabbro	3079	208.9	0.1	3	15

Table 5.2 - Amount of methane (grams) for m^3 of rock involved in fluid-rock interaction at 400 ºC, 0.5 GPa and logfO_2 = 0 ΔFMQ.

At the conditions investigated, most of the carbon in the fluid is into methane (**Fig. 5.2**), except when the peridotitic fluid interacts with gabbro due to the precipitation of carbon-bearing solid phases such as graphite and calcite (**Table D.3)**. Rock densities are calculated from mineral compositions presented in **Table D.2**. As Martian rocks are Fe-richer than their Terrestrial counterpart, the average density of each lithology is higher.

The amount of methane for all the lithologies considered in this study at 400 ºC, 0.5 GPa and logfO_2 = 0 ΔFMQ is shown in **Table 5.2**. Below 400 ºC, the slow kinetic of reactions involving methane prevents methanogenesis and any CH_4 loss. Considering a fluid bearing 600 ppm of carbon (0.5 molal) in a system with 2.0 wt.% H_2O at 0.5 GPa, 400 ºC and logfO_2 = 0 ΔFMQ, up to 349 g of methane can be produced per 1 m^3 of rock during fluid-rock metasomatism (**Table 5.2**).

5.5.3 Transport of methane from magmatic environments to the surface

Although our models predict methane formation below 400 ºC, it is well-established that methanogenic reactions are very slow below this threshold (Manning et al., 2013). It is thus possible that aliphatic and condensed polycyclic aromatic hydrocarbons are expected instead of gaseous CH_4 (Zolotov and Shock, 1999, 2000), akin to what is observed in the meteorite record (Steele et al., 2012). Thermodynamically speaking, methane would be a metastable species at T < 400 ºC (**Fig. 5.2**). At these conditions, despite not being in equilibrium with the other carbon species, CH_4 does not react with the fluid or rocks when stored and then transported toward the surface due to its kinetic reluctance to participate in reactions (Sverjensky et al., 2020). Therefore, fluid traps located at the Martian mantle-crust boundary can store the CH_4 during the progressive cooling of a metasomatic system and preserve it over geological time, providing a shallow crustal source for methane detected in the atmosphere.

Metasomatic fluid generated in the Martian crust can reach the surface through deep fractures, which characterise the brittle Martian crust (Heap et al., 2017), resulting in effusive degassing after magma emplacement on Mars (Wetzel et al., 2013). Therefore, it is possible that metasomatic methane production was a contributor of CH_4 to the Martian atmosphere, past and present. A greater magmatic flux on early Mars – consistent with surface observations and thermal models – would have translated to a greater methane flux and thus contributed to the greenhouse effect required to explain geological evidence for an active hydrological cycle on the surface.

5.6 CONCLUSIONS

Fluid-rock metasomatism in the Martian crust can produce methane over a broad range of conditions compatible with the ones thought to be at the Martian crust – mantle boundary. This work simulated metasomatic reactions between a peridotitic fluid and a broad range of rocks (peridotites, pyroxenites, and gabbro). Where the system is warm (≥ 400 ºC) and logfO_2 is < 0 ΔFMQ, fluid-rock interaction should result in methane production both in the past and the present day. Methane can be transported to the surface by exploiting the extremely slow kinetic of reactions involving methane at low temperatures (< 400 ºC). Ergo, abiotic methane production in the crust cannot be ruled out as a source of methane in the present-day Martian atmosphere and could have contributed to the formation of the CH_4-based greenhouse required for maintaining liquid water on the surface in the past. These results are directly transferable to exoplanet science. For example, future chemical characterisation of exoplanet atmospheres via Space borne telescopes should strongly question the notion that disequilibrium carbon (i.e., the coexistence of CO_2 + CH_4) in the atmospheres of volcanically active telluric bodies might serve as a biosignature.

CHAPTER 6

CONCLUSIONS AND FURTHER WORK

6.1 FINAL REMARKS

The overall aim of this work was to model fluid-rock metasomatic interaction applied to Terrestrial and Martian mantles. I have modelled the processes and results of aqueous fluid-rock interaction using the Deep Earth Water model (Chapter 2). The results have been then analysed using *ad-hoc* python scripts, and the evolution of metasomatic minerals and fluids has been evaluated in the context of the formation of diamond inclusions (Chapter 3), the origin of mantle pyroxenites (Chapter 4), and the speciation of carbon in the Martian crust (Chapter 5).

In the simplest sense, fluid-rock metasomatism can be responsible for a range of petrological and petrographic features in mantle rocks, which often mirror the assumed result(s) of melt metasomatism. Fluid-rock interaction is an essential but often underrated mass-transfer agent for mobilising rock-forming elements in the mantle and lower crust, whose physical properties are crucial in the migration and infiltration through grain boundaries, fractures, and other discontinuities.

Fluid speciation is more complex than previously thought. For example, simple COH models (e.g., Zhang and Duan, 2009) must be revised to describe the geochemical characteristics and the mobilising power of aqueous fluid-metasomatism because they do not account for the speciation and solubility of charged complexes. The geological environment (pressure, temperature, and oxygen fugacity) controls fluid geochemistry and the composition of the resulting metasomatic minerals. These minerals are not necessarily hydrated, where anhydrous silicates such as olivine, pyroxene and garnet can be formed via fluid-rock interaction. Therefore, as the presence or absence of hydrous minerals cannot be considered a diagnostic,

the distinction between fluid and melt metasomatism needs to be examined in more detail than this PhD thesis.

The most significant results of this work are described below.

1. **Chapter 3: The importance of carbon to the formation and composition of silicates during mantle metasomatism**
    a. Diamond silicate inclusions with different compositions can result from a single metasomatic event and do not necessarily mirror or reflect the geochemistry of the host rock. The progression of a metasomatic interaction implies a change in the composition and speciation of the fluid, which is reflected in the minerals precipitated (**Fig. 3.3**, pp 58).
    b. The fluid controls the geochemistry of the metasomatic minerals in the first stages of fluid-rock interaction. Only in the final stages, the host rock exerts dominant control.
    c. The genetic classification of diamonds based on paragenetic groups (Stachel and Harris, 2008) is unsuitable for defining the host rock of a diamond and, therefore, the provenance and origin of mantle diamonds.
    d. The carbon content of a system strongly influences the composition of metasomatic silicates. Ca-rich silicates result from carbon-poor fluids, while Mg-rich silicates are linked to diamond-forming fluids (**Fig. 3.4**, pp 60). This implies that peridotitic and websteritic inclusions can be either syngenetic or protogenetic. Instead, Mg-poor eclogitic inclusions are likely protogenetic.

2. **Chapter 4: Fluid-rock metasomatism as a source of mantle pyroxenites**

    a. Fluid-rock interaction results in the precipitation of metasomatic non-hydrous minerals. Therefore, a simple petrographic analysis cannot rule out the distinction between melt and fluid metasomatism.

    b. Fluids have all the rock-forming major elements for the precipitation of silicates (orthopyroxene, clinopyroxene, olivine and garnet) with compositions comparable to minerals crystallised from silicate melts (**Table 4.3**, pp 77).

    c. Fluid-rock interaction provides a simple mechanistic model for pyroxenite formation.

    d. Fluid-rock metasomatism is a progressive reaction, and the composition of the resulting minerals varies as the process continues. Therefore, fluid metasomatism can form the whole range of natural pyroxenites (**Fig. 4.4**, pp 80).

3. **Chapter 5: Metasomatism is a source of methane on Mars**

    a. Methanogenesis is efficient at temperatures <500 °C under the reduced conditions of the Martian crust and mantle (**Fig. 5.2**, pp 91). Geological environments are thus suitable reservoirs and storage for abiotic methane on Mars.

    b. Methanogenesis is particularly efficient when a fluid reacts with ultramafic rocks. In such cases, the variations of oxygen fugacity triggered by fluid-rock metasomatism are inside the stability field of methane (**Table 5.2**, pp 94).

    c. Conversely, fluid-rock interaction with felsic rocks results in more oxidising conditions. The subsequent precipitation of graphite and carbonates subtracts carbon from the fluid and reduces the amount of methane in the fluid.

d. Methane can be preserved during the fluid migration toward the surface due to its metastability at < 400 °C. The extremely slow kinetic of chemical reactions which consume methane at low temperatures prohibit and even prevent CH_4 loss.
e. Up to 467 g of methane per host rock can be produced per 1 m^3 of rock during fluid-rock metasomatism on Mars.

6.2 LIMITATIONS OF THE PRESENT WORK

This work used the Deep Earth Water model, a thermodynamic software which predicts the result of fluid metasomatism. Nevertheless, I acknowledge that a study entirely based on thermodynamic modelling presents many uncertainties as it is inevitably bounded to the quality of the database because a model is only as good as the database.

The necessity of implementing the models with experiments and filling the gaps in minerals' thermoelastic and thermodynamic properties is a central point of my future work, which will be presented in the next section.

6.3 FURTHER WORK

This study provided many open questions, and several studies are required to test the theories discussed in this thesis. In this section, a non-exhaustive collection of future projects is described.

6.3.1 An upgrade to the Deep Earth Water model

As briefly discussed in the previous paragraph, thermodynamic modelling tools are inevitably bound to the quality of their database(s). As Chapter 2 (**Eq. 9**, pp. 33) shows, calculating the Gibbs Free energy for minerals at different conditions requires a series of thermoelastic and thermodynamic parameters. The Deep Earth Water model is based on Berman (1988), where various mineral thermodynamic and thermoelastic parameters were presented. Heat capacity and the pressure-temperature volume dependence were determined mainly by fitting the Berman equations of state to experimental data. Instead, standard mineral properties (enthalpy and entropy) were obtained by calorimetry. When published, the quality of these data and equations of state were state of the art. However, significant improvements in both analytic techniques and predictive equations of state equations have been made over the last 30 years. Presently, the most refined database of thermoelastic and thermodynamic properties of minerals is from (Holland and Powell, 2011), and most thermodynamic software like PerpleX and THERMOCALC use it as database. The Deep Earth Water model needs to be recalibrated using these more recent thermodynamic and thermoelastic data to assess the quality of DEW models using the Berman (1988) vs the Holland and Powell (2011) databases.

6.3.2 The lack of thermoelastic and thermodynamic properties of minerals

The quality of thermoelastic and thermodynamic properties is critical in thermodynamic modelling. Still, the number of phases in a database also plays a crucial role in the ability of a model to reproduce a natural system. Less than 200 minerals and endmembers have been adequately studied (Holland and Powell, 2011; Stixrude and Lithgow-Bertelloni, 2011; Murakami, 2013), which is minimal if we think that more than 5000 minerals have been discovered in nature. Characterising a larger pool of minerals would benefit every branch of Earth Sciences, as minerals are the bricks of every geological environment and influence a

system's physical and chemical properties. The heat capacity measurement has been improved through low-temperature calorimetry (Gamsjäger and Wiessner, 2018; Liu et al., 2018). Now, the standard state properties of minerals (enthalpy and entropy) can be accurately determined in a lab without expensive equipment (e.g., synchrotrons or HPHT requirements). For the thermoelastic properties (heat capacity, thermal expansion, compressibility and bulk modulus), their measurement still requires high-resolution diffraction at the synchrotron, which implies several issues in both experimental apparatus and time + energy (i.e., cost). An alternative approach is modelling the volume variations with temperature and pressure based on the crystallographic structure and how it behaves under stress (Lasaga and Gibbs, 1987; Hama and Suito, 2001; Auzende et al., 2006).

If a computational model were available, the characterisation of the thermoelastic properties of minerals would be more feasible in the short term. A statistical analysis of all the thermodynamic and thermoelastic properties of the available data could be a starting point to identify relationships between the crystallographic structure, the geochemistry, and the physical properties of minerals.

6.3.3 Chromium and other missing components

The Deep Earth Water database has an extensive collection of carbon species (Huang and Sverjensky, 2019) but requires other minor elements relevant to the diamond formation (Mikhail et al., 2014; Weiss et al., 2022). The absence of components such as Cr, N, and F reduces our ability to model how the geochemistry of the fluid influences diamond formation. To overcome this issue, thermodynamic parameters of both Cr-N-F bearing aqueous species and minerals are required.

A relevant question regards the amount of Cr_2O_3 in garnet diamond inclusions. The current diamond classification aims to identify the diamond host rock based on the geochemistry of

the garnet inclusions (Stachel and Harris, 2008). Therefore, garnet inclusions should reflect the chemical composition of garnets found in peridotites and eclogites for both major and minor elements. Nevertheless, when found as diamond inclusions, eclogitic garnets have Cr_2O_3 < 1 wt.%, while peridotitic garnets have Cr_2O_3 >1 wt.% (Aulbach et al., 2002). These values are incompatible with the traditional geochemistry of garnets, where chrome enrichment is characteristic of eclogites and not peridotites (Pearson et al., 2014). This discrepancy could be related to a metasomatic alteration of the host rock minerals operated by the fluid. It could also reinforce the idea presented in Chapter 3 that syngenetic inclusions are more common than previously thought.

To study the behaviour of chrome in fluid-rock metasomatic systems, new Cr-bearing aqueous species, Mg-chromite (Huang et al., 2019), and a garnet Cr-endmember (knorringite) have been added to the Deep Earth Water model database. I am examining this by running further models to evaluate the influence and behaviour of chrome during diamond-forming fluid metasomatism.

6.3.4 The role of the mineral assemblage during diamond formation

As discussed in Chapter 3 and Chapter 4, fluid-rock metasomatism is a dynamic system. The host rock's mineral assemblage strongly influences diamond formation in the final stages of a metasomatic process. In the models presented in this work, diamond formation is linked with $HCOO^-$ complexes, and the abundance of these compounds is directly connected with the geochemistry of the fluid. The changes in the fluid composition and speciation alter the stability of the diamond, which can be dissolved, or its precipitation can be triggered. An interesting relationship has been found when modelling the interaction between eclogitic fluid and three different peridotites (dunite, harzburgite, and lherzolite):

$$Diamond + Forsterite + MgSiC + H^{+} \rightarrow Orthopyroxene + 2\,HCOO^{-} + SiO_2 + 2\,Mg^{2+} + H_2O$$

This reaction shows as the fluid reabsorbs the diamond when the system contains olivine. An increase in the amount of olivine in the system pushes the equilibrium toward the right-hand side of the reaction. Conversely, an increase in the orthopyroxene amount shifts the balance to the left-hand side. Dunite and harzburgite would trigger the diamond dissolution due to their high amount of olivine and low amount of orthopyroxene. Instead, a lherzolite would preserve the diamond from dissolution (**Fig. 6.1**).

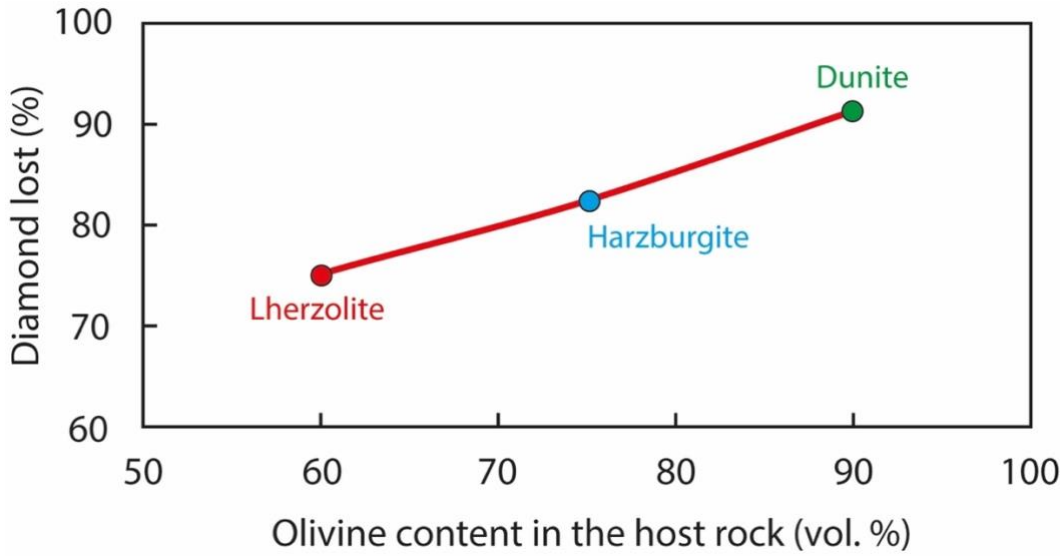

Figure 6.1 - Relationship between the olivine content of the host rock and the diamond dissolution. For diamond lost is intended how much diamond is reabsorbed by the fluid after the peak of diamond formation (i.e., the highest amount of diamond produced during the metasomatic interaction). A lower amount of olivine better preserves the diamond.

Therefore, a fertile mantle better suits the role of host rock for diamonds. Besides, this reaction would describe why orthopyroxene is rarely found as diamond inclusion, as it would react and form olivine + diamond under the right environmental conditions. This reaction may not be

common because coesite is repeatedly reported as inclusion in sub-lithospheric diamonds (Schulze et al., 2003), destabilising olivine in favour or orthopyroxene. Therefore, further experiments on diamond stability in various mineral assemblages are required to verify this relationship.

6.3.5 Experimental test for modelling data

The inaccurate or missing representation of a mineral in the database is a crucial issue that must be overcome. If improving our knowledge of thermodynamic and thermoelastic properties of minerals is central to the future of the modelling approach (Paragraphs 6.3.1 and 6.3.2), experiments are still required for corroborating the modelling results without being bound to a database. A new experimental design has been devised to study the ability of fluids to precipitate metasomatic minerals during fluid-rock interaction (**Fig. 6.2**). As multi-anvil capsules are hard to build with a multi-layer setup, the experiments have been conducted in a rotating piston-cylinder apparatus at lower pressure-temperature conditions (3 GPa and 700 °C) than the ones used in Chapter 3 and Chapter 4 (5 GPa and 1000 °C). If this setup proves to be efficient, the experimental work will be extended to higher pressures and temperatures.

The first step is to allow the water released by the dehydration of $Zr(OH)_4$ to equilibrate with the eclogite. These layers are temporarily positioned at the top of the experiment to avoid any percolation of the fluid into the peridotitic layer. For the same reason, a thick layer of synthetic diamond powder separates the eclogite and peridotite. Then, the piston-cylinder rotates, and the peridotitic layer is now at the top of the experimental setup. The fluid arises through the diamond filter and finally interacts with the top layer. As visible in **Fig. 6.2**, the metasomatic products are distributed inside the peridotite, and microprobe and Raman analysis provide their chemical composition.

Further experiments are required to improve the experimental setup and verify the models presented in this work. Potentially, exploiting the slow kinetic of sub-solidus reactions, the boundary close to the diamond filter would be exposed to the fluid for longer than the top of the capsule. Therefore, metasomatic minerals would have different compositions based on their spatial position, and an evolution pattern would be present.

x

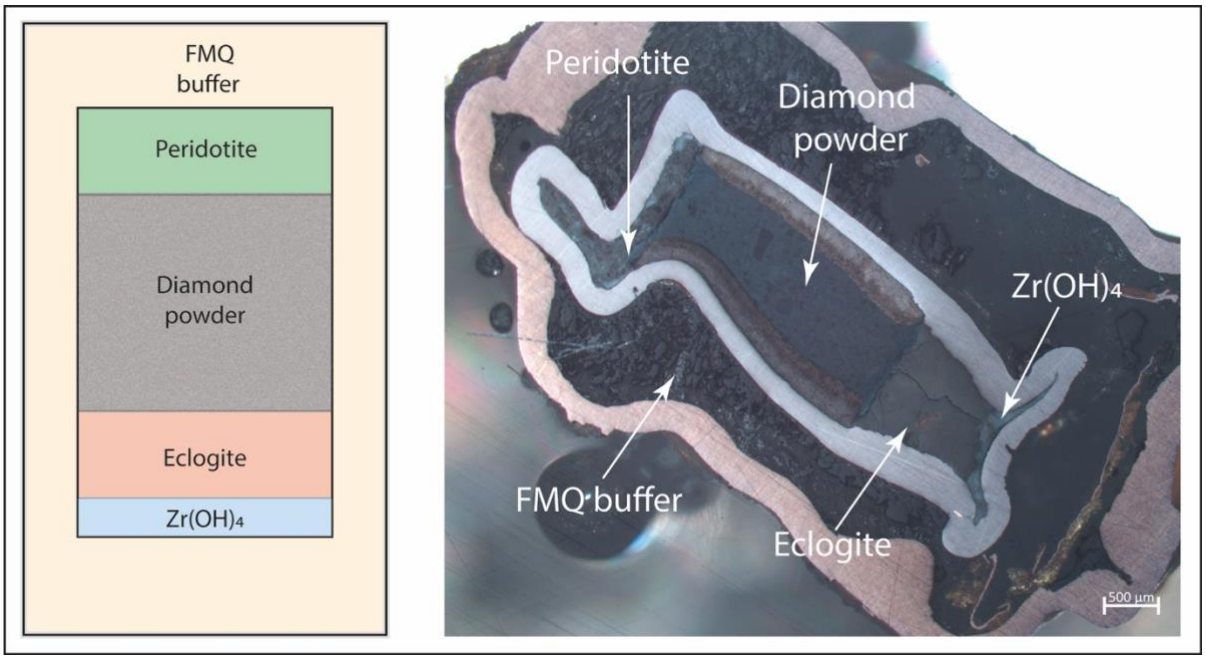

Figure 6.2 – Experimental setup for fluid-rock interaction in a piston cylinder. Experimental design for fluid-rock interaction in a piston-cylinder apparatus; b) Photograph of the capsule post-experiment. Experimental conditions are 3 GPa, 700 °C and ΔFMQ = 0.

6.3.6 Fluids and melts: different structures but same results?

Anhydrous metasomatic minerals have often been considered the result of melt metasomatism, despite textural and structural features not entirely compatible with a theoretical melt-rock interaction. In Chapter 3 and Chapter 4, models show that fluids have all the rock-forming elements and can precipitate anhydrous minerals, such as garnet, pyroxene, and olivine

(Chapter 4, **Fig. 4.3,** pp 78)**.** Therefore, hydrous minerals cannot be used as distinctive features of fluid-rock interaction, and different approaches (e.g., trace elements) must be considered. Fluids and melts are undistinguishable above the critical point (Kessel et al., 2005a, b), but this may also be partially true in a broader range of environmental conditions. Here, aqueous fluids and silicate melts have, without a doubt, different physical (structure) and geochemical (ligand) properties, but the results of their interaction with rocks may be the same. Fluids can be a hidden component of many geological systems and be more common than we assume. If the models presented in this work are correct, the role of the fluids in the Earth's mantle needs to be reconsidered, as they may be involved in a broader pool of geological processes than thought before. Experiments are required significantly to constrain the fluid's ability to precipitate anhydrous minerals and to evaluate its mass-transfer efficiency when compared to melt.

APPENDIX A

SUPPLEMENTARY MATERIAL FOR CHAPTER 2

Table A.1 - List of aqueous species and ions in the database used in this work.

Ag^{+}	CH_3COO^{-}	$Fe(OH)_3^{-}$	HCl	Mn^{2+}	SO_4^{2-}
$Al(OH)_3$	CH_3COOH	Fe^{2+}	HCO_3-	N_2	$Sr(CO_3)$
$Al(OH)_4^{-}$	CH_4	Fe^{3+}	HCOO-	Na^{+}	$Sr(HCO_3)^{+}$
Al(OH)Si(OH)	Cl^{-}	$FeCl^{+}$	HCOOH	$Na_2OTiOSi_2$	Sr^{2+}
$Al(OH)Si(OH)^{-}$	CN^{-}	$FeCl^{2+}$	Hg^{2+}	NaCl	$SrCl^{+}$
Al^{3+}	CO	$FeCl_2$	Hg_2^{2+}	$NaCO_3$-	$Ti(OH)_4$
Au^{+}	CO_2	$FeCl_2^{+}$	HPO_4^{2-}	$NaHCO_3$	$Ti(OH)_5^{-}$
Ba^{2+}	CO_3^{--}	$FeCl_3$	HS^{-}	$NaOAlO(SiO_2)_3$	$TiO(CHOO)_2^{-}$
$Ca(H_3SiO_4)^{+}$	Cr^{2+}	$FeCl_4^{-}$	HSO_4^{-}	NaOH	$TiOCHO^{-}$
$Ca(HCO_3)^{+}$	Cs^{+}	Glutamate	K^{+}	$NaOTi(OH)_4^{-}$	$TiOCHOO^{-}$
$Ca(HCOO)^{+}$	Cu^{+}	Glutamic	KCl	$NaOTiOSi_2^{-}$	$TiOSi^{-}$
$Ca(OH)^{+}$	Cu^{2+}	Glycine	KOH	$NaSO_4^{-}$	$TiOSi_2^{-}$
Ca^{2+}	Diglycine	H^{+}	KSO_4^{-}	$NaTi(OH)_5$	$TiOSi_2COOH^{-}$
$CaCl^{+}$	DKP	H_2	Methanol	$NaTiOSi_2$	$TiOSiCOOH^{-}$
$CaCl_2$	Ethane	H_2CO_3	$Mg(H_3SiO_4)^{+}$	NH_3	U^{4+}
$CaCO_3$	Ethanol	H_2O	$Mg(HCO_3)^{+}$	NH_4^{+}	UO_2^{2+}
CaOTiOSi	Ethylene	$H_2PO_4^{-}$	$Mg(OH)^{+}$	NO_3^{-}	UREA
$CaOTiOSi^{+}$	Eu^{2+}	H_2S	$Mg(OH)_2$	O_2	$Zr(OH)_4$
$CaOTiOSi_2$	F^{-}	H_3PO_4	Mg^{2+}	OH^{-}	Zr^{2+}
$CaSO_4$	$Fe(H_3SiO_4)^{+}$	$H_3SiO_4^{-}$	$MgCl^{+}$	Pb^{2+}	
Cd^{++}	$Fe(HCOO)^{+}$	H_4SiO_4	$MgCO_3$	Propane	
$CH_3CH_2COO^{-}$	$Fe(OH)^{+}$	$H_6Si_2O_7$	$MgSiC^{+}$	Propanol	
CH_3CH_2COOH	$Fe(OH)_2$	$H_8Si_3O_{10}$	$MgSO_4$	S_3^{-}	

Table A.2 - List of gaseous species in the database used in this work.

CH_4	H_2	H_2S	S_2
CO_2	H_2O	O_2	

Table A.3 - List of minerals in the database used in this work. For their chemical composition see the Research Data (name of the database: DATA0).

Albite	Coesite	Hedenbergite	Prehnite
Almandine	Cordierite	Hematite	Pseudo-wollastonite
Alunite	Corundum	Hydroxyapatite	Pumpellyite
Andalusite	Cristobalite-Alpha	Iron-Alpha	Pyrite
Andradite	Cristobalite-Beta	Iron-Gamma	Pyrope
Anhydrite	Diamond	Jadeite	Pyrophyllite
Annite	Diaspore	K-Feldspar	Pyrrhotite
Anorthite	Diopside	Kaolinite	Quartz-Alpha
Anthophyllite	Diopside05	Kyanite	Quartz-Beta
Antigorite	Dolomite	Lawsonite	Rutile
Aragonite	Enstatite-Clino	Lime	Siderite
Barite	Enstatite-Ortho	Magnesite	Sillimanite
Brucite	Fayalite	Magnetite	Spinel
Ca-Al-Pyroxene	Ferrosilite	Margarite	Strontianite
Calcite	Fluorapatite	Meionite	Sylvite
Celestite	Forsterite	Merwinite	Talc
Chamosite	Gehlenite	Monticellite	Tremolite
Chlorapatite	Glaucophane	Muscovite	Wollastonite
Chrysotile	Graphite	Paragonite	Zoisite
Clinochlore	Grossular	Periclase	
Clinozoisite	Halite	Phlogopite	

Table A.4 - List of the solid solutions in the database used in this work.

[a] Not used in Chapter 5

[b] In Chapter 5, Enstatite-Ortho is used instead

Apatite	Hydroxyapatite, Fluoroapatite, Chlorapatite
Biotite	Phlogopite, Annite
Calcite	Calcite, Magnesite, Siderite
Chlorite	Clinochlore, Chamosite
Cpx (Subcalcic)	Diopside, Hedenbergite, Enstatite-Clino[b], Jadeite
Garnet	Pyrope, Grossular, Almandine, Andradite[a]
K-Feldspar	K-Feldspar, Albite
Magnetite	Magnetite, Hematite
Olivine	Forsterite, Fayalite
Orthopyroxene	Enstatite-Ortho, Ferrosilite
Plagioclase	Albite, Anorthite

STEP-BY-STEP MODELLING PROCESS: EXAMPLE OF THE PROCEDURE

In this section, a step-by-step modelling process is provided, to improve the comprehension of the procedure described in Paragraph 2.3.1. Here, Model number 2 of Chapter 3 (Lherzolite + Eclogitic fluid, 0.25 mol/Kg of carbon in the system) is used as an example. For a detailed description of the choice of input parameters see Paragraph 3.3.2.

Step 1: Definition of the environmental parameters

Model 2 aims to calculate fluid-rock metasomatism at environmental conditions suitable for diamond formation. Therefore, the P-T-X-fO_2 parameters must be relevant to the geological environment under study (Stachel and Harris, 2008; Pearson et al., 2014; Stachel and Luth, 2015).

Pressure: 5 GPa

Temperature: 1000 °C

Oxygen Fugacity: logfO_2 = -3 ΔFMQ (equal to -10.4)

Chemical system: Na-Ca-Mg-Fe-Al-Si-C-O

Step 2: Fluid modelling

The silicic (eclogitic) fluid is based on an experimental calibration of aqueous fluid in equilibrium with a mafic eclogite (Kessel et al., 2015), documented in (Huang and Sverjensky, 2020). The geochemistry of the fluid in equilibrium with an eclogite is calculated through the aqueous speciation and solubility code EQ3 (Woolery, 1983, 1984, 1992). After setting each element of the chemical system in equilibrium with a mineral endmember (**Table A.5**), the software solves the required mathematical system (Paragraph 2.2.3).

Table A.5 - Composition of mineral assemblages, model parameters, and geochemistry of the initial fluid for Model 2 (Chapter 3).

	Eclogitic fluid	
Variable	**Set with**	**Concentration (mol/Kg)**
Na	Fixed	1.05
Ca	Diopside (0.350)	0.69
Mg	Pyrope (0.352)	0.05
Fe	Almandine (0.323)	0.07
Al	Grossular (0.326)	1.19
Si	Coesite	11.52
C	Fixed/Diamond	0.25
pH	Jadeite (0.539)	4.51
***f*O$_2$**	Fixed	-10.4

Step 3: Definition of the reactant host-rock

The reactant lithology used in this calculation is a lherzolite (**Table A.6**), a suitable diamond host-rock (Stachel and Harris, 2008).

Table A.6 - Mineralogical and solid solution compositions of lherzolite used in Model 2 (Chapter 3).

Mineral	Volume (%)	Moles	Endmember composition
Olivine	51	19.8	$Fo_{0.933}$ $Fa_{0.067}$
Orthopyroxene	18	5.4	$En_{0.938}$ $Fe_{0.062}$
Clinopyroxene	26	3.8	$Di_{0.294}$ $Hdn_{0.088}$ $Ja_{0.015}En_{0.603}$
Garnet	5	1.1	$Py_{0.733}$ $Gr_{0.137}$ $Alm_{0.130}$

Step 4: Modelling fluid-rock interaction

The chemical mass transfer code EQ6 (Woolery, 1983, 1984, 1992) has been used to model metasomatic interaction. The fluid calculated in Step 2 is forced to interact with the reactant lithology defined in Step 3. The established chemical potential drives the metasomatic reaction until the thermodynamic equilibrium is attained. The fluid progressively dissolves the host-rock, changing its composition and triggering the precipitation of metasomatic minerals. The evolution of the fluid geochemistry and chemical composition of garnets and clinopyroxenes are shown in **Table A.7** and **Table A.8**.

Table A.7 - Geochemistry of the fluid during the calculated metasomatic interaction (Model 2 – Chapter 3). The fluid dissolves a fixed amount of each reactant mineral in every step until the whole rock is dissolved and the thermodynamic equilibrium is attained. Each unit of the reaction progress variable (ξ) corresponds to the destruction of 1.0 mole of each reactant mineral per 1.0 kg of H_2O in the initial fluid.

logξ	**Reactant moles (cumulative)**				**Fluid geochemistry (mol/Kg of solvent)**							**Parameters**	
	Olivine	**Opx**	**Cpx**	**Garnet**	**Na**	**Ca**	**Mg**	**Al**	**Si**	**C**	**Fe**	**logfO_2**	**pH**
-999	0.00	0.00	0.00	0.00	1.03	0.46	0.05	0.84	10.99	0.19	0.07	-10.50	4.56
-8.00	$1.00x10^{-8}$	$1.00x10^{-8}$	$1.00x10^{-8}$	$1.00x10^{-8}$	1.03	0.46	0.05	0.84	10.99	0.19	0.07	-10.50	4.56
-7.50	$3.16x10^{-8}$	$3.16x10^{-8}$	$3.16x10^{-8}$	$3.16x10^{-8}$	1.03	0.46	0.05	0.84	10.99	0.19	0.07	-10.50	4.56
-7.00	$1.00x10^{-7}$	$1.00x10^{-7}$	$1.00x10^{-7}$	$1.00x10^{-7}$	1.03	0.46	0.05	0.84	10.99	0.19	0.07	-10.50	4.56
-6.50	$3.16x10^{-7}$	$3.16x10^{-7}$	$3.16x10^{-7}$	$3.16x10^{-7}$	1.03	0.46	0.05	0.84	10.99	0.19	0.07	-10.50	4.56
-6.00	$1.00x10^{-6}$	$1.00x10^{-6}$	$1.00x10^{-6}$	$1.00x10^{-6}$	1.03	0.46	0.05	0.84	10.99	0.19	0.07	-10.50	4.56
-5.50	$3.16x10^{-6}$	$3.16x10^{-6}$	$3.16x10^{-6}$	$3.16x10^{-6}$	1.03	0.46	0.05	0.84	10.99	0.19	0.07	-10.50	4.56
-5.00	$1.00x10^{-5}$	$1.00x10^{-5}$	$1.00x10^{-5}$	$1.00x10^{-5}$	1.03	0.46	0.05	0.84	10.99	0.19	0.07	-10.50	4.56
-4.50	$3.16x10^{-5}$	$3.16x10^{-5}$	$3.16x10^{-5}$	$3.16x10^{-5}$	1.03	0.46	0.05	0.84	10.99	0.19	0.07	-10.50	4.56
-4.00	$1.00x10^{-4}$	$1.00x10^{-4}$	$1.00x10^{-4}$	$1.00x10^{-4}$	1.03	0.46	0.05	0.84	10.99	0.19	0.07	-10.50	4.56
-3.50	$3.16x10^{-4}$	$3.16x10^{-4}$	$3.16x10^{-4}$	$3.16x10^{-4}$	1.03	0.46	0.05	0.84	10.99	0.19	0.07	-10.50	4.56
-3.00	$1.00x10^{-3}$	$1.00x10^{-3}$	$1.00x10^{-3}$	$1.00x10^{-3}$	1.03	0.46	0.06	0.84	10.99	0.19	0.07	-10.50	4.56
-2.70	$2.00x10^{-3}$	$2.00x10^{-3}$	$2.00x10^{-3}$	$2.00x10^{-3}$	1.03	0.46	0.06	0.84	11.00	0.19	0.07	-10.51	4.57
-2.62	$2.41x10^{-3}$	$2.41x10^{-3}$	$2.41x10^{-3}$	$2.41x10^{-3}$	1.03	0.46	0.06	0.84	11.00	0.19	0.07	-10.51	4.56
-2.50	$3.16x10^{-3}$	$3.16x10^{-3}$	$3.16x10^{-3}$	$3.16x10^{-3}$	1.03	0.46	0.06	0.84	10.99	0.19	0.07	-10.51	4.56
-2.00	$1.00x10^{-2}$	$1.00x10^{-2}$	$1.00x10^{-2}$	$1.00x10^{-2}$	1.01	0.44	0.07	0.83	10.93	0.19	0.07	-10.51	4.55
-1.66	$2.20x10^{-2}$	$2.20x10^{-2}$	$2.20x10^{-2}$	$2.20x10^{-2}$	0.99	0.42	0.07	0.82	10.84	0.19	0.07	-10.52	4.54
-1.50	$3.16x10^{-2}$	$3.16x10^{-2}$	$3.16x10^{-2}$	$3.16x10^{-2}$	0.98	0.40	0.08	0.80	10.79	0.19	0.07	-10.53	4.53
-1.00	$1.00x10^{-1}$	$1.00x10^{-1}$	$1.00x10^{-1}$	$1.00x10^{-1}$	0.93	0.33	0.09	0.70	10.54	0.19	0.05	-10.55	4.53
-0.50	$3.16x10^{-1}$	$3.16x10^{-1}$	$3.16x10^{-1}$	$3.16x10^{-1}$	0.86	0.21	0.12	0.52	10.11	0.19	0.05	-10.58	4.54
-0.32	$4.80x10^{-1}$	$4.80x10^{-1}$	$4.80x10^{-1}$	$4.80x10^{-1}$	0.83	0.17	0.13	0.45	9.90	0.19	0.06	-10.59	4.54

0.00	1.00	1.00	1.00	1.00	0.78	0.18	0.13	0.44	9.50	0.18	0.06	-10.59	4.54
0.04	1.10	1.10	1.10	1.10	0.78	0.18	0.13	0.43	9.43	0.18	0.06	-10.59	4.53
0.50	3.16	3.16	3.16	1.10	0.69	0.19	0.14	0.40	8.13	0.18	0.06	-10.59	4.53
0.58	3.80	3.80	3.80	1.10	0.68	0.19	0.14	0.39	7.76	0.18	0.06	-10.58	4.53
0.73	5.40	5.40	3.80	1.10	0.69	0.19	0.14	0.39	6.96	0.17	0.05	-10.58	4.54
1.00	10.00	5.40	3.80	1.10	0.73	0.18	0.15	0.37	4.83	0.17	0.05	-10.57	4.60
1.25	17.76	5.40	3.80	1.10	0.81	0.14	0.25	0.28	1.74	0.15	0.04	-10.54	4.76
1.30	19.80	5.40	3.80	1.10	0.82	0.12	0.30	0.24	1.29	0.15	0.03	-10.74	4.78

Table A.8 - Geochemistry of metasomatic clinopyroxenes and garnets during the calculated metasomatic interaction (Model 2 – Chapter 3). The fluid dissolves a fixed amount of each reactant mineral in every step until the whole rock is dissolved and the thermodynamic equilibrium is attained. Each unit of the reaction progress variable (ξ) corresponds to the destruction of 1.0 mole of each reactant mineral per 1.0 kg of H_2O in the initial fluid.

logξ	**Reactant moles (cumulative)**				**Clinopyroxene**				**Garnet**			
	Olivine	**Opx**	**Cpx**	**Garnet**	**Dio**	**Hdn**	**En**	**Jd**	**Py**	**Alm**	**Gr**	**And**
-999	0.00	0.00	0.00	0.00								
-8.00	$1.00x10^{-8}$	$1.00x10^{-8}$	$1.00x10^{-8}$	$1.00x10^{-8}$								
-7.50	$3.16x10^{-8}$	$3.16x10^{-8}$	$3.16x10^{-8}$	$3.16x10^{-8}$								
-7.00	$1.00x10^{-7}$	$1.00x10^{-7}$	$1.00x10^{-7}$	$1.00x10^{-7}$								
-6.50	$3.16x10^{-7}$	$3.16x10^{-7}$	$3.16x10^{-7}$	$3.16x10^{-7}$								
-6.00	$1.00x10^{-6}$	$1.00x10^{-6}$	$1.00x10^{-6}$	$1.00x10^{-6}$								

-5.50	$3.16x10^{-6}$	$3.16x10^{-6}$	$3.16x10^{-6}$	$3.16x10^{-6}$								
-5.00	$1.00x10^{-5}$	$1.00x10^{-5}$	$1.00x10^{-5}$	$1.00x10^{-5}$								
-4.50	$3.16x10^{-5}$	$3.16x10^{-5}$	$3.16x10^{-5}$	$3.16x10^{-5}$								
-4.00	$1.00x10^{-4}$	$1.00x10^{-4}$	$1.00x10^{-4}$	$1.00x10^{-4}$								
-3.50	$3.16x10^{-4}$	$3.16x10^{-4}$	$3.16x10^{-4}$	$3.16x10^{-4}$								
-3.00	$1.00x10^{-3}$	$1.00x10^{-3}$	$1.00x10^{-3}$	$1.00x10^{-3}$								
-2.70	$2.00x10^{-3}$	$2.00x10^{-3}$	$2.00x10^{-3}$	$2.00x10^{-3}$	0.47	0.09	0.06	0.38				
-2.62	$2.41x10^{-3}$	$2.41x10^{-3}$	$2.41x10^{-3}$	$2.41x10^{-3}$	0.47	0.09	0.06	0.38				
-2.50	$3.16x10^{-3}$	$3.16x10^{-3}$	$3.16x10^{-3}$	$3.16x10^{-3}$	0.47	0.09	0.06	0.38				
-2.00	$1.00x10^{-2}$	$1.00x10^{-2}$	$1.00x10^{-2}$	$1.00x10^{-2}$	0.48	0.08	0.07	0.37				
-1.66	$2.20x10^{-2}$	$2.20x10^{-2}$	$2.20x10^{-2}$	$2.20x10^{-2}$	0.49	0.07	0.09	0.36	0.54	0.28	0.16	0.01
-1.50	$3.16x10^{-2}$	$3.16x10^{-2}$	$3.16x10^{-2}$	$3.16x10^{-2}$	0.49	0.07	0.10	0.35	0.57	0.26	0.16	0.01
-1.00	$1.00x10^{-1}$	$1.00x10^{-1}$	$1.00x10^{-1}$	$1.00x10^{-1}$	0.51	0.04	0.16	0.29	0.67	0.20	0.12	0.01
-0.50	$3.16x10^{-1}$	$3.16x10^{-1}$	$3.16x10^{-1}$	$3.16x10^{-1}$	0.47	0.03	0.29	0.20	0.76	0.17	0.06	0.01
-0.32	$4.80x10^{-1}$	$4.80x10^{-1}$	$4.80x10^{-1}$	$4.80x10^{-1}$	0.44	0.03	0.37	0.17	0.77	0.18	0.05	0.01
0.00	1.00	1.00	1.00	1.00	0.45	0.03	0.37	0.15	0.78	0.17	0.05	0.01
0.04	1.10	1.10	1.10	1.10	0.45	0.03	0.37	0.15	0.78	0.17	0.05	0.01
0.50	3.16	3.16	3.16	1.10	0.49	0.03	0.37	0.11	0.78	0.16	0.05	0.01
0.58	3.80	3.80	3.80	1.10	0.49	0.03	0.37	0.11	0.77	0.16	0.05	0.01
0.73	5.40	5.40	3.80	1.10	0.50	0.03	0.37	0.10	0.78	0.16	0.06	0.01
1.00	10.00	5.40	3.80	1.10	0.52	0.03	0.37	0.08	0.78	0.16	0.06	0.01
1.25	17.76	5.40	3.80	1.10	0.56	0.03	0.38	0.03	0.77	0.15	0.06	0.01
1.30	19.80	5.40	3.80	1.10	0.57	0.03	0.38	0.02	0.79	0.13	0.06	0.01

Step 5: Analysis of results

The results in **Table A.7** and **Table A.8** are plotted against natural data to verify the agreement and to analyse the results (**Fig. A.1**).

Figure A.1 - Evolution of the metasomatic system in Model 2 (Chapter 3). [a] and [b] evolution of the fluid composition; [c] garnet geochemistry; [d] clinopyroxene geochemistry.

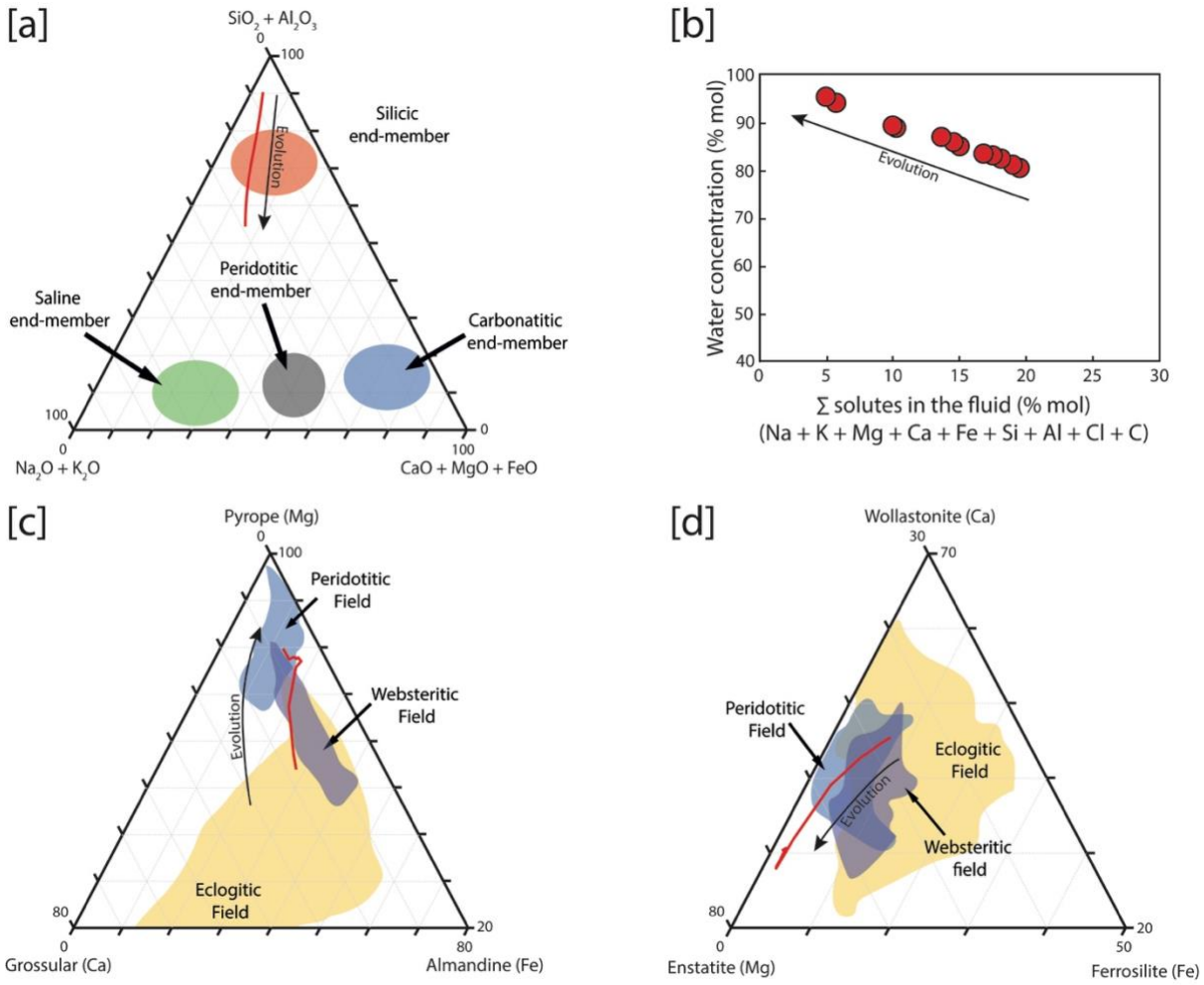

APPENDIX B

SUPPLEMENTARY MATERIAL FOR CHAPTER 3

Table B.1 - Composition of mineral assemblages and model parameters for eclogitic, peridotitic and carbonatitic fluids. This table is reproduced from Chapter 2 (Paragraph 2.3.1).

	Eclogitic	**Peridotitic**	**Carbonatitic**
Variable	**Set with**	**Set with**	**Set with**
K	-	Phlogopite	Fixed
Na	Fixed	Fixed	Fixed
Ca	Diopside (0.350)	Grossular (0.100)	Calcite (0.500)
Mg	Pyrope (0.352)	Forsterite (0.920)	Magnesite (0.450)
Fe	Almandine (0.323)	Fayalite (0.080)	Fayalite (0.080)
Al	Grossular (0.326)	Pyrope (0.800)	Grossular (0.300)
Si	Coesite	Clinoenstatite (0.955)	Forsterite (0.920)
Cl	-	Fixed	Fixed
C	Fixed/Diamond	Fixed/Diamond	Diamond
pH	Jadeite (0.539)	Jadeite (0.015)	Fixed
$f\mathbf{O_2}$	Fixed	Fixed	Fixed

Table B.2 - The initial composition (molality concentration [moles/kg H_2O]) of eclogitic, peridotitic and carbonatitic diamond-forming fluids and control parameters at 5 GPa, 1000 ºC, and logfO_2 = -2 and -4 ΔFMQ.

	ECLOGITIC		**PERIDOTITIC**		**CARBONATITIC**
	Diamond forming		**Diamond forming**		**Diamond forming**
Name	E_diamond	E_diamond	P_diamond	P_diamond	C_diamond
C	18.73	8.47	27.77	8.07	30.56
K	0.00	0.00	1.48	2.62	0.50
Na	1.94	1.04	2.00	2.00	0.50
Ca	0.98	0.68	1.12	0.91	8.40
Mg	2.34	0.06	9.32	0.50	2.48
Fe	0.42	0.11	0.75	1.57	0.48
Al	1.65	1.11	0.19	0.09	0.06
Si	9.19	9.14	10.63	2.26	3.11
Cl	0.00	0.00	8.00	8.00	1.00
pH	4.87	4.56	5.15	4.59	4.49
***f*O$_2$ (log)**	-9.4	-11.4	-9.4	-11.4	-9.4
P (GPa)	5		5		5
T (^{o}C)	1000		1000		1000

Table B.3 - Most relevant carbon species (logarithm of molality concentration [moles/kg H_2O]) in the initial eclogitic, peridotitic and carbonatitic fluids at 5 GPa, 1000 ºC, and logfO_2 = -2 to -4 ΔFMQ. $MgSiC^+$ is an abbreviation for $Mg(SiO_2)(HCO_3)^+$.

PARAMETERS			**CARBON SPECIATION (log conc)**										
Fluid	**ΔFMQ**	**Initial C (mol)**	**$MgSiC^+$**	**CH_4**	**$HCOO^-$**	**CH_3COO^-**	**CO**	**CO_2**	**H_2CO_3**	**HCO_3^-**	**CO_3^{--}**	**$Ca(HCOO)^+$**	**$Fe(HCOO)^+$**
Eclogitic	-2	18.73	0.37	-1.39	0.13	-3.06	-2.15	-0.57	1.09	-1.36	-1.76	-0.20	-0.40
	-3	0											
	-3	0.25	-1.41	-1.39	-1.86	-5.55	-3.84	-2.77	-1.00	-3.86	-4.75	-1.58	-1.79
	-3	0.50	-1.12	-1.08	-1.55	-4.93	-3.54	-2.47	-0.70	-3.54	-4.42	-1.29	-1.49
	-3	0.75	-0.95	-0.91	-1.37	-4.58	-3.36	-2.30	-0.52	-3.36	-4.22	-1.11	-1.32
	-3	1.00	-0.83	-0.79	-1.22	-4.32	-3.24	-2.16	-0.40	-3.22	-4.07	-0.99	-1.20
	-3	3.13	-0.40	-0.31	-0.66	-3.27	-2.73	-1.66	0.09	-2.66	-3.41	-0.55	-0.75
	-4	8.47	-1.37	0.67	-1.21	-3.34	-3.21	-2.64	-0.91	-3.71	-4.54	-1.01	-1.21
Peridotitic	-2	27.77	0.96	-1.47	0.45	-2.81	-2.07	-0.50	1.09	-1.04	-1.04	-0.05	-0.25
	-3	0											
	-3	0.25	-0.90	-1.77	-2.15	-6.22	-4.16	-3.09	-1.35	-4.14	-4.88	-1.55	-1.75
	-3	0.50	-0.60	-1.46	-1.83	-5.59	-3.86	-2.78	-1.04	-3.82	-4.54	-1.25	-1.46

	-3	0.75	-0.43	-1.28	-1.64	-5.22	-3.67	-2.60	-0.86	-3.63	-4.34	-1.08	-1.28
	-3	1.00	-0.31	-1.15	-1.49	-4.94	-3.54	-2.46	-0.73	-3.49	-4.17	-0.96	-1.16
	-3	5.58	0.36	-0.36	-0.49	-3.14	-2.68	-1.61	0.94	-2.48	-2.97	-0.26	-0.47
	-4	8.07	-0.51	0.64	-1.14	-3.30	-3.18	-2.60	-0.91	-3.63	-4.29	-0.62	-0.83
Carbonatitic	-2	30.56	0.34	-1.45	0.79	-2.46	-2.09	-0.52	1.09	-0.71	-0.38	0.88	-0.33
	-3	17.96	-1.97	-0.42	0.60	-2.11	-2.62	-1.55	0.09	-1.39	-0.75	1.04	-0.17

Table B.4 - Final mineralogy (% volume) after fluid-rock interaction at 5 GPa, 1000 ºC, and logfO_2 = -2 to -4 ΔFMQ for selected models. Minerals: Kyanite (Ky), Garnet (Grt), Clinopyroxene (Cpx), Orthopyroxene (Opx), Magnetite-Hematite (Ma-He), Meionite (Mei), Olivine (Ol), Diamond (Dia).

INPUT PARAMETERS					**METASOMATIC MINERAL COMPOSITION (vol. %)**										
Model	**Initial rock**	**Fluid**	**ΔFMQ**	**Carbon (molality)**	**Ky**	**Grt**	**Cpx**	**Opx**	**MaHe**	**Mei**	**Coe**	**Ol**	**Dia**	**Dol**	**Bru**
1	Lhz	Ecl	-3	0.00		8.41	19.06	72.48	0.05						
2	Lhz	Ecl	-3	0.25		6.88	17.78	74.85	0.50						
3	Lhz	Ecl	-3	0.50		6.61	17.57	75.17	0.65						
4	Lhz	Ecl	-3	0.75		6.50	17.45	75.30	0.76						
5	Lhz	Ecl	-3	1.00		6.44	17.37	75.35	0.84						
56	Ecl T2	Per	-3	0.00	2.89	26.73	70.15				0.22				
57	Ecl T3	Per	-3	0.25		23.83	64.01			11.92	0.23				
58	Ecl T4	Per	-3	0.50		21.48	62.46			15.83	0.23				
59	Ecl T5	Per	-3	0.75		20.60	61.61			17.52	0.27				
60	Ecl T6	Per	-3	1.00		20.07	61.07			18.60	0.26				
91	Lhz	Ecl	-3	3.13		6.52	16.80	75.23	1.36			0.09			
92	Lhz	Per	-3	5.58		10.45	34.04	55.24	0.26						

93	Dun	Ecl	-3	3.13		8.52	7.03	82.88	1.46			0.11			
94	Dun	Per	-3	5.58		17.68	22.26	59.86				0.21			
95	Harz	Ecl	-3	3.13		7.87	2.04	88.56	1.41			0.11			
96	Harz	Per	-3	5.58		19.15	5.45	75.19				0.21			
97	Ecl T2	Ecl	-3	3.13		0.69	35.15			50.84	13.32				
98	Ecl T3	Per	-3	5.58		30.15	55.09			13.96	0.33		0.47		
99	Ecl T4	Ecl	-3	3.13		0.51	32.16			49.23	18.11				
100	Ecl T5	Per	-3	5.58		15.92	59.07			24.38	0.28		0.35		
101	Ecl T6	Ecl	-3	3.13		0.24	50.06			49.70					
102	Ecl T7	Per	-3	5.58		1.28	97.39						1.34		
103	Web	Ecl	-3	3.13		13.30	57.02	29.68							
104	Web	Per	-3	5.58		15.18	58.26	25.13	1.43						
105	Orthopy	Ecl	-3	3.13		37.88	35.96	26.17							
106	Orthopy	Per	-3	5.58		35.65	28.03	36.32							
107	Clinopy	Ecl	-3	3.13		17.47	82.53								
108	Clinopy	Per	-3	5.58		28.62	71.38								
109	Lhz	Ecl	-2	18.70		8.27	19.70	69.27	2.68			0.07			
118	Ecl T2	Per	-2	27.77		15.82	48.36		0.37	34.40	0.35		0.71		
127	Lhz	Ecl	-4	8.47		7.69	19.29	72.86	0.03			0.13			

136	Ecl T2	Per	-4	8.07		20.74	60.89			17.92	0.27		0.18		
145	Lhz	Carb	-2	30.56			54.20		2.16	11.89		35.16	1.24	1.19	
146	Lhz	Carb	-3	17.96			49.19		2.06	7.10		40.19	1.46		
147	Dun	Carb	-2	30.56			49.28		2.08	11.89		0.47	2.24	34.03	
148	Dun	Carb	-3	17.96		12.53	46.25		2.25			1.27	2.08		35.63
149	Harz	Carb	-2	30.56			38.86		2.48	7.49		38.92	1.60	10.65	
150	Harz	Carb	-3	17.96		11.53	34.02		2.35			44.13	1.75		6.21
152	Ecl T1	Carb	-3	17.96			58.12		2.28	37.74			1.85		
154	Ecl T2	Carb	-3	17.96			46.88		3.98	44.6	3.08		1.45		
156	Ecl T3	Carb	-3	17.96		96.05	0.07		1.03				2.85		
158	Web	Carb	-3	17.96		5.28	71.81		4.47			16.88	1.56		
160	Orthopy	Carb	-3	17.96		4.96	58.59		3.31			31.13	2.02		
161	Clinopy	Carb	-2	30.56			58.61		2.63	26.65		0.27	1.10	10.73	
162	Clinopy	Carb	-3	17.96		36.11	50.71		1.91				1.44		9.83

Table B.5 - Final fluid composition (molality concentration [moles/kg H_2O]) after fluid-rock interaction at 5 GPa, 1000 ºC, and logfO_2 = -2 to -4 ΔFMQ for selected models.

	FLUID COMPOSITION (molal conc)									PARAMETERS	
Model	**Na**	**Ca**	**Mg**	**Al**	**Si**	**Fe**	**C**	**K**	**Cl**	fO_2	**pH**
1	0.82	0.12	0.29	0.23	1.19	0.02				-11.15	4.80
2	0.82	0.12	0.30	0.24	1.29	0.03	0.15			-10.75	4.80
3	0.82	0.13	0.34	0.25	1.33	0.04	0.34			-10.64	4.81
4	0.82	0.14	0.39	0.26	1.35	0.05	0.53			-10.59	4.83
5	0.82	0.15	0.43	0.26	1.36	0.06	0.73			-10.56	4.84
56	2.40	0.93	0.01	0.70	7.87	2.15		2.81	9.17	-11.18	4.38
57	2.60	0.68	0.03	0.64	7.66	2.19	0.11	2.74	9.09	-10.64	4.41
58	2.72	0.58	0.09	0.59	7.56	2.20	0.34	2.68	9.04	-10.46	4.44
59	2.78	0.54	0.16	0.57	7.52	2.21	0.61	2.64	9.02	-10.39	4.46
60	2.81	0.53	0.24	0.56	7.51	2.21	0.88	2.59	9.00	-10.36	4.47
91	0.85	0.23	0.78	0.27	1.43	0.14	2.40			-10.50	4.94
92	1.92	0.76	2.06	0.13	2.49	1.61	5.11	1.83	7.66	-10.30	4.71
93	0.84	0.23	0.79	0.26	1.44	0.14	2.40			-10.49	4.93
94	1.91	0.79	2.12	0.12	2.54	1.52	5.11	1.83	7.66	-10.30	4.69
95	0.83	0.23	0.79	0.26	1.44	0.14	2.40			-10.49	4.93
96	1.91	0.79	2.12	0.12	2.54	1.53	5.11	1.83	7.66	-10.30	4.69
97	1.17	0.35	0.54	0.87	10.61	0.31	2.94			-10.45	4.72
98	2.93	0.47	1.88	0.56	8.09	1.88	5.23	2.09	8.74	-10.23	4.53
99	1.20	0.36	0.49	0.86	10.56	0.34	2.92			-10.45	4.73
100	2.86	0.51	1.60	0.54	7.91	2.14	5.15	2.08	8.72	-10.23	4.57
101	1.32	0.36	0.42	0.88	10.53	0.36	2.85			-10.45	4.74
102	2.04	0.89	2.10	0.25	3.85	1.37	5.26	1.89	7.92	-10.32	4.58
103	0.67	0.20	0.80	0.54	8.10	0.27	2.80			-10.48	4.76
104	1.90	0.62	2.03	0.16	2.90	1.75	5.16	1.85	7.74	-10.32	4.69

105	0.89	0.16	0.83	0.61	9.24	0.22	2.87			-10.48	4.76
106	1.93	0.61	2.18	0.17	3.20	1.58	5.19	1.86	7.79	-10.33	4.65
107	0.84	0.34	0.69	0.74	7.86	0.20	2.80			-10.46	4.72
108	2.55	0.92	1.64	0.25	2.99	1.54	5.20	1.86	7.79	-10.27	4.69
109	1.68	0.40	3.56	0.34	4.21	0.17	15.76			-9.34	5.22
118	2.82	0.43	8.15	0.54	11.81	1.13	28.02	1.54	8.34	-9.33	4.95
127	0.86	0.15	0.36	0.20	0.96	0.10	6.88			-11.46	4.89
136	2.70	0.60	0.09	0.53	6.13	2.02	8.10	2.87	8.75	-11.44	4.49
146	0.52	7.15	1.13	0.25	0.50	0.09	13.8	0.47	0.95	-10.06	5.54
148	0.53	8.78	1.16	0.24	0.41	0.08	15.93	0.52	1.04	-10.09	5.62
150	0.48	8.26	1.16	0.24	0.42	0.08	14.95	0.48	0.97	-10.11	5.61
152	3.56	0.57	0.94	0.62	4.87	0.37	8.08	0.49	0.98	-9.92	4.97
154	1.62	0.54	1.17	0.66	9.46	0.52	6.65	0.53	1.06	-9.97	4.83
156	0.88	10.16	0.99	0.20	0.31	0.05	16.47	0.49	0.97	-10.32	5.74
158	0.63	3.07	1.40	0.25	1.29	0.19	10.30	0.46	0.92	-9.90	5.23
160	0.46	2.57	1.63	0.25	1.61	0.21	10.40	0.46	0.93	-9.85	5.18
162	1.38	8.62	1.12	0.23	0.37	0.07	15.38	0.49	0.99	-10.20	5.66

Table B.6 - Most relevant carbon species (logarithm of molality concentration [moles/kg H_2O]) in the final fluid after fluid-rock interaction at 5 GPa, 1000 ºC, and logfO_2 = -2 to -4 ΔFMQ for selected models. $MgSiC^+$ is an abbreviation for $Mg(SiO_2)(HCO_3)^+$.

PARAMETERS			**CARBON SPECIATION (log conc)**										
Model	***f*O₂**	**Initial C (mol)**	**$MgSiC^+$**	**CH_4**	**$HCOO^-$**	**CH_3COO^-**	**CO**	**CO_2**	**H_2CO_3**	**HCO_3^-**	**CO_3^{--}**	**$Ca(HCOO)^+$**	**$Fe(HCOO)^+$**
1	-11.15	0.00											
2	-10.75	0.25	-1.63	-1.19	-1.98	-5.64	-4.25	-3.35	-1.54	-4.14	-4.86	-2.11	-1.99
3	-10.64	0.50	-1.20	-0.97	-1.57	-4.96	-3.86	-2.90	-1.10	-3.69	-4.38	-1.73	-1.64
4	-10.59	0.75	-0.99	-0.84	-1.35	-4.58	-3.65	-2.67	-0.87	-3.44	-4.11	-1.53	-1.46
5	-10.56	1.00	-0.84	-0.74	-1.20	-4.31	-3.51	-2.52	-0.72	-3.27	-3.92	-1.39	-1.33
56	-11.18	0.00											
57	-10.64	0.25	-1.75	-1.52	-2.35	-6.29	-4.23	-3.28	-1.56	-4.47	-5.30	-2.00	-1.83
58	-10.46	0.50	-1.13	-1.30	-1.82	-5.45	-3.73	-2.68	-0.97	-3.84	-4.64	-1.58	-1.31
59	-10.39	0.75	-0.84	-1.17	-1.57	-5.02	-3.49	-2.41	-0.70	-3.55	-4.33	-1.39	-1.07
60	-10.36	1.00	-0.66	-1.06	-1.40	-4.74	-3.34	-2.24	-0.53	-3.37	-4.14	-1.26	-0.91
91	-10.50	3.13	-0.37	-0.33	-0.56	-3.24	-2.98	-1.96	-0.17	-2.61	-3.11	-0.85	-0.89
92	-10.3	5.58	0.24	-0.49	-0.52	-3.26	-2.70	-1.57	0.14	-2.46	-2.99	-0.27	-0.36
93	-10.49	3.13	-0.36	-0.34	-0.56	-3.25	-2.98	-1.95	-0.16	-2.60	-3.10	-0.85	-0.89

94	-10.30	5.58	0.26	-0.49	-0.53	-3.27	-2.70	-1.58	0.14	-2.48	-3.02	-0.26	-0.40
95	-10.49	3.13	-0.36	-0.34	-0.56	-3.25	-2.98	-1.95	-0.16	-2.60	-3.11	-0.85	-0.89
96	-10.3	5.58	0.26	-0.49	-0.53	-3.27	-2.70	-1.58	0.14	-2.48	-3.02	-0.26	-0.40
97	-10.45	3.13	-0.29	-0.30	-0.62	-3.23	-2.80	-1.75	0.00	-2.63	-3.29	-0.98	-0.63
98	-10.23	5.58	0.27	-0.54	-0.60	-3.35	-2.59	-1.43	0.26	-2.51	-3.2	-0.73	-0.38
99	-10.45	3.13	-0.33	-0.30	-0.61	-3.23	-2.80	-1.75	0.00	-2.62	-3.27	-0.96	-0.59
100	-10.23	5.58	0.20	-0.54	-0.57	-3.32	-2.59	-1.43	0.26	-2.47	-3.12	-0.69	-0.27
101	-10.45	3.13	-0.40	-0.31	-0.60	-3.23	-2.81	-1.76	-0.01	-2.62	-3.26	-0.97	-0.56
102	-10.32	5.58	0.30	-0.43	-0.59	-3.28	-2.65	-1.53	0.18	-2.55	-3.19	-0.31	-0.53
103	-10.48	3.13	-0.14	-0.31	-0.65	-3.29	-2.88	-1.84	-0.07	-2.68	-3.33	-1.22	-0.69
104	-10.32	5.58	0.26	-0.44	-0.52	-3.21	-2.68	-1.57	0.15	-2.47	-3.02	-0.41	-0.31
105	-10.48	3.13	-0.11	-0.29	-0.64	-3.26	-2.86	-1.83	-0.07	-2.67	-3.31	-1.32	-0.78
106	-10.33	5.58	0.30	-0.44	-0.55	-3.25	-2.68	-1.56	0.15	-2.51	-3.09	-0.43	-0.40
107	-10.46	3.13	-0.20	-0.31	-0.66	-3.29	-2.85	-1.81	-0.04	-2.68	-3.35	-0.97	-0.80
108	-10.27	5.58	0.18	-0.50	-0.49	-3.22	-2.65	-1.51	0.20	-2.42	-2.96	-0.25	-0.37
109	-9.34	18.73	0.51	-1.65	0.28	-3.13	-2.38	-0.77	0.93	-1.18	-1.24	-0.47	-0.77
118	-9.33	27.77	0.91	-1.55	0.29	-3.02	-2.03	-0.42	1.17	-1.17	-1.38	-0.53	-0.12
127	-11.46	8.47	-1.30	0.62	-1.10	-3.30	-3.43	-2.88	-1.11	-3.62	-4.22	-1.27	-1.11
136	-11.44	8.07	-1.12	0.66	-1.26	-3.42	-3.18	-2.63	-0.95	-3.78	-4.52	-1.06	-0.80

146	-10.06	17.96	-0.78	-0.70	0.49	-2.34	-2.51	-1.27	0.43	-1.33	-1.00	0.84	-1.04
148	-10.09	17.96	-0.94	-0.70	0.57	-2.26	-2.50	-1.27	0.41	-1.26	-0.82	0.93	-1.11
150	-10.11	17.96	-0.94	-0.66	0.54	-2.28	-2.52	-1.31	0.38	-1.31	-0.89	0.90	-1.11
152	-9.92	17.96	-0.04	-0.82	-0.03	-2.90	-2.46	-1.15	0.57	-1.78	-2.10	-0.48	-0.49
154	-9.97	17.96	0.06	-0.76	-0.20	-3.04	-2.49	-1.20	0.52	-1.98	-2.44	-0.60	-0.37
156	-10.32	17.96	-1.45	-0.47	0.58	-2.15	-2.61	-1.50	0.17	-1.37	-0.80	0.99	-1.28
158	-9.90	17.96	-0.10	-0.84	0.25	-2.64	-2.46	-1.13	0.60	-1.49	-1.53	0.45	-0.74
160	-9.85	17.96	0.03	-0.89	0.22	-2.68	-2.43	-1.08	0.65	-1.49	-1.58	0.37	-0.68
162	-10.20	17.96	-1.13	-0.58	0.55	-2.23	-2.56	-1.39	0.29	-1.35	-0.87	0.92	-1.17

Figure B.1 - Geochemistry of garnet and clinopyroxene precipitated during progressive fluid-rock interaction for peridotitic (a, b), eclogitic (c, d) and carbonatitic (e, f) fluids with a range of host rocks at 5 GPa, 1000 ºC, and logfO_2 = -3 ΔFMQ. The initial amount of carbon in the fluids is in equilibrium with diamond (diamond-forming fluids). The numbers in parentheses refer to the model run number.

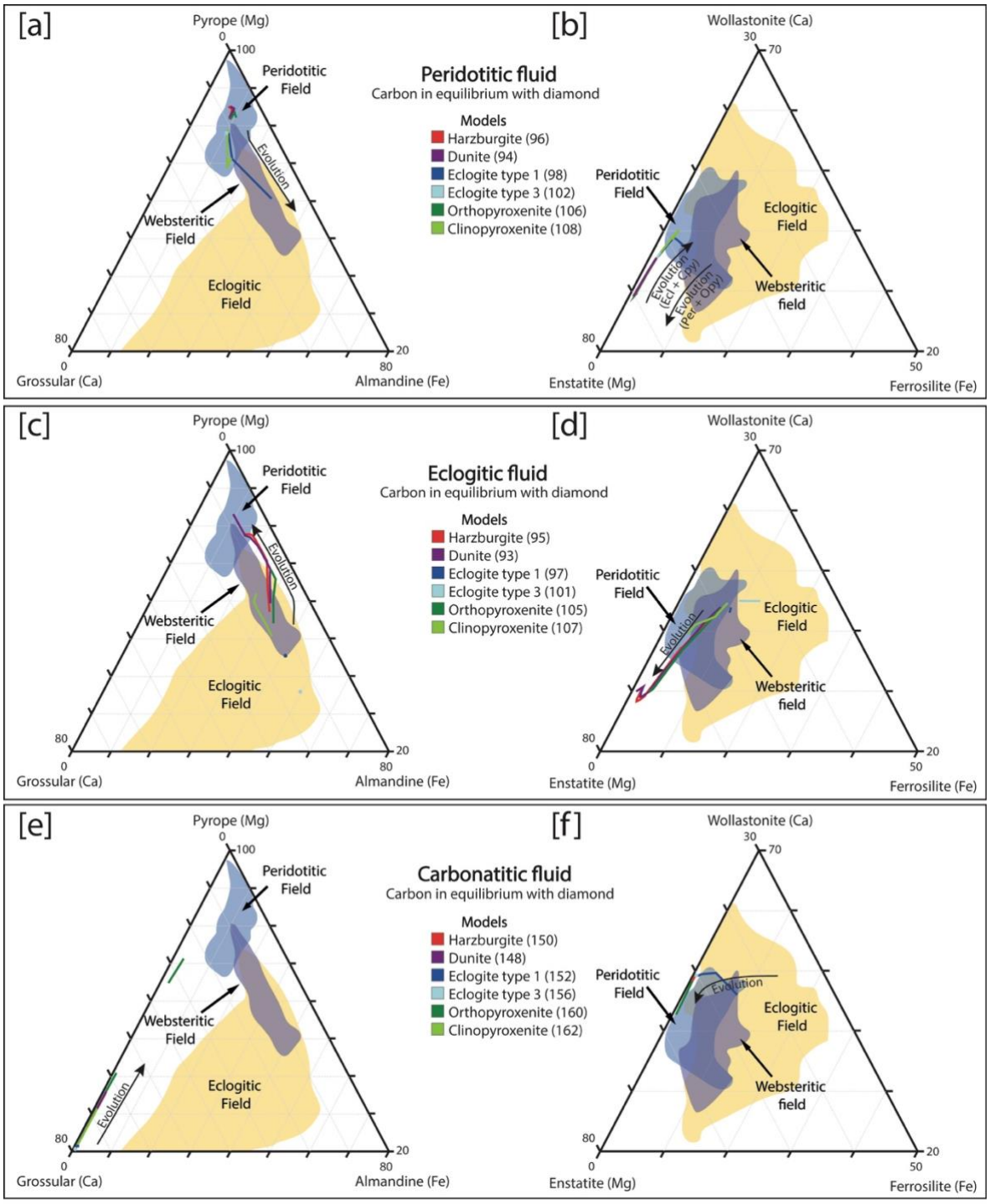

Figure B.2 - Geochemistry of clinopyroxene (including jadeite) precipitated during progressive fluid-rock interaction for fluids in equilibrium with diamond (a, b, c) and different amounts of carbon (d, e) at 5 GPa, 1000 ºC, and logfO_2 = -2 to -4 ΔFMQ. The numbers in parentheses refer to the model run number.

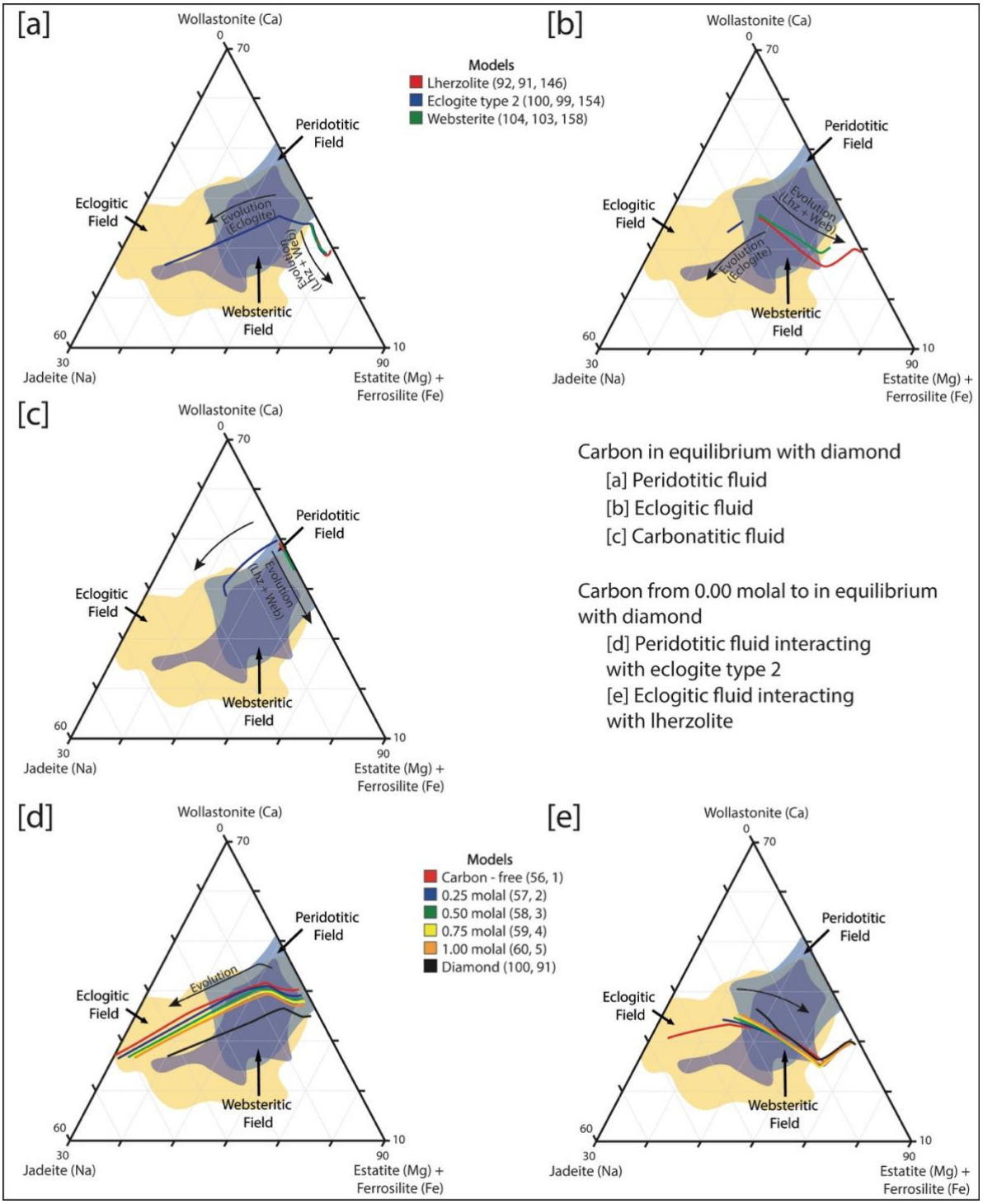

Figure B.3 - Geochemistry of garnet and clinopyroxene precipitated during progressive fluid-rock interaction for peridotitic fluid + eclogite (a, b), eclogitic fluid + lherzolite (c, d) at 5 GPa, 1000 ºC, and logfO_2 = -2 to -4 ΔFMQ. The initial amount of carbon in the fluids is in equilibrium with diamond (diamond-forming fluids). The numbers in parentheses refer to the model run number.

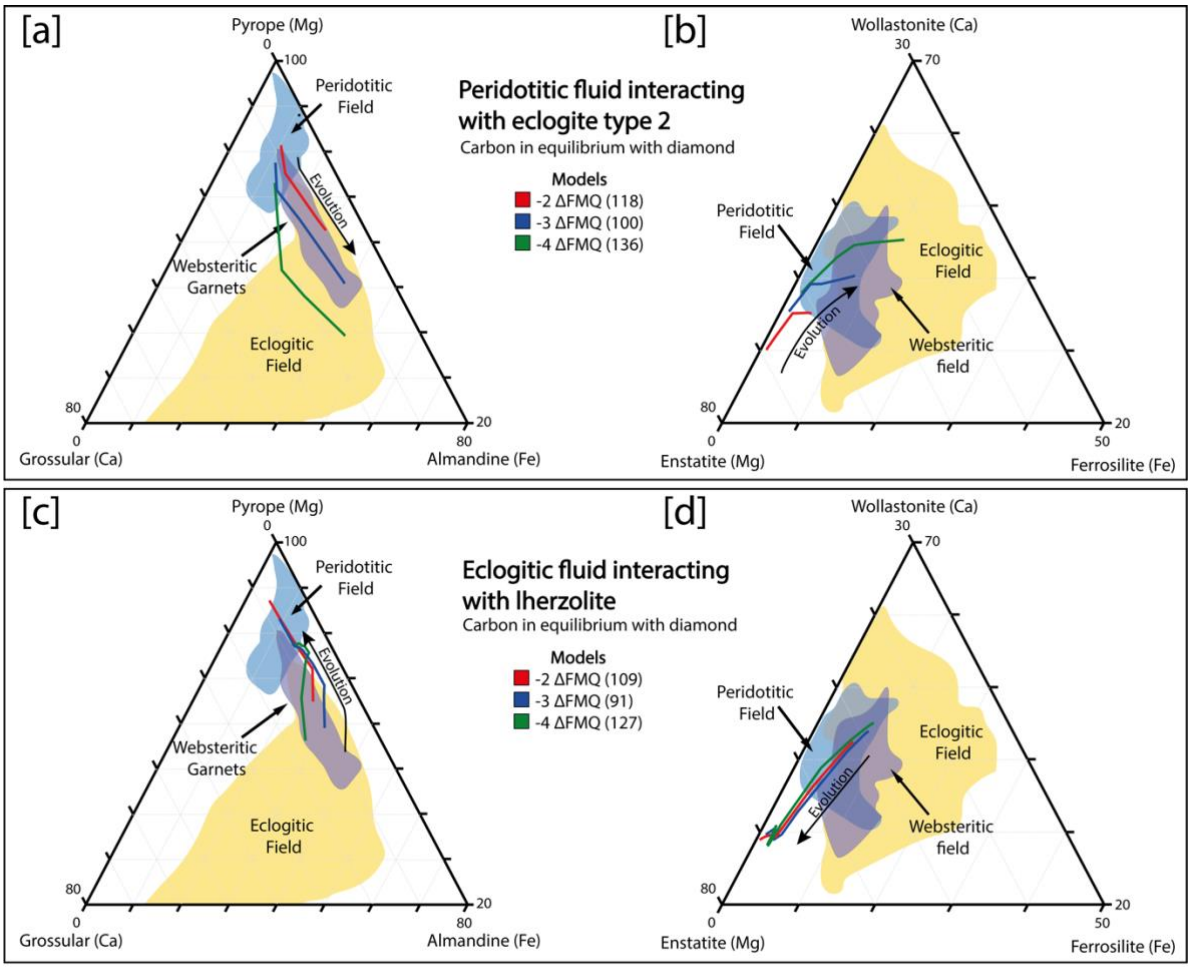

APPENDIX C

SUPPLEMENTARY MATERIAL FOR CHAPTER 4

Table C.1 - Composition of mineral assemblages and model parameters for eclogitic, peridotitic and carbonatitic fluids. This table is reproduced from Chapter 2 (Paragraph 2.3.1).

	Eclogitic	**Peridotitic**	**Carbonatitic**
Variable	**Set with**	**Set with**	**Set with**
K	-	Phlogopite	Fixed
Na	Fixed	Fixed	Fixed
Ca	Diopside (0.350)	Grossular (0.100)	Calcite (0.500)
Mg	Pyrope (0.352)	Forsterite (0.920)	Magnesite (0.450)
Fe	Almandine (0.323)	Fayalite (0.080)	Fayalite (0.080)
Al	Grossular (0.326)	Pyrope (0.800)	Grossular (0.300)
Si	Coesite	Clinoenstatite (0.955)	Forsterite (0.920)
Cl		Fixed	Fixed
C	Fixed/Diamond	Fixed/Diamond	Diamond
pH	Jadeite (0.539)	Jadeite (0.015)	Fixed
fO_2	Fixed	Fixed	Fixed

Table C.2 - The initial composition (molality concentration [moles/kg H_2O]) for eclogitic, peridotitic and carbonatitic diamond-forming fluids and control parameters at 5 GPa, 1000 ºC, and logfO_2 = -2 and -4 ΔFMQ.

	ECLOGITIC		**PERIDOTITIC**		**CARBONATITIC**
	Diamond forming		**Diamond forming**		**Diamond forming**
Name	E_diamond	E_diamond	P_diamond	P_diamond	C_diamond
C	18.73	8.47	27.77	8.07	30.56
K	0.00	0.00	1.48	2.62	0.50
Na	1.94	1.04	2.00	2.00	0.50
Ca	0.98	0.68	1.12	0.91	8.40
Mg	2.34	0.06	9.32	0.50	2.48
Fe	0.42	0.11	0.75	1.57	0.48
Al	1.65	1.11	0.19	0.09	0.06
Si	9.19	9.14	10.63	2.26	3.11
Cl	0.00	0.00	8.00	8.00	1.00
pH	4.87	4.56	5.15	4.59	4.49
***f*O$_2$ (log)**	-9.4	-11.4	-9.4	-11.4	-9.4
P (GPa)	5		5		5
T (^{o}C)	1000		1000		1000

Table C.3 - Final mineralogy after fluid-rock interaction for all the models. Temperature and pressure are fixed respectively at 5 GPa, 1000 ºC, and logfO_2 = -3 ΔFMQ. The initial rock composition is reported in Table 2. ΔfO_2 expresses changes in the redox conditions of the fluid after the metasomatic interaction.

Mei: Meionite, Cpx: Clinopyroxene, Grt: Garnet, Opx: Orthopyroxene, Mag: Magnetite, Ol: Olivine, Dia: Diamond, Dol: Dolomite, Bru: Brucite, Coe: Coesite

PARAMETERS					METASOMATIC MINERAL COMPOSITION (vol. %)											
Model	**Initial rock**	**Fluid**	**ΔFMQ**	**ΔlogfO_2**	**Ky**	**Grt**	**Cpx**	**Opx**	**MaHe**	**Mei**	**Coe**	**Ol**	**Dia**	**Dol**	**Bru**	**Final Rock**
91	Lhz	Ecl	-3	-0.1		6.5	16.8	75.2	1.4			0.1				Web
92	Lhz	Per	-3	0.1		10.5	34.0	55.2	0.3							Web
93	Dun	Ecl	-3	-0.1		8.5	7.0	82.9	1.5			0.1				Web
94	Dun	Per	-3	0.1		17.7	22.3	59.9				0.2				Web
95	Harz	Ecl	-3	-0.1		7.9	2.0	88.6	1.4			0.1				Orthopx
96	Harz	Per	-3	0.1		19.2	5.5	75.2				0.2				Orthopx
97	Ecl T1	Ecl	-3	0.0		0.7	35.2			50.8	13.3					Ecl
98	Ecl T1	Per	-3	0.2		30.2	55.1			14.0	0.3		0.5			Ecl
99	Ecl T2	Ecl	-3	0.0		0.5	32.2			49.2	18.1					Ecl
100	Ecl T2	Per	-3	0.2		15.9	59.1			24.4	0.3		0.4			Ecl
101	Ecl T3	Ecl	-3	0.0		0.2	50.1			49.7						Clinopx
102	Ecl T3	Per	-3	0.1		1.3	97.4						1.3			Clinopx
103	Web	Ecl	-3	-0.1		13.3	57.0	29.7								Web
104	Web	Per	-3	0.1		15.2	58.3	25.1	1.4							Web
105	Orthopx	Ecl	-3	-0.1		37.9	36.0	26.2								Web
106	Orthopx	Per	-3	0.1		35.7	28.0	36.3								Web
107	Clinopx	Ecl	-3	-0.1		17.5	82.5									Clinopx

108	Clinopx	Per	-3	0.1		28.6	71.4									Clinopx
109	Lhz	Ecl	-2	0.1		8.3	19.7	69.3	2.7			0.1				Web
110	Lhz	Per	-2	0.1		10.5	23.1	64.1	2.2			0.1				Web
111	Dun	Ecl	-2	0.1		12.9	6.9	76.7	3.5			0.1				Orthopx
112	Dun	Per	-2	0.1		19.5		77.6	2.8			0.2				Orthopx
113	Harz	Ecl	-2	0.1		11.0		85.7	3.2			0.1				Orthopx
114	Harz	Per	-2	0.1		26.9		70.6	2.4			0.2				Orthopx
115	Ecl T1	Ecl	-2	-0.1		21.1	0.5		1.9	37.1	39.4					Ecl
116	Ecl T1	Per	-2	0.1		32.2	43.5			23.1	0.3		0.9			Ecl
117	Ecl T2	Ecl	-2	-0.1		0.3	7.6		5.0	50.7	36.2		0.1			Ecl
118	Ecl T2	Per	-2	0.1		15.8	48.4		0.4	34.4	0.4		0.7			Ecl
119	Ecl T3	Ecl	-2	-0.2			34.3		4.3	61.2			0.2			Clinopx
120	Ecl T3	Per	-2	0.0		1.5	97.4						1.1			Clinopx
121	Web	Ecl	-2	0.0		9.4	75.3	11.0	4.3							Web
122	Web	Per	-2	0.0		16.1	50.2	30.0	3.7				0.1			Web
123	Orthopx	Ecl	-2	0.0		41.6	49.5	0.9	8.0							Orthopx
124	Orthopx	Per	-2	0.0		38.5		58.1	3.4							Orthopx
125	Clinopx	Ecl	-2	0.0		1.6	78.4		2.5	17.6						Clinopx
126	Clinopx	Per	-2	0.1		29.2	70.0		0.7	0.1						Clinopx
127	Lhz	Ecl	-4	-0.1		7.7	19.3	72.9	0.0			0.1				Web
128	Lhz	Per	-4	0.0		12.4	40.9	46.6				0.1				Web
129	Dun	Ecl	-4	-0.1		10.5	9.8	79.6				0.1				Web
130	Dun	Per	-4	0.0		18.2	36.3	45.4				0.1				Web
131	Harz	Ecl	-4	-0.1		9.6	3.9	86.5				0.1				Web
132	Harz	Per	-4	0.0		21.1	19.8	58.9				0.2				Web
133	Ecl T1	Ecl	-4	0.0		9.9	60.7			29.5						Clinopx
134	Ecl T1	Per	-4	0.0		38.5	54.7			6.3			0.6			Clinopx
135	Ecl T2	Ecl	-4	0.0		1.4	48.6			41.3	8.7					Clinopx
136	Ecl T2	Per	-4	0.0		20.7	60.9			17.9	0.3		0.2			Clinopx

137	Ecl T3	Ecl	-4	-0.1		0.5	52.4			47.1						Clinopx
138	Ecl T3	Per	-4	0.0		1.4	95.9						2.7			Clinopx
139	Web	Ecl	-4	-0.1		16.0	55.3	28.7								Web
140	Web	Per	-4	0.0		15.6	60.1	23.6	0.7							Web
141	Orthopx	Ecl	-4	-0.1		42.6	33.2	24.2								Web
142	Orthopx	Per	-4	0.0		35.1	35.8	29.1								Web
143	Clinopx	Ecl	-4	0.0		19.8	80.2									Clinopx
144	Clinopx	Per	-4	0.0		29.9	70.1									Clinopx
145	Lhz	Carb	-2	0.1			54.2		2.2	6.1		35.2	1.2	1.2		Wehr
146	Lhz	Carb	-3	0.3			49.2		2.1	7.1		40.2	1.5			Wehr
147	Dun	Carb	-2	0.0			49.3		2.1	11.9		0.5	2.2	34.0		Ecl
148	Dun	Carb	-3	0.3		12.5	46.3		2.3			1.3	2.1		35.6	Ecl
149	Harz	Carb	-2	0.0			38.9		2.5	7.5		38.9	1.6	10.7		Wehr
150	Harz	Carb	-3	0.3		11.5	34.0		2.4			44.1	1.8		6.2	Wehr
151	Ecl T1	Carb	-2	0.1			46.9		3.3	40.5	7.9		1.5			Clinopx
152	Ecl T1	Carb	-3	0.5			58.1		2.3	37.7			1.9			Clinopx
153	Ecl T2	Carb	-2	0.0			31.0		5.3	47.4	15.1		1.1			Clinopx
154	Ecl T2	Carb	-3	0.4			46.9		4.0	44.6	3.1		1.5			Clinopx
155	Ecl T3	Carb	-2	-0.1			28.7		4.1	66.3			0.8			Clinopx
156	Ecl T3	Carb	-3	0.1		96.1	0.1		1.0				2.9			Clinopx
157	Web	Carb	-2	0.1		4.6	80.5		5.1			8.7	1.2			Wehr
158	Web	Carb	-3	0.5		5.3	71.8		4.5			16.9	1.6			Wehr
159	Orthopx	Carb	-2	0.1		4.1	67.3		4.0			23.0	1.6			Wehr
160	Orthopx	Carb	-3	0.6		5.0	58.6		3.3			31.1	2.0			Wehr
161	Clinopx	Carb	-2	0.0			58.6		2.6	26.7		0.3	1.1	10.7		Ecl
162	Clinopx	Carb	-3	0.2		36.1	50.7		1.9				1.4		9.8	Ecl

Figure C.1 - Model results for the evolution of the metasomatic interaction between different fluids (eclogitic, peridotitic, and carbonatitic) and a lherzolite at 5 GPa, 1000 ºC, and logfO_2 = -2 ΔFMQ (a, b, c) and logfO_2 = -4 ΔFMQ (c, d). The detailed parameters of each model are listed in Table C.2 and Table C.3. [Mei: Meionite, Cpx: Clinopyroxene, Grt: Garnet, Opx: Orthopyroxene, Mag: Magnetite, Ol: Olivine, Dia: Diamond].

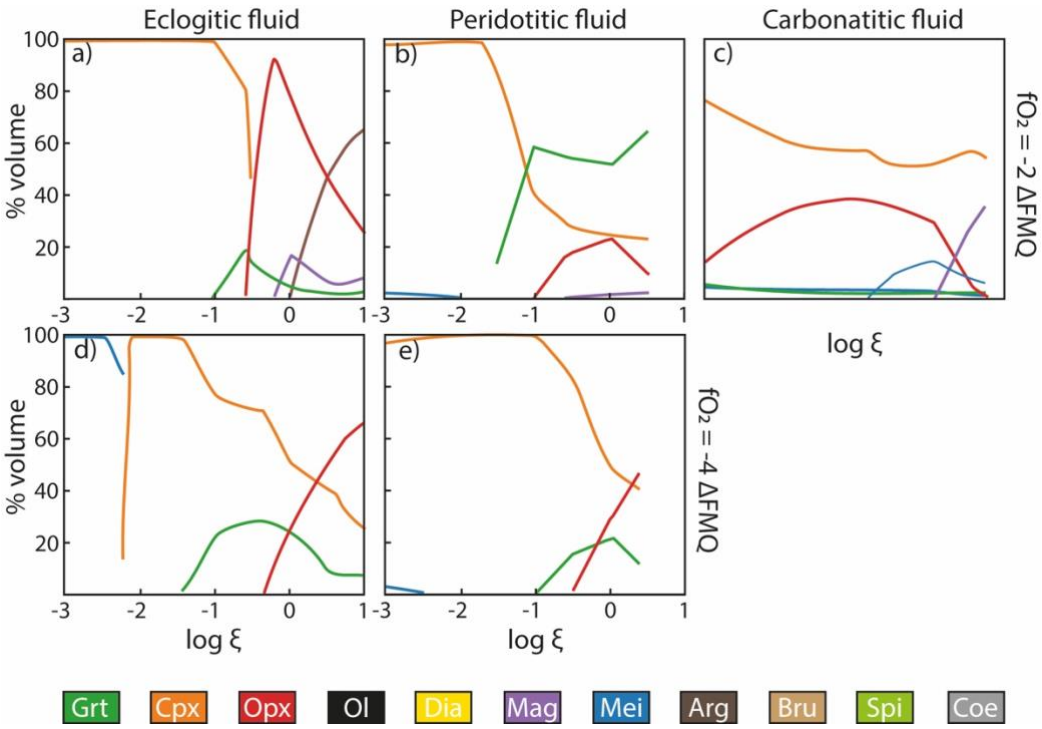

APPENDIX D

SUPPLEMENTARY MATERIAL FOR CHAPTER 5

Table D.1 - Chemical composition (molality concentration [moles/kg H_2O]) for selected peridotitic fluids at 0.5 GPa, between 300 and 800 ºC, and logfO_2 = 0 ΔFMQ. This table is reproduced from Chapter 2 (Paragraph 2.3.1).

mol/Kg	**Equilibrium with**	**300 ºC**	**400 ºC**	**500 ºC**	**600 ºC**	**700 ºC**	**800 ºC**
Na	Fixed	0.50	0.50	0.50	0.50	0.50	0.50
K	Fixed	0.50	0.50	0.50	0.50	0.50	0.50
Ca	Diopside (0.26)	$0.22x10^{-5}$	0.85×10^{-5}	0.22×10^{-4}	0.59×10^{-4}	0.15×10^{-4}	$0.30x\ 10^{-3}$
Mg	Forsterite (0.65)	0.17	0.28	0.32	0.30	0.25	0.19
Fe	Fayalite (0.35)	$0.34x10^{-4}$	$0.18x10^{-3}$	$0.38x10^{-3}$	$0.37x10^{-3}$	$0.41x10^{-3}$	$0.47x10^{-3}$
Si	Enstatite (0.41)	0.06	0.01	0.16	0.24	0.28	0.30
Al	Spinel	0.14	0.15	0.21	0.26	0.27	0.26
C	Fixed	0.50	0.50	0.50	0.50	0.50	0.50
Cl	Fixed	0.50	0.50	0.50	0.50	0.50	0.50
pH	Charge balance	8.08	7.58	7.38	7.30	7.27	7.32
fO_2		-35.45	-28.72	-23.81	-20.07	-17.13	-14.75
ΔFMQ		0	0	0	0	0	0

Table D.2 - Final mineralogy after fluid-rock interaction for selected models after fluid metasomatism at 0.5 GPa, 400 and 800 ºC, and logfO_2 = 0 and -1 ΔFMQ. Ant (antigorite); bio (biotite); dol (dolomite); chl (chlorite); cpx (clinopyroxene); grt (garnet); mag (magnetite); ol (olivine); opx (orthopyroxene); par (paragonite); pl (plagioclase); talc (talc); trem (tremolite).

PARAMETERS					**MINERAL COMPOSITION (vol. %)**
Model	**Initial Rock**	**Temp (ºC)**	**F/R ratio**	**FMQ**	
2	Lhz	400	1.85	0	trem (14.03), ant (21.90), talc (19.19), ol (43.41), bio (1.47)
6	Lhz	800	1.85	0	ol (34.43), bio (16.27), cpx (48.97), opx (0.33)
8	Dun	400	1.85	0	mag (18.93), ant (72.30), ol (0.30), bio (2.72), cpx (5.75)
12	Dun	800	1.85	0	mag (19.17), ol (9.37), bio (50.68), cpx (20.78)
14	Clinopx	400	1.85	0	mag (16.18), ol (0.31), bio (30.14), cpx (46.95), chl (6.42)
18	Clinopx	800	1.85	0	mag (18.34), ol (0.27), bio (33.52), cpx (39.64), pl (8.23)
20	Orthopx	400	1.85	0	mag (2.88), talc (57.52), ol (38.78), bio (0.82)
24	Orthopx	800	1.85	0	ol (89.86), bio (10.02), opx (0.12)
26	Gab	400	1.85	0	bio (14.43), cpx (40.68), chl (21.39), grt (6.14), pl (2.85), dol (1.12), par (13.39)
30	Gab	800	1.85	0	mag (19.44), bio (27.60), cpx (20.31), pl (32.65)
62	Lhz	400	1.85	-2	trem (14.03), ant (21.51), talc (18.99), ol (43.14), bio (2.33)
66	Lhz	800	1.85	-2	ol (34.42), bio (16.30). cpx (48.96), opx (0.32)
68	Dun	400	1.85	-2	mag (20.19), ol (23.24), bio (35.61), cpx (20.96)
72	Dun	800	1.85	-2	mag (13.33), ol (22.65), bio (46.25), cpx (17.77)
74	Clinopx	400	1.85	-2	mag (14.88), ol (0.05), bio (33.02), cpx (39.20), chl (12.85),
78	Clinopx	800	1.85	-2	mag (6.35), ol (9.97), bio (58.89), cpx (0.04), grt (24.75)
80	Orthopx	400	1.85	-2	mag (0.21), talc (50.84), ol (47.57), bio (1.38)
84	Orthopx	800	1.85	-2	ol (89.85), bio (10.03), opx (0.12),
86	Gab	400	1.85	-2	bio (13.25), cpx (42.37), chl (19.76), grt (7.63), pl (2.07), par (14.92)
90	Gab	800	1.85	-2	ol (47.07), bio (26.68), cpx (0.56), grt (25.66), pl (0.03)
121	Lhz	600	1.85	0	ol (31.93), bio (21.67), cpx (46.09), opx (0.31)

122	Lhz	600	1.85	0	ol (31.93), bio (21.67), cpx (46.09), opx (0.31)
123	Lhz	600	1.85	0	ol (31.93), bio (21.67), cpx (46.09), opx (0.31)
124	Lhz	600	1.85	0	ol (31.93), bio (21.67), cpx (46.09), opx (0.31)

Table D.3 - Distribution of carbon into mineral and aqueous species (mol. %) in the system after fluid-rock interaction at 0.5 GPa, between 300 and 800 ºC, and logfO_2 = 0 to -3 ΔFMQ. The molality (moles/kg) of carbon in the system varies from 0.1 to 2.0.

PARAMETERS						**CARBON SPECIATION (mol %)**						
Models	**Initial Rock**	**Temperature (ºC)**	**FMQ**	**Carbon (moles)**	**ΔfO_2**	**CH_4**	**CO_2**	**HCO_3^-**	**H_2CO_3**	**$NaHCO_3$**	**Graphite**	**Calcite**
1	Lhz	300	0	0.5	-0.74	0.97		0.01				
2	Lhz	400	0	0.5	-0.02	0.57	0.05	0.16	0.01	0.15		
3	Lhz	500	0	0.5	0	0.25	0.37	0.08	0.09	0.17		
4	Lhz	600	0	0.5	0	0.06	0.62	0.01	0.23	0.06		
5	Lhz	700	0	0.5	-0.01	0.02	0.63		0.32	0.01		
6	Lhz	800	0	0.5	0		0.56		0.38			
7	Dun	300	0	0.5	-5.59	1.00						
8	Dun	400	0	0.5	-1.76	1.00						
9	Dun	500	0	0.5	0.03	0.23	0.39	0.08	0.10	0.17		
10	Dun	600	0	0.5	0.05	0.05	0.63	0.01	0.23	0.07		
11	Dun	700	0	0.5	0.03	0.01	0.63		0.32	0.01		
12	Dun	800	0	0.5	0.02		0.56		0.38			
13	Clinopx	300	0	0.5	-0.65	0.99			0.00			
14	Clinopx	400	0	0.5	0.25	0.65	0.18	0.05	0.03	0.07		
15	Clinopx	500	0	0.5	0	0.34	0.49	0.01	0.12	0.03		
16	Clinopx	600	0	0.5	-0.12	0.11	0.63		0.23	0.01		
17	Clinopx	700	0	0.5	-0.1	0.02	0.63		0.32			
18	Clinopx	800	0	0.5	-0.02	0.01	0.56		0.38			
19	Orthopx	300	0	0.5	-0.74	0.97		0.01				
20	Orthopx	400	0	0.5	0.15	0.44	0.08	0.21	0.01	0.18		

21	Orthopx	500	0	0.5	1.17		0.54	0.09	0.14	0.21		
22	Orthopx	600	0	0.5	1.64		0.67	0.01	0.25	0.07		
23	Orthopx	700	0	0.5	1.58		0.65		0.33	0.01		
24	Orthopx	800	0	0.5	0.29		0.57		0.38			
25	Gab	300	0	0.5	1.14	0.12	0.03				0.30	0.52
26	Gab	400	0	0.5	0.78	0.12	0.40	0.04	0.07	0.05		
27	Gab	500	0	0.5	0.1	0.24	0.55	0.02	0.14	0.05		
28	Gab	600	0	0.5	0.03	0.06	0.66		0.24	0.02		
29	Gab	700	0	0.5	-0.01	0.02	0.63		0.32	0.01		
30	Gab	800	0	0.5	0		0.56		0.38			
31	Lhz	300	-1	0.5	-0.04	0.99						
32	Lhz	400	-1	0.5	-0.04	0.99						
33	Lhz	500	-1	0.5	-0.02	0.96	0.01			0.01		
34	Lhz	600	-1	0.5	0	0.86	0.09		0.03	0.01		
35	Lhz	700	-1	0.5	0	0.60	0.25		0.12	0.01		
36	Lhz	800	-1	0.5	0	0.30	0.36		0.24			
37	Dun	300	-1	0.5	-0.65	1.00						
38	Dun	400	-1	0.5	0.18	0.97		0.01		0.01		
39	Dun	500	-1	0.5	0.09	0.95	0.02	0.01	0.01	0.02		
40	Dun	600	-1	0.5	0.03	0.84	0.10		0.04	0.01		
41	Dun	700	-1	0.5	0.02	0.58	0.26		0.13	0.01		
42	Dun	800	-1	0.5	0.01	0.28	0.37		0.25			
43	Clinopx	300	-1	0.5	-0.14	1.00						
44	Clinopx	400	-1	0.5	-0.26	1.00						
45	Clinopx	500	-1	0.5	-0.08	0.98	0.01					
46	Clinopx	600	-1	0.5	0.01	0.87	0.09		0.03			
47	Clinopx	700	-1	0.5	0.01	0.59	0.25		0.13			

48	Clinopx	800	-1	0.5	0.01	0.29	0.37		0.24			
49	Orthopx	300	-1	0.5	0.26	0.97	0.00	0.01				
50	Orthopx	400	-1	0.5	1.13	0.52	0.08	0.17	0.01	0.16		
51	Orthopx	500	-1	0.5	0.79	0.47	0.27	0.05	0.07	0.12		
52	Orthopx	600	-1	0.5	0.43	0.47	0.35	0.01	0.13	0.04		
53	Orthopx	700	-1	0.5	0.2	0.38	0.38		0.19	0.01		
54	Orthopx	800	-1	0.5	0.08	0.22	0.40		0.27			
55	Gab	300	-1	0.5	2.09	0.14	0.03				0.81	
56	Gab	400	-1	0.5	1.42	0.54	0.32	0.03	0.05	0.04		
57	Gab	500	-1	0.5	0.24	0.94	0.04		0.01	0.01		
58	Gab	600	-1	0.5	0.05	0.84	0.11		0.04			
59	Gab	700	-1	0.5	0.02	0.58	0.26		0.13			
60	Gab	800	-1	0.5	0.01	0.29	0.36		0.24			
61	Lhz	300	-2	0.5	-0.13	1.00						
62	Lhz	400	-2	0.5	-0.09	1.00						
63	Lhz	500	-2	0.5	-0.03	1.00						
64	Lhz	600	-2	0.5	0	1.00						
65	Lhz	700	-2	0.5	0	0.99						
66	Lhz	800	-2	0.5	0	0.97	0.01		0.01			
67	Dun	300	-2	0.5	-0.09	1.00						
68	Dun	400	-2	0.5	0.56	1.00						
69	Dun	500	-2	0.5	0.11	1.00						
70	Dun	600	-2	0.5	0.03	1.00						
71	Dun	700	-2	0.5	0.01	0.99						
72	Dun	800	-2	0.5	0.01	0.97	0.01		0.01			
73	Clinopx	300	-2	0.5	0.4	1.00						
74	Clinopx	400	-2	0.5	0.07	1.00						

75	Clinopx	500	-2	0.5	0.02	1.00						
76	Clinopx	600	-2	0.5	0.04	1.00						
77	Clinopx	700	-2	0.5	0.01	0.99						
78	Clinopx	800	-2	0.5	0.02	0.97	0.01		0.01			
79	Orthopx	300	-2	0.5	1.13	0.97		0.01				
80	Orthopx	400	-2	0.5	2.06	0.52	0.08	0.17	0.01	0.16		
81	Orthopx	500	-2	0.5	1.55	0.68	0.15	0.03	0.04	0.08		
82	Orthopx	600	-2	0.5	0.45	0.99	0.01					
83	Orthopx	700	-2	0.5	0.11	1.00						
84	Orthopx	800	-2	0.5	0.04	0.96	0.01		0.01			
85	Gab	300	-2	0.5	2.91	0.16	0.02				0.79	
86	Gab	400	-2	0.5	2.3	0.59	0.28	0.03	0.05	0.03		
87	Gab	500	-2	0.5	0.55	1.00						
88	Gab	600	-2	0.5	0.3	0.99						
89	Gab	700	-2	0.5	0.08	0.99	0.01					
90	Gab	800	-2	0.5	0.03	0.97	0.01		0.01			
91	Lhz	300	-3	0.5	-0.14	1.00						
92	Lhz	400	-3	0.5	-0.09	1.00						
93	Lhz	500	-3	0.5	-0.03	1.00						
94	Lhz	600	-3	0.5	0	1.00						
95	Lhz	700	-3	0.5	0	1.00						
96	Lhz	800	-3	0.5	0	1.00						
97	Dun	300	-3	0.5	0.38	1.00						
98	Dun	400	-3	0.5	0.26	1.00						
99	Dun	500	-3	0.5	0.05	1.00						
100	Dun	600	-3	0.5	0.01	1.00						
101	Dun	700	-3	0.5	0	1.00						

102	Dun	800	-3	0.5	0.01	1.00						
103	Clinopx	300	-3	0.5	2.12	0.97		0.01				
104	Clinopx	400	-3	0.5	2.96	0.60	0.06	0.14	0.01	0.14		
105	Clinopx	500	-3	0.5	0.77	1.00						
106	Clinopx	600	-3	0.5	0.13	1.00						
107	Clinopx	700	-3	0.5	0.04	1.00						
108	Clinopx	800	-3	0.5	0.03	1.00						
109	Orthopx	300	-3	0.5	2.12	0.97		0.01				
110	Orthopx	400	-3	0.5	2.96	0.60	0.06	0.14	0.01	0.14		
111	Orthopx	500	-3	0.5	0.77	1.00						
112	Orthopx	600	-3	0.5	0.13	1.00						
113	Orthopx	700	-3	0.5	0.04	1.00						
114	Orthopx	800	-3	0.5	0.03	1.00						
115	Gab	300	-3	0.5	3.84	0.18	0.02				0.78	
116	Gab	400	-3	0.5	3.2	0.70	0.21	0.02	0.03	0.02		
117	Gab	500	-3	0.5	0.61	1.00						
118	Gab	600	-3	0.5	0.1	1.00						
119	Gab	700	-3	0.5	0.03	1.00						
120	Gab	800	-3	0.5	0.02	1.00						
121	Lhz	600	-2	0.1	0	1.00						
122	Lhz	600	-2	1	0	1.00						
123	Lhz	600	-2	1.5	0	1.00						
124	Lhz	600	-2	2	0	1.00						
125	Dun	600	-2	0.1	0.03	1.00						
126	Dunite	600	-2	1	0.03	1.00						
127	Dunite	600	-2	1.5	0.03	1.00						
128	Dunite	600	-2	2	0.03	1.00						

129	Clinopx	600	-2	0.1	0.04	1.00						
130	Clinopx	600	-2	1	0.04	1.00						
131	Clinopx	600	-2	1.5	0.04	1.00						
132	Clinopx	600	-2	2	0.04	1.00						
133	Orthopx	600	-2	0.1	0.46	0.99	0.01					
134	Orthopx	600	-2	1	0.44	0.99	0.01					
135	Orthopx	600	-2	1.5	0.43	0.99	0.01					
136	Orthopx	600	-2	2	0.42	0.99	0.01					
137	Gab	600	-2	0.1	0.31	0.99						
138	Gab	600	-2	1	0.3	0.99						
139	Gab	600	-2	1.5	0.3	0.99						
140	Gab	600	-2	2	0.3	0.99						

Figure D.1 - Methane content after the interaction between a peridotitic fluid and different lithologies at 0.5 GPa, between 300 and 800 ºC, and logfO_2 = -3 to 0 ΔFMQ. The oxygen fugacity mitigates the influence of lithologies in methanogenesis. Methane metastability is reported as a grey field (Manning et al., 2013).

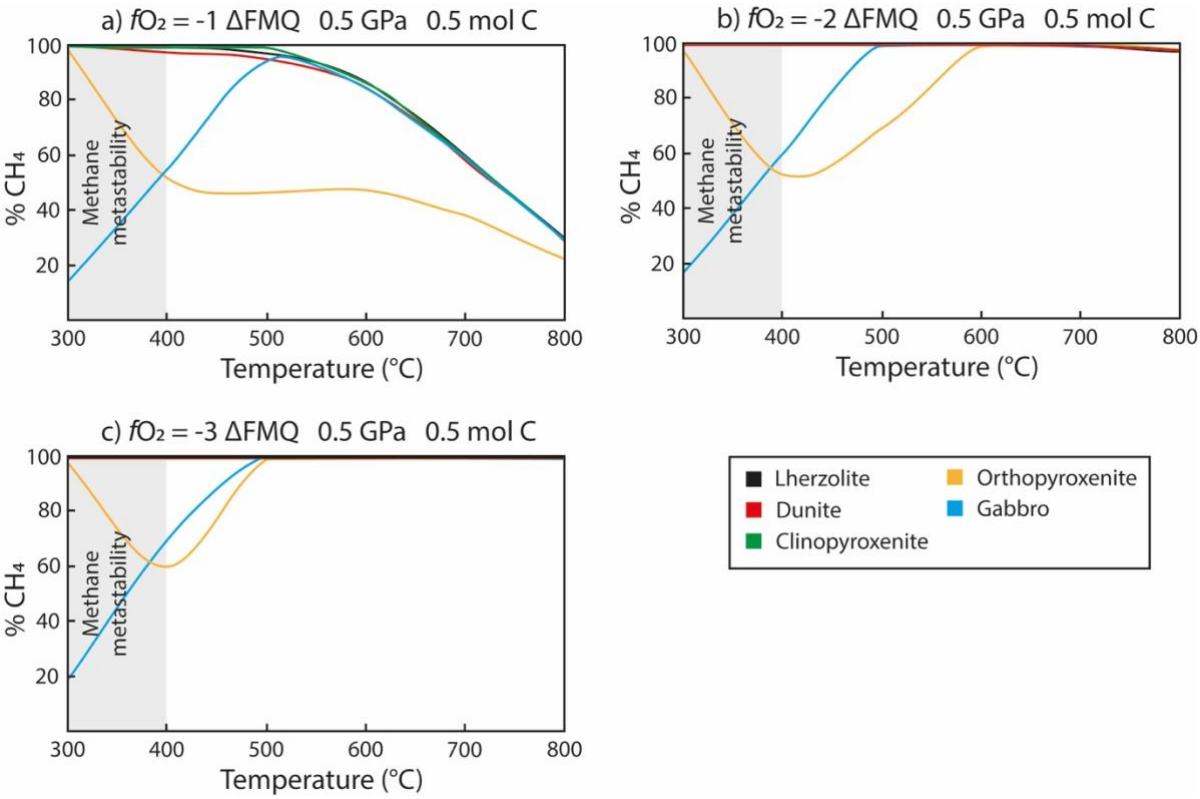

Figure D.2 - Carbon speciation after the interaction between a peridotitic fluid and a lherzolite at 0.5 GPa, between 300 and 800 ºC, and logfO_2 = -3 to 0 ΔFMQ. The amount of methane increases as the oxygen fugacity decreases. Methane metastability is reported as a grey field (Manning et al., 2013).

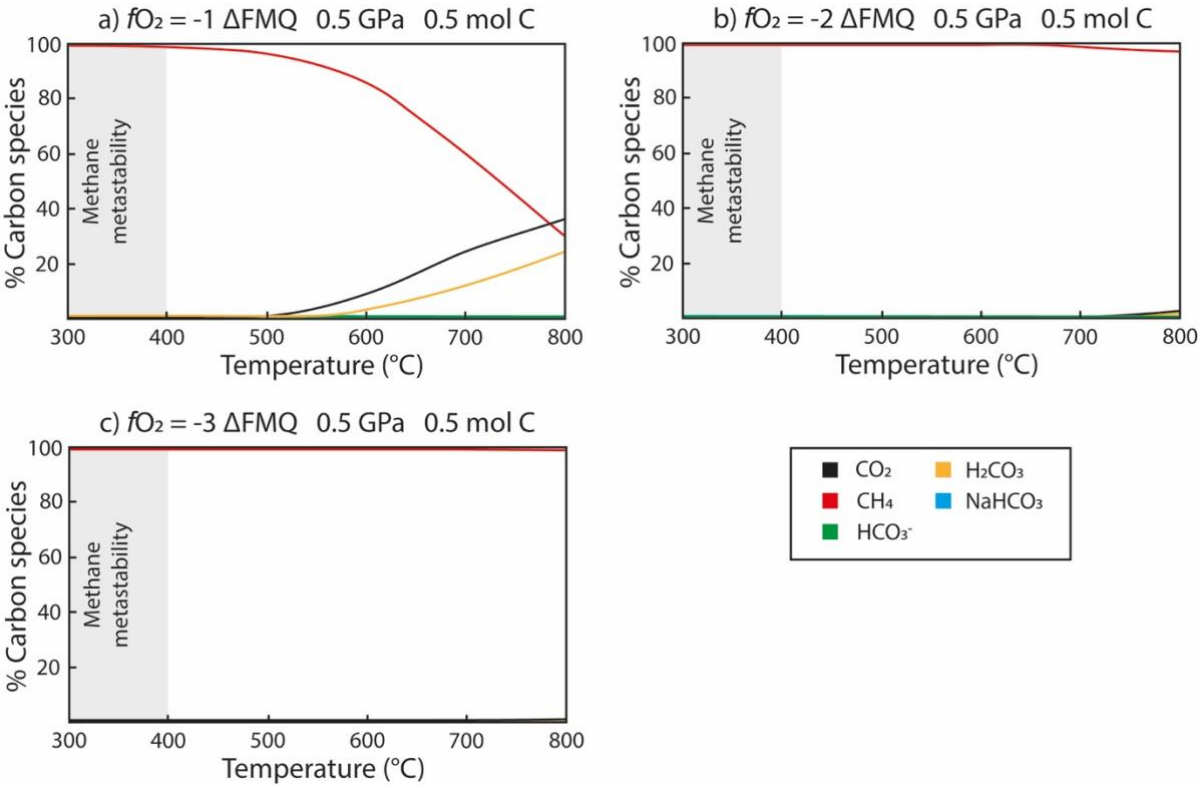

Figure D.3 - Carbon speciation after the interaction between a peridotitic fluid and different rocks at 0.5 GPa, 500 ºC, and logfO_2 = -3 to 0 ΔFMQ. The oxygen fugacity mitigates the influence of lithologies in methanogenesis. Methane metastability is reported as a grey field (Manning et al., 2013).

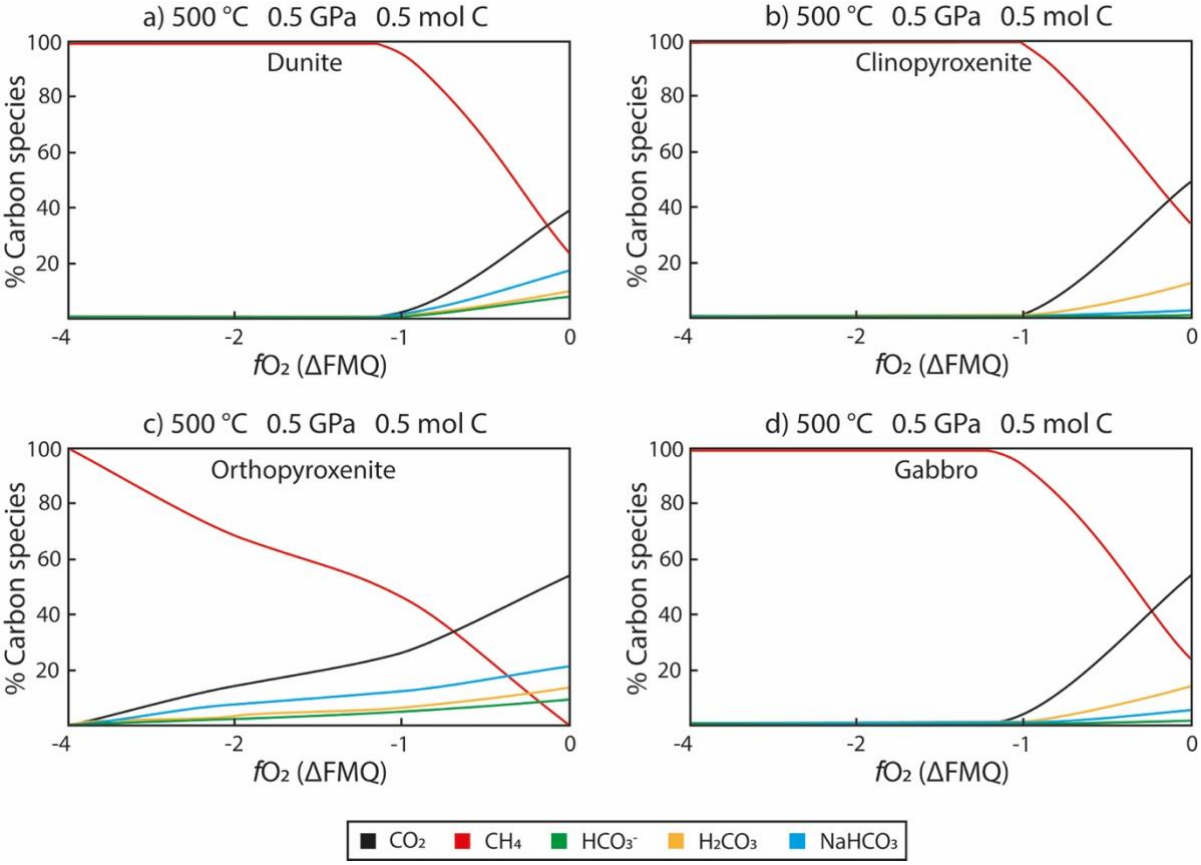

LIST OF FIGURES

LIST OF TABLES

REFERENCES

Ammannati E, Jacob DE, Avanzinelli R, Foley SF, Conticelli S (2016) - Low Ni olivine in silica-undersaturated ultrapotassic igneous rocks as evidence for carbonate metasomatism in the mantle. Earth and Planetary Science Letters, 444, pp 64–74.

Anderson G (2017) - Thermodynamics of Natural Systems: Theory and Applications in Geochemistry and Environmental Science. Thermodynamics of Natural Systems.

Arzilli F, Burton M, La Spina G, Macpherson CG, van Keken PE, McCann J (2023) - Decarbonation of subducting carbonate-bearing sediments and basalts of altered oceanic crust: Insights into recycling of CO2 through volcanic arcs. Earth and Planetary Science Letters, 602.

Aulbach S, Stachel T, Viljoen KS, Brey GP, Harris JW (2002) - Eclogitic and websteritic diamond sources beneath the Limpopo Belt - Is slab-melting the link? Contributions to Mineralogy and Petrology, 143, pp 56–70.

Aulbach S, Stachel T, Creaser RA, Heaman LM, Shirey SB, Muehlenbachs K, Eichenberg D, Harris JW (2008) - Sulfide survival and diamond genesis during formation and evolution of Archaean subcontinental lithosphere: Slave vs Kaapvaal. International Kimberlite Conference: Extended Abstracts, 9.

Auzende A-L, Pellenq RJ-M, Devouard B, Baronnet A, Grauby O (2006) - Atomistic calculations of structural and elastic properties of serpentine minerals: the case of lizardite. Physics and Chemistry of Minerals, 33, pp 266–275.

Azevedo-Vannson S, France L, Ingrin J, Chazot G (2021) - Mantle metasomatic influence on water contents in continental lithosphere: New constraints from garnet pyroxenite xenoliths (France & Cameroon volcanic provinces). Chemical Geology, 575.

Azuma S, Katayama I (2017) - Evolution of the rheological structure. Earth, Planets and Space, 69, pp 1–13.

Bale CW, Bélisle E, Chartrand P, Decterov SA, Eriksson G, Gheribi AE, Hack K, Jung IH, Kang YB, Melançon J, PeltoN AD, Petersen S, Robelin C, Sangster J, Spencer P, Van Ende MA (2016) - FactSage thermochemical software and databases, 2010–2016. Caphad, 54, pp 35-53.

Baker VR, Strom RG, Gulick VC, Kargel JS, Komatsu G, Kale VS (1991) - Ancient oceans, ice sheets and the hydrological cycle on Mars. Nature, 352, pp 589–594.

Basch V, Rampone E, Borghini G, Ferrando C, Zanetti A (2019) - Origin of pyroxenites in the oceanic mantle and their implications on the reactive percolation of depleted melts. Contributions to Mineralogy and Petrology, 174.

Beck P, Barrat JA, Gillet P, et al (2006) - Petrography and geochemistry of the chassignite Northwest Africa 2737 (NWA 2737). Geochimica et Cosmochimica Acta, 70, pp 2127–2139.

Bénard A, Ionov DA (2013) - Melt– and Fluid–Rock Interaction in Supra-Subduction Lithospheric Mantle: Evidence from Andesite-hosted Veined Peridotite Xenoliths. Journal of Petrology, 54, pp 2339–2378.

Berman RG (1988) - Internally-Consistent Thermodynamic Data for Minerals in the System Na2O-K2O-CaO-MgO-FeO-Fe2O3-Al2O3-SiO2-TiO2-H2O-CO2. Journal of Petrology, 29, pp 445–522.

Blamey NJF, Parnell J, McMahon S, et al (2015) - Evidence for methane in Martian meteorites. Nature Communications 2015 6:1, 6, pp 1–7.

Bodinier JL, Godard M (2014) - Orogenic, Ophiolitic, and Abyssal Peridotites. Treatise on Geochemistry: Second Edition, 3, pp 103–167.

Borghini G, Rampone E, Zanetti A, Class C, Cipriani A, Hofmann AW, Goldstein SL (2016) - Pyroxenite Layers in the Northern Apennines' Upper Mantle (Italy)—Generation by Pyroxenite Melting and Melt Infiltration. Journal of Petrology, 57, pp 625–653.

Bouhifd MA, Whittington A, Roux J, Richet P (2006) - Effect of water on the heat capacity of polymerized aluminosilicate glasses and melts. Geochimica et Cosmochimica Acta, 70, pp 711–722.

Bowman EE, Ducea MN (2023) - Pyroxenite melting at subduction zones. Geology, 51, pp 383–386.

Bulanova GP, Walter MJ, Smith CB, Kohn SC, Armstrong LS, Blundy J, Gobbo L (2010) - Mineral inclusions in sublithospheric diamonds from Collier 4 kimberlite pipe, Juina, Brazil: Subducted protoliths, carbonated melts and primary kimberlite magmatism. Contributions to Mineralogy and Petrology, 160, pp 489–510.

Bureau H, Remusat L, Esteve I, Pinti DL, Cartigny P (2018) - The growth of lithospheric diamonds. Science Advances, 4.

Busigny V, Cartigny P, Philippot P (2011) - Nitrogen isotopes in ophiolitic metagabbros: A re-evaluation of modern nitrogen fluxes in subduction zones and implication for the early Earth atmosphere. Geochimica et Cosmochimica Acta, 75, pp 7502–7521.

Connolly JAD (2005) - Computation of phase equilibria by linear programming: A tool for geodynamic modeling and its application to subduction zone decarbonation. Earth and Planetary Science Letters, 236, pp 524–541.

Dalou C, Hirschmann MM, Jacobsen SD, Le Losq C (2019) - Raman spectroscopy study of C-O-H-N speciation in reduced basaltic glasses: Implications for reduced planetary mantles. Geochimica et Cosmochimica Acta, 265, pp 32–47.

Dasgupta R, Hirschmann MM, Stalker K (2006) - Immiscible Transition from Carbonate-rich to Silicate-rich Melts in the 3 GPa Melting Interval of Eclogite + CO2 and Genesis of Silica-undersaturated Ocean Island Lavas. Journal of Petrology, 47, pp 647–671.

Dasgupta R, Hirschmann MM, Smith ND (2007) - Partial Melting Experiments of Peridotite + CO2 at 3 GPa and Genesis of Alkalic Ocean Island Basalts. Journal of Petrology, 48, pp 2093–2124.

Dasgupta R, Hirschmann MM, McDonough WF, Spiegelman M, Withers AC (2009) - Trace element partitioning between garnet lherzolite and carbonatite at 6.6 and 8.6 GPa with applications to the geochemistry of the mantle and of mantle-derived melts. Chemical Geology, 262, pp 57–77.

Dasgupta R, Hirschmann MM (2010) - The deep carbon cycle and melting in Earth's interior. Earth and Planetary Science Letters, 298, pp 1–13.

De Stefano A, Kopylova MG, Cartigny P, Afanasiev V (2009) - Diamonds and eclogites of the Jericho kimberlite (Northern Canada). Contributions to Mineralogy and Petrology, 158, pp 295–315.

Deep Carbon Observatory (2019) - Deep Carbon Observatory: A Decade of Discovery.

Dobosi G, Kurat G (2010) - On the origin of silicate-bearing diamondites. Mineralogy and Petrology, 99, pp 29–42.

Duan Z, Zhang Z (2006) - Equation of state of the H2O, CO2, and H2O–CO2 systems up to 10 GPa and 2573.15 K: Molecular dynamics simulations with ab initio potential surface. Geochimica et Cosmochimica Acta, 70, pp 2311–2324.

Dvir O, Pettke T, Fumagalli P, Kessel R (2011) - Fluids in the peridotite-water system up to 6 GPa and 800°C: New experimental constrains on dehydration reactions. Contributions to Mineralogy and Petrology, 161, pp 829–844.

Elazar O, Frost D, Navon O, Kessel R (2019) - Melting of H2O and CO2-bearing eclogite at 4–6 GPa and 900–1200 °C: Implications for the generation of diamond-forming fluids. Geochimica et Cosmochimica Acta, 255, pp 69–87.

Endo S, Mizukami T, Wallis SR, Tamura A, Arai S (2014) - Orthopyroxene-rich rocks from the sanbagawa belt (SW Japan): Fluid-rock interaction in the forearc slab-mantle wedge interface. Journal of Petrology, 56, pp 1113–1137.

Evans KA, Tomkins AG (2020) - Metamorphic Fluids in Orogenic Settings. Elements, 16, pp 381–387.

Facq S, Daniel I, Montagnac G, Cardon H, Sverjensky DA (2014) - In situ Raman study and thermodynamic model of aqueous carbonate speciation in equilibrium with aragonite under subduction zone conditions. Geochimica et Cosmochimica Acta, 132, pp 375–390.

Facq S, Daniel I, Montagnac G, Cardon H, Sverjensky DA (2016) - Carbon speciation in saline solutions in equilibrium with aragonite at high pressure. Chemical Geology, 431, pp 44–53.

Farré-de-Pablo J, Pujol-Solà N, Torres-Herrera H, Aiglsperger T, González-Jiménez JM, Llanes-Castro AI, Garcia-Casco A, Proenza JA (2020) - Orthopyroxenite hosted chromitite veins anomalously enriched in platinum-group minerals from the Havana-Matanzas Ophiolite, Cuba Vetas de cromitita en ortopiroxenita anómalamente enriquecidas en minerales del grupo del platino de la ofiolita Habana-Matanzas, Cuba. Boletin de la Sociedad Geologica Mexicana, 72, pp 1–22.

Foley SF, Yaxley GM, Rosenthal A, Buhre S, Kiseeva ES, Rapp RP, Jacob DE (2009) - The composition of near-solidus melts of peridotite in the presence of CO2 and H2O between 40 and 60 kbar. Lithos, 112, pp 274–283.

Formisano V, Atreya S, Encrenaz T, Ignatiev N, Giuranna M (2004) - Detection of methane in the atmosphere of Mars. Science, 306, pp 1758–1761.

Förster MW, Foley SF, Marschall HR, Alard O, Buhre S (2019) - Melting of sediments in the deep mantle produces saline fluid inclusions in diamonds. Science Advances, 5

Franck EU, Rosenzweig S, Christoforakos M (1990) - Calculation of the Dielectric Constant of Water to 1000°C and Very High Pressures. Berichte der Bunsengesellschaft für physikalische Chemie, 94, pp 199–203.

Frezzotti ML, Selverstone J, Sharp ZD, Compagnoni R (2011) - Carbonate dissolution during subduction revealed by diamond-bearing rocks from the Alps. Nature Geoscience, 4, pp 703–706.

Frost DJ (2008) - The upper mantle and transition zone. Elements, 4, pp 171–176.

Frost DJ, McCammon CA (2008) - The Redox State of Earth's Mantle. Annual Reviews, 36, pp 389–420.

Gamsjäger E, Wiessner M (2018) - Low temperature heat capacities and thermodynamic functions described by Debye–Einstein integrals. Monatshefte fur Chemie, 149, pp 357–368.

Gleason JD, Kring DA, Hill DH, Boynton W V. (1997) - Petrography and bulk chemistry of Martian orthopyroxenite ALH84001: Implications for the origin of secondary carbonates. Geochimica et Cosmochimica Acta, 61, pp 3503–3512.

Gonzaga RG, Lowry D, Jacob DE, LeRoex A, Schulze D, Menzies MA (2010) - Eclogites and garnet pyroxenites: Similarities and differences. Journal of Volcanology and Geothermal Research, 190, pp 235–247.

Gorman PJ, Kerrick DM, Connolly JAD (2006) - Modeling open system metamorphic decarbonation of subducting slabs. Geochemistry, Geophysics, Geosystems, 7, pp 4007.

Grant TB, Harlov DE, Rhede D (2016) - Experimental formation of pyroxenite veins by reactions between olivine and Si, Al, Ca, Na, and Cl-rich fluids at 800 ºC and 800 MPa: Implications for fluid metasomatism in the mantle wedge. American Mineralogist, 101, pp 808–818.

Gréau Y, Huang JX, Griffin WL, Renac C, Alard O, O'reilly SY (2011) - Type I eclogites from Roberts Victor kimberlites: Products of extensive mantle metasomatism. Geochimica et Cosmochimica Acta, 75, pp 6927–6954.

Gress MU, Koornneef JM, Thomassot E, Chinn IL, van Zuilen K, Davies GR (2021) - Sm-Nd isochron ages coupled with C-N isotope data of eclogitic diamonds from Jwaneng, Botswana. Geochimica et Cosmochimica Acta, 293, pp 1–17.

Griffin WL, Ryan CG (1995) - Trace elements in indicator minerals: area selection and target evaluation in diamond exploration. Journal of Geochemical Exploration, 53, pp 311–337.

Gross J, Filiberto J, Bell AS (2013) - Water in the martian interior: Evidence for terrestrial MORB mantle-like volatile contents from hydroxyl-rich apatite in olivine–phyric shergottite NWA 6234. Earth and Planetary Science Letters, 369–370, pp 120–128.

Grove TL, Till CB, Krawczynski MJ (2012) - The role of H 2O in subduction zone magmatism. Annual Review of Earth and Planetary Sciences, 40, pp 413–439.

Gurney JJ, Boyd FR (1982) - Mineral intergrowths with polycrystalline diamonds from Orapa Mine, Botswana. Carnegie Institution of Washington, Year 81, pp 267–273.

Gurney JJ, Harris JW, Rickard RS (1984) - Silicate and Oxide Inclusions in Diamonds from the Orapa Mine, Botswana. Kimberlites II: The Mantle and Crust-Mantle Relationships, 11, pp 3–9.

Gurney JJ, Helmstaedt HH, Richardson SH, Shirey SB (2010) - Diamonds through Time. Economic Geology, 105, pp 689–712.

Gysi AP, Jagoutz O, Schmidt M, Targuisti K (2011) - Petrogenesis of Pyroxenites and Melt Infiltrations in the Ultramafic Complex of Beni Bousera, Northern Morocco. Journal of Petrology, 52, pp 1679–1735.

Halama R, Savov IP, Rudnick RL, McDonough WF (2009) - Insights into Li and Li isotope cycling and sub-arc metasomatism from veined mantle xenoliths, Kamchatka. Contributions to Mineralogy and Petrology, 158, pp 197–222.

Hama J, Suito K (2001) - Thermoelastic model of minerals: application to Al2O3. Physics and Chemistry of Minerals, 28, pp 258–267.

Harlov DE (2015) - Apatite: A Fingerprint for Metasomatic Processes. Elements, 11, pp 171–176.

Harris J (1968) - The recognition of diamond inclusions. Part 1: syngenetic mineral inclusions. Industrial Diamond Review, 28, pp 402–410.

Hayes JM, Waldbauer JR (2006) - The carbon cycle and associated redox processes through time. Philosophical Transactions of the Royal Society B: Biological Sciences, 361, pp 931.

Heap MJ, Byrne PK, Mikhail S (2017) - Low surface gravitational acceleration of Mars results in a thick and weak lithosphere: Implications for topography, volcanism, and hydrology. Icarus, 281, pp 103–114.

Helgeson HC (1964) - Complexing and Hydrothermal Ore Deposits. MacMillan, New York.

Helgeson HC (1969) - Thermodynamics of hydrothermal systems at elevated temperatures and pressures. American Journal of Science, 267, pp 729–804.

Helgeson HC, Kirkham DH (1974a) - Theoretical prediction of the thermodynamic behavior of aqueous electrolytes at high pressures and temperatures; I, Summary of the thermodynamic/electrostatic properties of the solvent. American Journal of Science, 274, pp 1089–1198.

Helgeson HC, Kirkham DH (1974b) - Theoretical prediction of the thermodynamic behavior of aqueous electrolytes at high pressures and temperatures; II, Debye-Huckel parameters

for activity coefficients and relative partial molal properties. American Journal of Science, 274, pp 1199–1261.

Helgeson HC, Kirkham DH (1976) - Theoretical prediction of the thermodynamic properties of aqueous electrolytes at high pressures and temperatures. III. Equation of state for aqueous species at infinite dilution. American Journal of Science, 276, pp 97–240.

Helgeson HC, Kirkham DH, Flowers GC (1981) - Theoretical prediction of the thermodynamic behavior of aqueous electrolytes by high pressures and temperatures; IV, Calculation of activity coefficients, osmotic coefficients, and apparent molal and standard and relative partial molal properties to 600 degrees C and 5kb. American Journal of Science, 281, pp 1249–1516.

Herd CDK, Papike JJ, Brearley AJ (2001) - Oxygen fugacity of martian basalts from electron microprobe oxygen and TEM-EELS analyses of Fe-Ti oxides. American Mineralogist, 86, pp 1015–1024.

Herd CDK, Borg LE, Jones JH, Papike JJ (2002) - Oxygen fugacity and geochemical variations in the martian basalts: implications for martian basalt petrogenesis and the oxidation state of the upper mantle of Mars. Geochimica et Cosmochimica Acta, 66, pp 2025–2036.

Hirauchi KI, den Hartog SAM, Spiers CJ (2013) - Weakening of the slab–mantle wedge interface induced by metasomatic growth of talc. Geology, 41, pp 75–78.

Hirschmann MM, Withers AC (2008) - Ventilation of CO2 from a reduced mantle and consequences for the early Martian greenhouse. Earth and Planetary Science Letters, 270, pp 147–155.

Hoffman PF, Kaufman AJ, Halverson GP, Schrag DP (1998) - A Neoproterozoic Snowball Earth Science, New Series, Vol. 281, pp 1342–1346.

Hofmann AW (2007) - Sampling Mantle Heterogeneity through Oceanic Basalts: Isotopes and Trace Elements. Treatise on Geochemistry, 2–9, pp 1–44.

Holland TJB, Powell R (2018) - An improved and extended internally consistent thermodynamic dataset for phases of petrological interest, involving a new equation of state for solid. Journal of Metamorphic Geology, 29, pp 333–383.

Holloway JR (1998) - Graphite-melt equilibria during mantle melting: constraints on CO2 in MORB magmas and the carbon content of the mantle. Chemical Geology, 147, pp 89–97.

Howarth GH, Pernet-Fisher JF, Balta JB, Barry PH, Bodnar RJ, Taylor LA (2014) - Two-stage polybaric formation of the new enriched, pyroxene-oikocrystic, lherzolitic shergottite, NWA 7397. Meteoritics & Planetary Science, 49, pp 1812–1830.

Huang J, Hao J, Huang F, Sverjensky DA (2019) - Mobility of chromium in high temperature crustal and upper mantle fluids. Geochemical Perspectives Letters, 12, pp 1–6.

Huang F, Sverjensky DA (2019) - Extended Deep Earth Water Model for predicting major element mantle metasomatism. Geochimica et Cosmochimica Acta, 254, pp 192–230.

Huang F, Sverjensky DA (2020) - Mixing of carbonatitic into saline fluid during panda diamond formation. Geochimica et Cosmochimica Acta, 284, pp 1–20.

Hunt JD, Kavner A, Schauble EA, Snyder D, Manning CE (2011) - Polymerization of aqueous silica in H2O–K2O solutions at 25–200 °C and 1 bar to 20 kbar. Chemical Geology, 283, pp 161–170.

Hunt JD, Manning CE (2012) - A thermodynamic model for the system SiO2–H2O near the upper critical end point based on quartz solubility experiments at 500–1100 °C and 5–20 kbar. Geochimica et Cosmochimica Acta, 86, pp 196–213.

Huybers P, Langmuir C (2009) - Feedback between deglaciation, volcanism, and atmospheric CO2. Earth and Planetary Science Letters, 286, pp 479–491.

Izraeli ES, Harris JW, Navon O (2001) - Brine inclusions in diamonds: a new upper mantle fluid. Earth and Planetary Science Letters, 187, pp 323–332.

Jacob DE, Viljoen KS, Grassineau N, Jagoutz E (2000) - Remobilization in the Cratonic Lithosphere Recorded in Polycrystalline Diamond. Science, 289, pp 1182–1185.

Jacob DE, Dobrzhinetskaya L, Wirth R (2014) - New insight into polycrystalline diamond genesis from modern nanoanalytical techniques. Earth-Science Reviews, 136, pp 21–35.

Jacob DE, Piazolo S, Schreiber A, Trimby P (2016) - Redox-freezing and nucleation of diamond via magnetite formation in the Earth's mantle. Nature Communications, 7, pp 1–7.

Jambon A (1994) - Earth degassing and large-scale geochemical cycling of volatile elements. Reviews in Mineralogy and Geochemistry, 30, pp 479–517.

Johnson JW, Oelkers EH, Helgeson HC (1992) - SUPCRT92: A software package for calculating the standard molal thermodynamic properties of minerals, gases, aqueous species, and reactions from 1 to 5000 bar and 0 to 1000°C. Computers & Geosciences, 18, pp 899–947.

Kaczmarek MA, Jonda L, Davies HL (2015) - Evidence of melting, melt percolation and deformation in a supra-subduction zone (Marum ophiolite complex, Papua New Guinea). Contributions to Mineralogy and Petrology, 170, pp 1–23.

Kadik AA, Kurovskaya NA, Ignat'ev YA, Kryukova EB, Koltashev V V., Kononkova NN (2013) - Use of platinum capsules in the study of the carbon and hydrogen solubility in silicate melts in equilibrium with liquid iron alloys at high pressures and temperatures. Geochemistry International, 51, pp 1019–1024.

Kawamoto T, Mibe K, Bureau H, Reguer S, Mocuta C, Kubsky S, Thiaudière D, Ono S, Kogiso T (2014) - Large-ion lithophile elements delivered by saline fluids to the sub-arc mantle. Earth, Planets and Space, 66, pp 1–11.

Keller T, Katz RF, Hirschmann MM (2017) - Volatiles beneath mid-ocean ridges: Deep melting, channelised transport, focusing, and metasomatism. Earth and Planetary Science Letters, 464, pp 55–68.

Keppler H (2003) - Water solubility in carbonatite melts. American Mineralogist, 88, pp 1822–1824.

Kerrick DM, Connolly JAD (2001) - Metamorphic devolatilization of subducted marine sediments and the transport of volatiles into the Earth's mantle. Nature, 411, pp 291–296.

Kessel R, Schmidt MW, Ulmer P, Pettke T (2005a) - Trace element signature of subduction-zone fluids, melts and supercritical liquids at 120–180 km depth. Nature, 437, pp 724–727.

Kessel R, Ulmer P, Pettke T, Schmidt MW, Thompson AB (2005b) - The water–basalt system at 4 to 6 GPa: Phase relations and second critical endpoint in a K-free eclogite at 700 to 1400 °C. Earth and Planetary Science Letters, 237, pp 873–892.

Kessel R, Pettke T, Fumagalli P (2015) - Melting of metasomatized peridotite at 4–6 GPa and up to 1200 °C: an experimental approach. Contributions to Mineralogy and Petrology, 169, pp 1–19.

Kiseeva ES, Wood BJ, Ghosh S, Stachel T (2016) - The pyroxenite-diamond connection. Geochemical Perspectives Letters, 2, pp 1–9.

Knapmeyer-Endrun B, Panning MP, Bissig F, et al (2021) - Thickness and structure of the martian crust from InSight seismic data. Science, 373, pp 438–443.

Koornneef JM, Gress MU, Chinn IL, Jelsma HA, Harris JW, Davies GR (2017) - Archaean and Proterozoic diamond growth from contrasting styles of large-scale magmatism. Nature Communications, 8, pp 1–8.

Kopylova MG, Russell JK, Cookenboo H (1999) - Petrology of peridotite and pyroxenite xenoliths from the Jericho Kimberlite: Implications for the thermal state of the mantle beneath the Slave Craton, Northern Canada. Journal of Petrology, 40, pp 79–104.

Kopylova MG, Hayman P (2008) - Petrology and textural classification of the Jericho kimberlite, northern Slave Province, Nunavut, Canada. Canadian Journal of Earth Sciences, 45, pp 701–723.

Lapen TJ, Righter M, Andreasen R, Irving AJ, Satkoski AM, Beard BL, Nishiizumi K, Jull AJT, Caffee MW (2017) - Two billion years of magmatism recorded from a single Mars meteorite ejection site. Science Advances, 3.

Lasaga AC, Gibbs G V. (1987) - Applications of quantum mechanical potential surfaces to mineral physics calculations. Physics and Chemistry of Minerals, 14, pp 107–117.

Laukert G, Von Der Handt A, Hellebrand E, Snow JE, Hoppe P, Klügel A (2014) - High-pressure Reactive Melt Stagnation Recorded in Abyssal Pyroxenites from the Ultraslow-spreading Lena Trough, Arctic Ocean. Journal of Petrology, 55, pp 427–458.

Lee C-TA, Jiang H, Dasgupta R, Torres M (2019) - A Framework for Understanding Whole-Earth Carbon Cycling. Deep Carbon: Past to Present Cambridge: Cambridge University Press, pp 313–357.

Lenardic A, Nimmo F, Moresi L (2004) - Growth of the hemispheric dichotomy and the cessation of plate tectonics on Mars. Journal of Geophysical Research: Planets, 109, pp 2003.

Litasov KD, Ohtani E (2009) - Solidus and phase relations of carbonated peridotite in the system CaO–Al2O3–MgO–SiO2–Na2O–CO2 to the lower mantle depths. Physics of the Earth and Planetary Interiors, 177, pp 46–58.

Liu X, Luo J, Yin N, Tan ZC, Shi Q (2018) - Applications of low temperature calorimetry in material research. Chinese Chemical Letters, 29, pp 664–670.

Liu J, Wang J, Hattori K, Wang Z (2022) - Petrogenesis of Garnet Clinopyroxenite and Associated Dunite in Hujialin, Sulu Orogenic Belt, Eastern China. Minerals, 12, pp 162.

Lord OT, Walter MJ, Dasgupta R, Walker D, Clark SM (2009) - Melting in the Fe–C system to 70 GPa. Earth and Planetary Science Letters, 284, pp 157–167.

Lu JG, Griffin WL, Huang JX, Dai HK, Castillo-Oliver M, O'Reilly SY (2022) - Structure and composition of the lithosphere beneath Mount Carmel, North Israel. Contributions to Mineralogy and Petrology, 177, pp 1–16.

Luth RW (1999) - Carbon and carbonates in the mantle. In: Fei Y, Bertka CM, Mysen BO (eds) Mantle Petrology: Field Observations and High Pressure Experimenta- tion: A Tribute to Francis R. (Joe) Boyd. The Geochemical Society, pp 297–316.

Luth RW, Stachel T (2014) - The buffering capacity of lithospheric mantle: implications for diamond formation. Contributions to Mineralogy and Petrology, 168, pp 1–12.

Malaspina N, Hermann J, Scambelluri M, Compagnoni R (2006) - Polyphase inclusions in garnet–orthopyroxenite (Dabie Shan, China) as monitors for metasomatism and fluid-related trace element transfer in subduction zone peridotite. Earth and Planetary Science Letters, 249, pp 173–187.

Malaspina N, Hermann J, Scambelluri M (2009) - Fluid/mineral interaction in UHP garnet peridotite. Lithos, 107, pp 38–52.

Manning CE (1994) - The solubility of quartz in H2O in the lower crust and upper mantle. Geochimica et Cosmochimica Acta, 58, pp 4831–4839.

Manning CE (2004) - The chemistry of subduction-zone fluids. Earth and Planetary Science Letters, 223, pp 1–16.

Manning CE (2013) - Thermodynamic Modeling of Fluid-Rock Interaction at Mid-Crustal to Upper-Mantle Conditions. Reviews in Mineralogy and Geochemistry, 76, pp 135–164.

Manning CE, Shock EL, Sverjensky DA (2013) - The Chemistry of Carbon in Aqueous Fluids at Crustal and Upper-Mantle Conditions: Experimental and Theoretical Constraints. Reviews in Mineralogy and Geochemistry, 75, pp 109–148.

Manning CE, Frezzotti ML (2020) - Subduction-zone fluids. Elements, 16, pp 395–400.

Marschall HR, Schumacher JC (2012) - Arc magmas sourced from mélange diapirs in subduction zones. Nature Geoscience, 5, pp 862–867.

McCubbin FM, Hauri EH, Elardo SM, Vander Kaaden KE, Wang J, Shearer CK (2012) - Hydrous melting of the martian mantle produced both depleted and enriched shergottites. Geology, 40, pp 683–686.

McCubbin FM, Boyce JW, Srinivasan P, Santos AR, Elardo SM, Filiberto J, Steele A, Shearer CK (2016) - Heterogeneous distribution of H2O in the Martian interior: Implications for the abundance of H2O in depleted and enriched mantle sources. Meteoritics & Planetary Science, 51, pp 2036–2060.

McInnes BIA, Gregoire M, Binns RA, Herzig PM, Hannington MD (2001) - Hydrous metasomatism of oceanic sub-arc mantle, Lihir, Papua New Guinea: petrology and geochemistry of fluid-metasomatised mantle wedge xenoliths. Earth and Planetary Science Letters, 188, pp 169–183.

Melcher F, Meisel T (2004) - A Metamorphosed Early Cambrian Crust–Mantle Transition in the Eastern Alps, Austria. Journal of Petrology, 45, pp 1689–1723.

Meltzer A, Kessel R (2022) - The interaction of slab-derived silicic fluid and harzburgite – Metasomatism in the sub cratonic lithospheric mantle. Geochimica et Cosmochimica Acta, 328, pp 103–119.

Mikhail S, Verchovsky AB, Howell D, Hutchison MT, Southworth R, Thomson AR, Warburton P, Jones AP, Milledge HJ (2014) - Constraining the internal variability of the

stable isotopes of carbon and nitrogen within mantle diamonds. Chemical Geology, 366, pp 14–23.

Mikhail S, Crosby JC, Stuart FM, DiNicola L, Abernethy FAJ (2019a) - A secretive mechanical exchange between mantle and crustal volatiles revealed by helium isotopes in 13C-depleted diamonds. Geochemical Perspectives Letters, 11, pp 39–43.

Mikhail S, McCubbin FM, Jenner FE, Shirey SB, Rumble D, Bowden R (2019b) - Diamondites: evidence for a distinct tectono-thermal diamond-forming event beneath the Kaapvaal craton. Contributions to Mineralogy and Petrology, 174, pp 1–15.

Mikhail S, Rinaldi M, Mare ER, Sverjensky DA (2021) - A genetic metasomatic link between eclogitic and peridotitic diamond inclusions. Geochemical Perspectives Letters, 17, pp 33–38.

Miller CE, Kopylova M, Smith E (2014) - Mineral inclusions in fibrous diamonds: Constraints on cratonic mantle refertilization and diamond formation. Mineralogy and Petrology, 108, pp 317–331.

Miron GD, Leal AMM, Yapparova A (2019) - Thermodynamic Properties of Aqueous Species Calculated Using the HKF Model: How Do Different Thermodynamic and Electrostatic Models for Solvent Water Affect Calculated Aqueous Properties? Geofluids, 2019

Molina JF, Poli S (2000) - Carbonate stability and fluid composition in subducted oceanic crust: An experimental study on H2O-CO2-bearing basalts. Earth and Planetary Science Letters, 176, pp 295–310.

Moore DE, Lockner DA (2010) - Comparative Deformation Behavior of Minerals in Serpentinized Ultramafic Rock: Application to the Slab-Mantle Interface in Subduction Zones. International Geology Review, 49, pp 401–415.

Morishige M, van Keken PE (2018) - Fluid Migration in a Subducting Viscoelastic Slab. Geochemistry, Geophysics, Geosystems, 19, pp 337–355.

Morrissey LJ, Tomkins AG (2020) - Evaporite-bearing orogenic belts produce ligand-rich and diverse metamorphic fluids. Geochimica et Cosmochimica Acta, 275, pp 163–187.

Mumma MJ, Villanueva GL, Novak RE, Hewagama T, Bonev BP, DiSanti MA, Mandell AM, Smith MD (2009) - Strong release of methane on Mars in northern summer 2003. Science, 323, pp 1041–1045.

Murakami M (2013) - Chemical Composition of the Earth's Lower Mantle: Constraints from Elasticity. Physics and Chemistry of the Deep Earth, pp 183–212.

Mysen BO (2010) - Speciation and mixing behavior of silica-saturated aqueous fluid at high temperature and pressure. American Mineralogist, 95, pp 1807–1816.

Mysen BO, Mibe K, Chou IM, Bassett WA (2013) - Structure and equilibria among silicate species in aqueous fluids in the upper mantle: Experimental SiO2–H2O and MgO–SiO2–H2O data recorded in situ to 900°C and 5.4 GPa. Journal of Geophysical Research: Solid Earth, 118, pp 6076–6085.

Mysen B (2022) - Fluids and physicochemical properties and processes in the Earth. Progress in Earth and Planetary Science, 9, 54.

Navon O, Hutcheon ID, Rossman GR, Wasserburg GJ (1988) - Mantle-derived fluids in diamond micro-inclusions. Nature, 335, pp 784–789.

Nekvasil H, Filiberto J, McCubbin FM, Lindsley DH (2007) - Alkalic parental magmas for chassignites? Meteoritics & Planetary Science, 42, pp 979–992.

Nestola F, Jung H, Taylor LA (2017) - Mineral inclusions in diamonds may be synchronous but not syngenetic. Nature Communications, 8, pp 1–6.

Newton RC, Manning CE (2002) - Solubility of enstatite + forsterite in H2O at deep crust/upper mantle conditions: 4 to 15 kbar and 700 to 900°c. Geochimica et Cosmochimica Acta, 66, pp 4165–4176.

Newton RC, Manning CE (2008) - Thermodynamics of SiO2–H2O fluid near the upper critical end point from quartz solubility measurements at 10 kbar. Earth and Planetary Science Letters, 274, pp 241–249.

Newton RC, Manning CE (2010) - Role of saline fluids in deep-crustal and upper-mantle metasomatism: Insights from experimental studies. Geofluids, 10, pp 58–72.

O'Driscoll B, Walker RJ, Day JMD, Ash RD, Daly JS (2015) - Generations of Melt Extraction, Melt–Rock Interaction and High-Temperature Metasomatism Preserved in Peridotites of the ~497 Ma Leka Ophiolite Complex, Norway. Journal of Petrology, 56, pp 1797–1828.

Ohtani E (2020) - The role of water in Earth's mantle. National Science Review, 7, pp 224–232.

O'Reilly S, Griffin WL (2013) - Mantle metasomatism. In: Harlov D, Austrheim H (eds) In: Metasomatism and the chemical transformation of rock, Lecture Notes in Earth System Sciences. Springer, Berlin, Heidelberg. pp 471–533

Padrón-Navarta JA, Sánchez-Vizcaí VL, Garrido CJ, Gómez-Pugnaire MT (2011) - Metamorphic Record of High-pressure Dehydration of Antigorite Serpentinite to Chlorite Harzburgite in a Subduction Setting (Cerro del Almirez, Nevado–Filábride Complex, Southern Spain). Journal of Petrology, 52, pp 2047–2078.

Palyanov YN, Kupriyanov IN, Khokhryakov AF, Ralchenko VG (2015) - Crystal Growth of Diamond. Handbook of Crystal Growth: Bulk Crystal Growth: Second Edition, 2, pp 671–713.

Pan D, Spanu L, Harrison B, Sverjensky DA, Galli G (2013) - Dielectric properties of water under extreme conditions and transport of carbonates in the deep Earth. Proceedings of the National Academy of Sciences of the United States of America, 110, pp 6646–6650.

Panero WR, Kabbes JE (2008) - Mantle-wide sequestration of carbon in silicates and the structure of magnesite II. Geophysical Research Letters, 35, pp 14307.

Pasqualetto L, Nestola F, Jacob DE, et al (2022) - Protogenetic clinopyroxene inclusions in diamond and Nd diffusion modeling—Implications for diamond dating. Geology, 50, pp 1038–1042.

Pearson DG, Davies GR, Nixon PH (1993) - Geochemical Constraints on the Petrogenesis of Diamond Facies Pyroxenites from the Beni Bousera Peridotite Massif, North Morocco. Journal of Petrology, 34, pp 125–172.

Pearson DG, Canil D, Shirey SB (2014) - Mantle Samples Included in Volcanic Rocks: Xenoliths and Diamonds. Treatise on Geochemistry: Second Edition, 3, pp 169–253.

Pellegrino L, Malaspina N, Zanchetta S, Langone A, Tumiati S (2020) - High pressure melting of eclogites and metasomatism of garnet peridotites from Monte Duria Area (Central Alps, N Italy): A proxy for melt-rock reaction during subduction. Lithos, 358–359

Pintér Z, Foley SF, Yaxley GM (2022) - Diamonds, dunites, and metasomatic rocks formed by melt/rock reaction in craton roots. Communications Earth & Environment, 3, pp 1–8.

Poli S, Schmidt MW (2003) - Petrology of Subducted Slabs. Annual Review of Earth and Planetary Sciences, 30, pp. 207–235.

Poli S, Franzolin E, Fumagalli P, Crottini A (2009) - The transport of carbon and hydrogen in subducted oceanic crust: An experimental study to 5 GPa. Earth and Planetary Science Letters, 278, pp 350–360.

Poli S (2015) - Carbon mobilized at shallow depths in subduction zones by carbonatitic liquids. Nature Geoscience, 8, pp 633–636.

Ricketts B Geological Digressions. https://www.geological-digressions.com/how-to-do-field-tasks/geofluids/. Accessed 7 Apr 2023.

Righter K, Yang H, Costin G, Downs RT (2008) - Oxygen fugacity in the Martian mantle controlled by carbon: New constraints from the nakhlite MIL 03346. Meteoritics & Planetary Science, 43, pp 1709–1723.

Rohrbach A, Ballhaus C, Golla-Schindler U, Ulmer P, Kamenetsky VS, Kuzmin D V. (2007) - Metal saturation in the upper mantle. Nature, 449, pp 456–458.

Sahle CJ, Sternemann C, Schmidt C, et al (2013) - Microscopic structure of water at elevated pressures and temperatures. Proceedings of the National Academy of Sciences of the United States of America, 110, pp 6301–6306.

Santos SSM, Marcondes ML, Justo JF, Assali LVC (2019) - Stability of calcium and magnesium carbonates at Earth's lower mantle thermodynamic conditions. Earth and Planetary Science Letters, 506, pp 1–7.

Scambelluri M, Bottazzi P, Trommsdorff V, Vannucci R, Hermann J, Gòmez-Pugnaire MT, Lòpez-Sànchez Vizcano V (2001) - Incompatible element-rich fluids released by antigorite breakdown in deeply subducted mantle. Earth and Planetary Science Letters, 192, pp 457–470.

Scheuermann PP, Tan C, Seyfried WE (2018) - Quartz Solubility in the Two-Phase Region of the NaCl-H2O System: An Experimental Study With Application to the Piccard Hydrothermal Field, Mid-Cayman Rise. Geochemistry, Geophysics, Geosystems, 19, pp 3570–3582.

Schmidt C, Manning CE (2017) - Pressure-induced ion pairing in MgSO4solutions: Implications for the oceans of icy worlds. Geochemical Perspectives Letters, 3, pp 66–74.

Schulze DJ, Harte B, Valley JW, Brenan JM, De R. Channer DM (2003) - Extreme crustal oxygen isotope signatures preserved in coesite in diamond. Nature 423, 68–70.

Shcheka SS, Wiedenbeck M, Frost DJ, Keppler H (2006) - Carbon solubility in mantle minerals. Earth and Planetary Science Letters, 245, pp 730–742.

Shirey SB, Cartigny P, Frost DJ, Keshav S, Nestola F, Nimis P, Pearson DG, Sobolev N V., Walter MJ (2013) - Diamonds and the Geology of Mantle Carbon. Reviews in Mineralogy and Geochemistry, 75, pp 355–421.

Shock EL, Helgeson HC (1988) - Calculation of the thermodynamic and transport properties of aqueous species at high pressures and temperatures: Correlation algorithms for ionic species and equation of state predictions to 5 kb and 1000°C. Geochimica et Cosmochimica Acta, 52, pp 2009–2036.

Shock EL, Helgeson HC, Sverjensky DA (1989) - Calculation of the thermodynamic and transport properties of aqueous species at high pressures and temperatures: Standard partial molal properties of inorganic neutral species. Geochimica et Cosmochimica Acta, 53, pp 2157–2183.

Shock EL, Helgeson HC (1990) - Calculation of the thermodynamic and transport properties of aqueous species at high pressures and temperatures: Standard partial molal properties of organic species. Geochimica et Cosmochimica Acta, 54, pp 915–945.

Shock EL, Sassani DC, Willis M, Sverjensky DA (1997) - Inorganic species in geologic fluids: Correlations among standard molal thermodynamic properties of aqueous ions and hydroxide complexes. Geochimica et Cosmochimica Acta, 61, pp 907–950.

Sklyarov E V., Lavrenchuk A V., Doroshkevich AG, Starikova AE, Kanakin S V. (2021) - Pyroxenite as a product of mafic-carbonate melt interaction (Tazheran massif, west baikal area, russia). Minerals, 11.

Sleep NH, Zahnle K (2001) - Carbon dioxide cycling and implications for climate on ancient Earth. Journal of Geophysical Research: Planets, 106, pp 1373–1399.

Smart KA, Chacko T, Stachel T, Tappe S, Stern RA, Ickert RB (2012) - Eclogite formation beneath the northern Slave craton constrained by diamond inclusions: Oceanic lithosphere origin without a crustal signature. Earth and Planetary Science Letters, 319–320, pp 165–177.

Sobolev A V., Hofmann AW, Kuzmin D V., et al (2007) - The Amount of Recycled Crust in Sources of Mantle-Derived Melts. Science, 316, pp 412–417.

Sobolev N V., Logvinova AM, Zedgenizov DA, Pokhilenko NP, Malygina E V., Kuzmin D V., Sobolev A V. (2009) - Petrogenetic significance of minor elements in olivines from diamonds and peridotite xenoliths from kimberlites of Yakutia. Lithos, 112, pp 701–713.

Soderman CR, Shorttle O, Gazel E, Geist DJ, Matthews S, Williams HM (2023) - The evolution of the Galápagos mantle plume. Science Advances, 9.

Sonin V, Tomilenko A, Zhimulev E, Bul'bak T, Chepurov A, Babich Y, Logvinova A, Timina T, Chepurov A (2022) - The composition of the fluid phase in inclusions in synthetic HPHT diamonds grown in system Fe–Ni–Ti–C. Scientific Reports, 12, pp 1–9.

Spera FJ, BohrSon W, tIll chrISty B, GhIorSo MS (2007) - Partitioning of trace elements among coexisting crystals, melt, and supercritical fluid during isobaric crystallization and melting. American Mineralogist, 92, pp 1881–1898.

Stachel T, Harris JW (2008) - The origin of cratonic diamonds — Constraints from mineral inclusions. Ore Geology Reviews, 34, pp 5–32.

Stachel T, Luth RW (2015) - Diamond formation — Where, when and how? Lithos, 220–223, pp 200–220.

Stachel T, Cartigny P, Chacko T, Pearson DG (2022) - Carbon and Nitrogen in Mantle-Derived Diamonds. Reviews in Mineralogy and Geochemistry, 88, pp 809–875.

Stagno V, Frost DJ, McCammon CA, Mohseni H, Fei Y (2015) - The oxygen fugacity at which graphite or diamond forms from carbonate-bearing melts in eclogitic rocks. Contributions to Mineralogy and Petrology, 169, pp 1–18.

Steele A, McCubbin FM, Fries M, et al (2012) - A reduced organic carbon component in martian basalts. Science, 337, pp 212–215.

Stixrude L, Lithgow-Bertelloni C (2011) - Thermodynamics of mantle minerals - II. Phase equilibria. Geophysical Journal International, 184, pp 1180–1213.

Storey M, Duncan RA, Swisher CC (2007) - Paleocene-Eocene thermal maximum and the opening of the northeast Atlantic. Science, 316, pp 587–589.

Suarez CA, Edmonds M, Jones AP (2019) - Earth Catastrophes and their Impact on the Carbon Cycle. Elements, 15, pp 301–306.

Sverjensky DA, Hemley JJ, D'angelo WM (1991) - Thermodynamic assessment of hydrothermal alkali feldspar-mica-aluminosilicate equilibria. Geochimica et Cosmochimica Acta, 55, pp 989–1004.

Sverjensky DA, Shock EL, Helgeson HC (1997) - Prediction of the thermodynamic properties of aqueous metal complexes to 1000°C and 5 kb. Geochimica et Cosmochimica Acta, 61, pp 1359–1412.

Sverjensky DA, Harrison B, Azzolini D (2014a) - Water in the deep Earth: The dielectric constant and the solubilities of quartz and corundum to 60 kb and 1200 °C. Geochimica et Cosmochimica Acta, 129, pp 125–145.

Sverjensky DA, Stagno V, Huang F (2014b) - Important role for organic carbon in subduction-zone fluids in the deep carbon cycle. Nature Geoscience, 7, pp 909–913.

Sverjensky DA, Huang F (2015) - Diamond formation due to a pH drop during fluid-rock interactions. Nature Communications, 6.

Sverjensky DA (2019) - Thermodynamic modelling of fluids from surficial to mantle conditions. Journal of the Geological Society, 176, pp 348–374.

Sverjensky D, Daniel I, Vitale Brovarone A (2020) - The Changing Character of Carbon in Fluids with Pressure. Geophysical Monograph Series, 249, pp 259–269.

Tanger JC, Helgeson HC (1988) - Calculation of the thermodynamic and transport properties of aqueous species at high pressures and temperatures; revised equations of state for the standard partial molal properties of ions and electrolytes. American Journal of Science, 288, pp 19–98.

Tappert R, Stachel T, Harris JW, Shimizu N, Brey GP (2005) - Mineral inclusions in diamonds from the Panda kimberlite, Slave Province, Canada. European Journal of Mineralogy, 17, pp 423–440.

Tappert R, Foden J, Stachel T, Muehlenbachs K, Tappert M, Wills K (2009) - The diamonds of South Australia. Lithos, 112, pp 806–821.

Taylor WR, Green DH (1986) - The role of reduced C-O-H fluids in mantle partial melting. International Kimberlite Conference: Extended Abstracts, 4, pp 211–213.

Thomsen TB, Schmidt MW (2008) - Melting of carbonated pelites at 2.5-5.0 GPa, silicate-carbonatite liquid immiscibility, and potassium-carbon metasomatism of the mantle. Earth and Planetary Science Letters, 267, pp 17–31.

Thomson AR, Walter MJ, Kohn SC, Brooker RA (2016) - Slab melting as a barrier to deep carbon subduction. Nature, 529, pp 76–79.

Timina TY, Tomilenko AA, Kovyazin S V. (2015) - Fluid regime of formation of clinopyroxenites from the mantle wedge beneath Avacha volcano (Kamchatka). Doklady Earth Sciences, 463, pp 851–854.

Timmerman S, Spivak A V., Jones AP (2021) - Carbonatitic Melts and Their Role in Diamond Formation in the Deep Earth. Elements, 17, pp 321–326.

Tiraboschi C, Tumiati S, Sverjensky D, Pettke T, Ulmer P, Poli S (2018) - Experimental determination of magnesia and silica solubilities in graphite-saturated and redox-buffered high-pressure COH fluids in equilibrium with forsterite + enstatite and magnesite + enstatite. Contributions to Mineralogy and Petrology, 173, pp 1–17.

Tiraboschi C, Miozzi F, Tumiati S (2022) - Carbon-saturated COH fluids in the upper mantle: A review of high-pressure and high-temperature ex situ experiments. European Journal of Mineralogy, 34, pp 59–75.

Tomlinson EL, Jones AP, Harris JW (2006) - Co-existing fluid and silicate inclusions in mantle diamond. Earth and Planetary Science Letters, 250, pp 581–595.

Treiman AH (2005) - The nakhlite meteorites: Augite-rich igneous rocks from Mars. Geochemistry, 65, pp 203–270.

Tropper P, Manning CE (2007) - The solubility of corundum in H2O at high pressure and temperature and its implications for Al mobility in the deep crust and upper mantle. Chemical Geology, 240, pp 54–60.

Tsay A, Zajacz Z, Ulmer P, Sanchez-Valle C (2017) - Mobility of major and trace elements in the eclogite-fluid system and element fluxes upon slab dehydration. Geochimica et Cosmochimica Acta, 198, pp 70–91.

Tumiati S, Tiraboschi C, Sverjensky DA, Pettke T, Recchia S, Ulmer P, Miozzi F, Poli S (2017) - Silicate dissolution boosts the CO2 concentrations in subduction fluids. Nature Communications, 8, pp 1–11.

Tumiati S, Malaspina N (2019) - Redox processes and the role of carbon-bearing volatiles from the slab–mantle interface to the mantle wedge. Journal of the Geological Society, 176, pp 388–397.

Udry A, Howarth GH, Lapen TJ, Righter M (2017) - Petrogenesis of the NWA 7320 enriched martian gabbroic shergottite: Insight into the martian crust. Geochimica et Cosmochimica Acta, 204, pp 1–18.

Ulmer P (2001) - Partial melting in the mantle wedge — the role of H2O in the genesis of mantle-derived 'arc-related' magmas. Physics of the Earth and Planetary Interiors, 127, pp 215–232.

Varas-Reus MI, Garrido CJ, Marchesi C, Bosch D, Hidas K (2018) - Genesis of ultra-high pressure garnet pyroxenites in orogenic peridotites and its bearing on the compositional

heterogeneity of the Earth's mantle. Geochimica et Cosmochimica Acta, 232, pp 303–328.

Viljoen KS, Phillips D, Harris JW, Robinson DN (1998) - Mineral inclusions in diamonds from the Venetia kimberlites, Northern Province, South Africa. International Kimberlite Conference: Extended Abstracts, 7, pp 943–945.

Vlastélic I, Sainlot N, Samaniego P, Bernard B, Nauret F, Hidalgo S, Auclair D, Gannoun A (2023) - Arc volcano activity driven by small-scale metasomatism of the magma source. Nature Geoscience 2023, pp 1–8.

Walter MJ, Bulanova GP, Armstrong LS, et al (2008) - Primary carbonatite melt from deeply subducted oceanic crust. Nature, 454, pp 622–625.

Wang J, Hattori KH, Stern CR (2008) - Metasomatic origin of garnet orthopyroxenites in the subcontinental lithospheric mantle underlying Pali Aike volcanic field, southern South America. Mineralogy and Petrology, 94, pp 243–258.

Wang C, Liang Y, Dygert N, Xu W (2016) - Formation of orthopyroxenite by reaction between peridotite and hydrous basaltic melt: an experimental study. Contributions to Mineralogy and Petrology, 171, pp 1–18.

Warren JM, Shimizu N, Sakaguchi C, Dick HJB, Nakamura E (2009) - An assessment of upper mantle heterogeneity based on abyssal peridotite isotopic compositions. Journal of Geophysical Research: Solid Earth, 114.

Watson BE, Lupulescu A (1993) - Aqueous fluid connectivity and chemical transport in clinopyroxene-rich rocks. Earth and Planetary Science Letters, 117, pp 279–294.

Webster CR, Mahaffy PR, Atreya SK, et al (2013) - Low upper limit to methane abundance on Mars. Science, 342, pp 355–357.

Webster CR, Mahaffy PR, Atreya SK, et al (2018) - Background levels of methane in Mars' atmosphere show strong seasonal variations. Science, 360, pp 1093–1096.

Weiss Y, Kessel R, Griffin WL, Kiflawi I, Klein-BenDavid O, Bell DR, Harris JW, Navon O (2009) - A new model for the evolution of diamond-forming fluids: Evidence from microinclusion-bearing diamonds from Kankan, Guinea. Lithos, 112, pp 660–674.

Weiss Y, Kiflawi I, Davies N, Navon O (2014) - High-density fluids and the growth of monocrystalline diamonds. Geochimica et Cosmochimica Acta, 141, pp 145–159.

Weiss Y, McNeill J, Pearson DG, Nowell GM, Ottley CJ (2015) - Highly saline fluids from a subducting slab as the source for fluid-rich diamonds. Nature, 524, pp 339–342.

Weiss Y, Class C, Goldstein SL, Hanyu T (2016) - Key new pieces of the HIMU puzzle from olivines and diamond inclusions. Nature, 537, pp 666–670.

Weiss Y, Czas J, Navon O (2022) - Fluid Inclusions in Fibrous Diamonds. Reviews in Mineralogy and Geochemistry, 88, pp 475–532.

Wetzel DT, Rutherford MJ, Jacobsen SD, Hauri EH, Saal AE (2013) - Degassing of reduced carbon from planetary basalts. Proceedings of the National Academy of Sciences of the United States of America, 110, pp 8010–8013.

White LT, Rawlinson N, Lister GS, et al (2019) - Earth's deepest earthquake swarms track fluid ascent beneath nascent arc volcanoes. Earth and Planetary Science Letters, 521, pp 25–36.

Wolery TJ (1983) - EQ3NR: A Computer Program for Geochemical Aqueous Speciation-Solubility Calculations, User's Guide and Documentation: UCRL- 53414.

Wolery TJ (1984) - EQ6---A computer Program For Reaction-Path Modelling of Aqueous Geochemical Systems: User's Guide and Documentation: UCRL-51.

Wolery TJ (1992) - EQ3NR, a computer program for geochemical aqueous speciation-solubility calculations: theoretical manual, user's guide, and related documentation (version 7.0).

Wyllie PJ, Ryabchikov ID (2000) - Volatile Components, Magmas, and Critical Fluids in Upwelling Mantle. Journal of Petrology, 41, pp 1195–1206.

Yaxley GM, Brey GP (2004) - Phase relations of carbonate-bearing eclogite assemblages from 2.5 to 5.5 GPa: Implications for petrogenesis of carbonatites. Contributions to Mineralogy and Petrology, 146, pp 606–619.

Yaxley GM, Kjarsgaard BA, Jaques AL (2021) - Evolution of Carbonatite Magmas in the Upper Mantle and Crust. Elements, 17, pp 315–320.

Yoder HS, Tilley CE (1962) - Origin of Basalt Magmas: An Experimental Study of Natural and Synthetic Rock Systems. Journal of Petrology, 3, pp 342–532.

Zhang C, Duan Z (2009) - A model for C-O-H fluid in the Earth's mantle. Geochimica et Cosmochimica Acta, 73, pp 2089–2102.

Zharikovf VA, Pertsev NN, Rusinov VL, Callegari E, Fettes DJ (2006) - 9. Metasomatism and metasomatic rocks. In: Fettes D, Desmons J (eds) Metamorphic rocks – a classification and glossary of terms. Cambridge University Press, Cambridge, pp 58–68.

Zolotov M, Shock E (1999) - Abiotic synthesis of polycyclic aromatic hydrocarbons on Mars. Journal of Geophysical Research: Planets, 104, pp 14033–14049.

Zolotov MY, Shock EL (2000) - A thermodynamic assessment of the potential synthesis of condensed hydrocarbons during cooling and dilution of volcanic gases. Journal of Geophysical Research: Solid Earth, 105, pp 539–559.